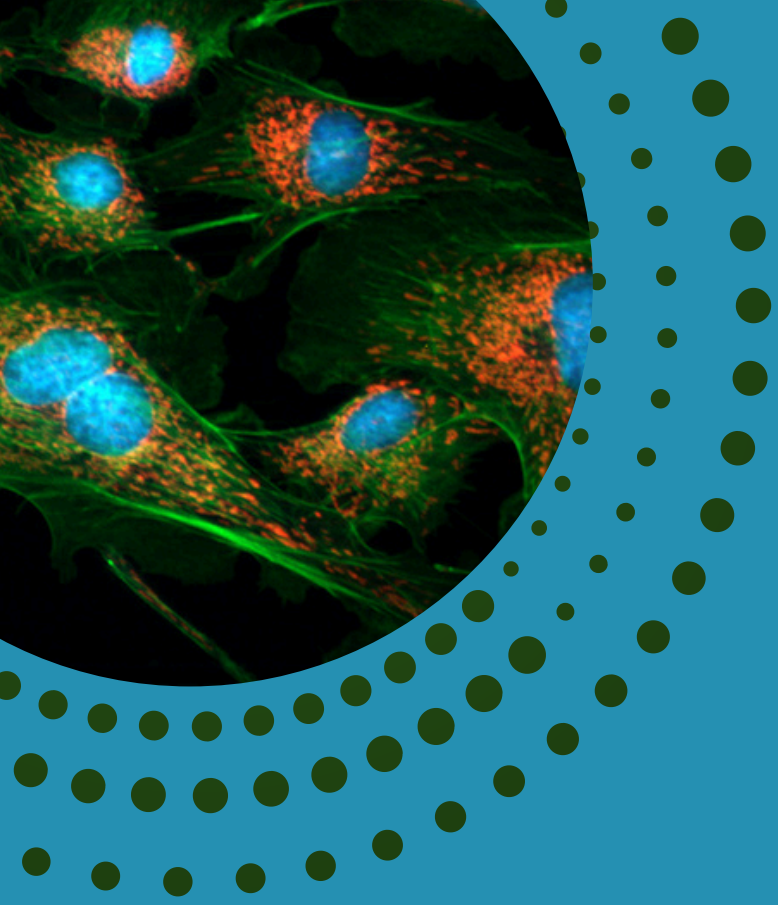

KNJIGA POVZETKOV

BOOK OF ABSTRACTS

6. SLOVENSKO POSVETOVANJE MIKROSKOPISTOV

6TH SLOVENE MICROSCOPY SYMPOSIUM

Slovensko Društvo za Mikroskopijo
SDM
Slovene Society for Microscopy

ROGLA

13.–15. 5. 2026

6. Slovensko posvetovanje mikroskopistov / 6th Slovene Microscopy Symposium
Book of Abstracts

Uredniki: Kristina Žagar Soderžnik, Rok Kostanjšek, Barbara Šetina Batič, Polona Mrak, Nada Žnidaršič, Samo Hudoklin, Blaž Belec, Elena Tchernychova, Melanija Hadolin [editors]

založnik: Slovensko društvo za mikroskopijo
Slovene Society for Microscopy [publisher]

naklada: 100 izvodov [copies]

prva izdaja, prvi natis
Ljubljana, 2026

https://mikroskopsko-drustvo.si/posvet/

CIP - Kataložni zapis o publikaciji
Narodna in univerzitetna knjižnica, Ljubljana

537.533.35(082)
621.385.833.2(082)

SLOVENSKO posvetovanje mikroskopistov (6 ; 2026 ; Rogla)
6. slovensko posvetovanje mikroskopistov = 6th Slovene Microscopy Symposium : book of abstracts / uredniki, editors Kristina Žagar Soderžnik ... [et al.]. - 1. izd., 1. natis. - Ljubljana : Slovensko društvo za mikroskopijo = Slovene Society for Microscopy, 2026

ISBN 978-961-94264-5-6
COBISS.SI-ID 276900355

6. Slovensko posvetovanje mikroskopistov
6th Slovene Microscopy Symposium

Book of Abstracts

Uredniki / editors:
Kristina Žagar Soderžnik, Rok Kostanjšek, Barbara Šetina Batič, Polona Mrak, Nada Žnidaršič, Samo Hudoklin, Blaž Belec, Elena Tchernychova, Melanija Hadolin

Založnik / publisher:
Slovensko društvo za mikroskopijo / Slovene Society for Microscopy

Kazalo / *Table of contents*

Organizatorji se za sponzorstvo zahvaljujejo

The organizers would like to thank our sponzors

Zlati / Gold

Srebrni / Silver

Bronasti / Bronze

Program / *Programme*

Sreda / Wednesday (13. 5. 2026)	
10:30-12:00	**Registracija / Registration with coffee**
12:00-12:15	**Uvodni pozdrav / Welcome address**
	Vodja sekcije / Chair: K. Žagar Soderžnik
12:15-13:00	**Plenarno predavanje / Plenary lecture** S. Šturm, JSI, *From Cosmic Dust to Confined Electrochemistry: Transmission Electron Microscopy of Nucleation, Early Growth and Dissolution*
13:00-14:30	**Kosilo / Lunch break**
	Vodji sekcij / Chairs: P. Mrak, B. Šetina Batič
14:30-15:00	**Vabljeno predavanje / Invited lecture** A. Kladnik, BF UL, *Mikroskopija je okno v biologijo rastlin / Microscopy as a window into plant biology*
	Izbrane predstavitve / Selected talks
15:00-15:15	M. Lachhab, JSI, *Investigating Parameter Dependence in 4D-STEM Measurements of $SrTiO_3$ and $BiFeO_3$*
15:15-15:30	U. Bogataj, BF UL, *3D imaging of arthropod morphology using microCT for educational purposes*
15:30-15:45	A. Jelen, JSI, *Structure and nanostructure of the light rare-earths based CexPrNdSm (x = 0.01–1.5) medium-entropy alloys, leading to an unconventional magnetic state*
15:45-16:00	D. Makovec, JSI, *Structure of Ni-Substituted Barium Ferrite Magnetic Nanoplatelets Synthesized via a Hydrothermal Method: From Stabilization of a β-Alumina-Type Defect Structure to Exchange-Coupled Spinel Ferrite–M-Type Hexaferrite Nanocomposites*
16:00-16:15	G.P. Servetto, Uni Turin, *Abiotic and biotic models: a comparative approach for the study of brain mineralogy*
16:15-16:30	Predstavitev srebrnega sponzorja / Silver sponsor presentation JEOL: L. Vassé, *JEOL News : Portfolio update on all products lines from Table TOP Electron microscope to 300kV TEM*
16:30-18:30	**Sekcija posterjev / Poster session**
19:00-20:30	**Večerja / Dinner**
21:00 -	**Networking**

Četrtek / Thursday (14. 5. 2026)	
8:30-9:00	**Registracija / Registration with coffee**
	Vodji sekcij / Chairs: A. Kladnik , M. Fanetti
9:00-9:30	**Vabljeno predavanje / Invited lecture** V. Sršan, JSI, *Lorentz electron ptychography: A new frontier in magnetic imaging*
	Izbrane predstavitve / Selected talks
9:30-9:45	K. Fink, NIB, *Live Imaging of Spatial Calcium Signatures in Potato Roots and Leaves During Interaction with Endophytic Bacteria*
9:45-10:00	A. Gajović, IRB, *The quaternary W-based refractory alloy for fusion application*
10:00-10:15	G. Dražić, KI, *Combining 4D-STEM with Machine Learning for Ferroelectric Materials Characterization*
10:15-10:30	G. Kapun, KI, *Razbijanje mitov: Razširitev področja uporabe sodobnih večionskih plazemskih sistemov FIB*
10:30-11:15	**Odmor za kavo / Coffee break**
	Vodji sekcij / Chairs: N. Žnidaršič, G. Kapun
11:15-12:00	**Plenarno predavanje / Plenary lecture** D. Zupančič, MF UL, *Decoding Urothelial Biology: Multimodal Microscopy from Cell Biology to Bladder Disease*
	Izbrane predstavitve / Selected talks
12:00-12:15	A. Benčan Golob, JSI, *Nanoscale Elasticity and Plasticity in Ferroelectric Perovskites*
12:15-13:00	Predstavitev zlatega sponzorja / Gold sponsor presentation Thermo Fisher Scientific: R. Spurny, *From Atoms to Cells: Cryo-EM and Cryo-FIB Enabling In Situ Structural Biology* Thermo Fisher Scientific: M. Wu: *The latest development in DualBeam technology for Materials Science*
13:00-14:30	**Kosilo / Lunch break**
	Vodji sekcij / Chairs: R. Kostanjšek, B. Belec
14:30-15:00	**Vabljeno predavanje / Invited lecture** M. Fanetti, UNG, *Collaborations between microscopy lab networks and industry: the experience gained within Interreg projects.*
	Izbrane predstavitve / Selected talks
15:00-15:15	R. Repič, ZAG, *3D Visualisation of Wood: 3D X-ray computed microtomography and 3D printing*
15:15-15:30	I. Dogša, BF UL, *Structural basis of antibiotic tolerance in biofilms*
15:30-15:45	Predstavitev srebrnega sponzorja / Silver sponsor presentation Zeiss: W. Schwinger, *Introducing the new ZEISS Crossbeam 750 with Gemini 4 column and ZEISS EMToolkit SW*
15:45-16:45	**Občni zbor društva**
16:45-18:30	**Sekcija posterjev in kava / Poster session**
19:00-20:30	**Večerja / Dinner**
21:00 -	**Networking and Best Microscopy Image Award announcement**

	Petek / Friday (15. 5. 2026)
8:30-9:00	**Registracija / Registration**
	Vodji sekcij / Chairs: S. Hudoklin, E. Tchernychova
9:00-9:30	**Vabljeno predavanje / Invited lecture** U. Kamenšek, Inst. of Oncology, *Translating gene electrotransfer into clinical oncology: imaging in plasmid development and evaluation*
	Izbrane predstavitve / Selected talks
9:30-9:45	L. Korat Bensa, ZAG, *X-ray Microtomography as a Diagnostic Tool for the Restoration of Slavko Tihec's Kinetic Aquamobile series*
9:45-10:00	T. Zaveršek, MF UL, *Implementation of serial SEM-based volume electron microscopy for use with urothelial tissue samples*
10:00-10:15	D. Feizpour, IMT, *Advanced Transmission Electron Microscopy of Gold Nanoparticles: Methodological Approaches and Nanoscale Structural Analysis*
10:15-10:30	B. Kokot, JSI, *Presentation of the Centre for Advanced Optical Microscopies at J. Stefan Institute (cNOM) and its recent implementation of automated large field-of-view SIM+2.5D+QPI microscopy*
10:30-11:15	**Odmor za kavo / Coffee break**
	Vodji sekcij / Chairs: A. Erman, B. Arah
11:15-11:45	**Vabljeno predavanje / Invited lecture** Č. Donik, IMT, *From Laser Cutting to Microscopy: First Results with Rapid Laser-Based Cross-Section Preparation on the Thermo Scientific Helios 5 Laser*
	Izbrane predstavitve / Selected talks
11:45-12:00	V. Levak, NIB, *Robust quantification of multiplexed fluorescent proteins in plant tissues*
12:00-12:15	S. Ahmad, UNG, *Focused Electron Beam-Induced Heating (FEBH) as a Tool for Local Modification of Materials*
12:15-12:30	T. Sever, IMT, *Tracking hot-deformation behavior of duplex steel with EBSD*
12:30-12:45	Predstavitev srebrnega sponzorja / Silver sponsor presentation SPECION: M. Novak: *Silver Sponsor presentation: SPECION*
12:45-13:00	**Zaključek / Closing remarks**
13:00-14:30	**Kosilo / Lunch break**

Pozdravni nagovor predsednice SDM

Spoštovani udeleženci, cenjeni gostje in razstavljavci,

v veliko čast in zadovoljstvo mi je, da vas lahko v imenu Slovenskega društva za mikroskopijo in Organizacijskega odbora pozdravim na »6. slovenskem posvetovanju mikroskopistov«.

Po uspešno izvedenih petih posvetovanjih slovenskih mikroskopistov, je dogodek postal tradicionalen. Tokrat se srečujemo drugič na Rogli in veseli me, da število udeležencev in interes razstavljavcev za tokratni posvet ponovno potrjuje veliko zanimanje za mikroskopijo in tovrstna srečanja v regiji. V znanstvenem programu posveta smo zato poskušali zajeti čim širši nabor mikroskopskih tehnik in aktualnih področij njihove uporabe v slovenskem prostoru, t.j. na področju naravoslovnih znanosti, znanosti o materialih ter znotraj industrijskega sektorja.

Plenarni predavanji dr. Daše Zupančič in dr. Saša Šturma, tako dopolnjuje pet vabljenih predavanj ter devetnajst krajših predavanj z različnih področij mikroskopije in analize slike. Znanstveni program zaokroža 40 predstavitev v okviru posterske sekcije.

Poleg predstavitve najnovejših dosežkov s področja mikroskopije, namen posveta ostaja tudi aktualni pregled mikroskopske opreme, laboratorijev in metodologij priprave, opazovanja in analize vzorcev na območju Slovenije. Temu je namenjen spremljevalni program srečanja, v okviru katerega želimo vzpostaviti primerno okolje za različne neformalne oblike izmenjave izkušenj in vzpostavljanje novih povezav med uporabniki in ponudniki mikroskopske opreme.

V zaključku nagovora se zahvaljujem Znanstvenemu odboru posveta za vsebinsko pripravo programa in razširjenemu Organizacijskemu odboru za samo izvedbo posveta. Prav tako se zahvaljujem predavateljem za njihove prispevke in moderatorjem za vodenje znanstvenih sekcij. Zahvaljujem se tudi gostom, da so se odzvali povabilu. Posebna zahvala pa gre vsekakor tudi domačim in tujim zastopnikom in proizvajalcem mikroskopske opreme, ki so s finančno podporo srečanja in predstavitvami aktualnih mikroskopskih tehnik omogočili organizacijo srečanja v pričujočem obsegu in obliki.

Dr. Kristina Žagar Soderžnik
Predsednica Slovenskega društva za mikroskopijo

Plenarni predavanji / *Plenary lectures*

Sašo Šturm: *From Cosmic Dust to Confined Electrochemistry: Transmission Electron Microscopy of Nucleation, Early Growth and Dissolution*

Daša Zupančič: *Decoding Urothelial Biology: Multimodal Microscopy from Cell Biology to Bladder Disease*

From Cosmic Dust to Confined Electrochemistry: Transmission Electron Microscopy of Nucleation, Early Growth and Dissolution

Sašo Šturm [a,b], Layrton José Souza da Silva[a], Monica Parpal [c,d]; Mohamed El Marini [c,d]; Daniel Torres[c], Anže Prašnikar [e]; Blaž Likozar [e], Jon Ustarroz [c,d]; Mirijam Vrabec [b], Bojan Ambrožič [f], Sorour Semsari Parapari [a]

[a]*Jožef Stefan Institute (Ljubljana), Slovenia*

[b]*University of Ljubljana (Ljubljana), Slovenia*

[c]*Université libre de Bruxelles (ULB) (Brussels), Belgium*

[d]*Vrije Universiteit (Brussel), Belgium*

[e]*National Institute of Chemistry (Ljubljana), Slovenia*

[f]*Nanocenter (Ljubljana), Slovenia*

Contact email: saso.sturm@ijs.si

Nucleation and the earliest growth stages of matter govern processes across enormous length scales, from the condensation of cosmic dust in stellar outflows, which ultimately contributes to the formation of planetary building blocks, to the controlled synthesis, processing, and degradation of functional nanomaterials.

This presentation will highlight how Transmission Electron Microscopy (TEM) can be used as an experimental tool to access these transient stages of matter formation, combining structural and spectroscopic analysis with in situ and operando observations in dynamic environments. First, microgravity experiments designed to mimic the nucleation and early growth of dust analogues under astrophysically relevant conditions will be discussed, showing how suppressed convection, density fluctuations, and collision frequencies influence nucleation pathways and particle size distributions [1].

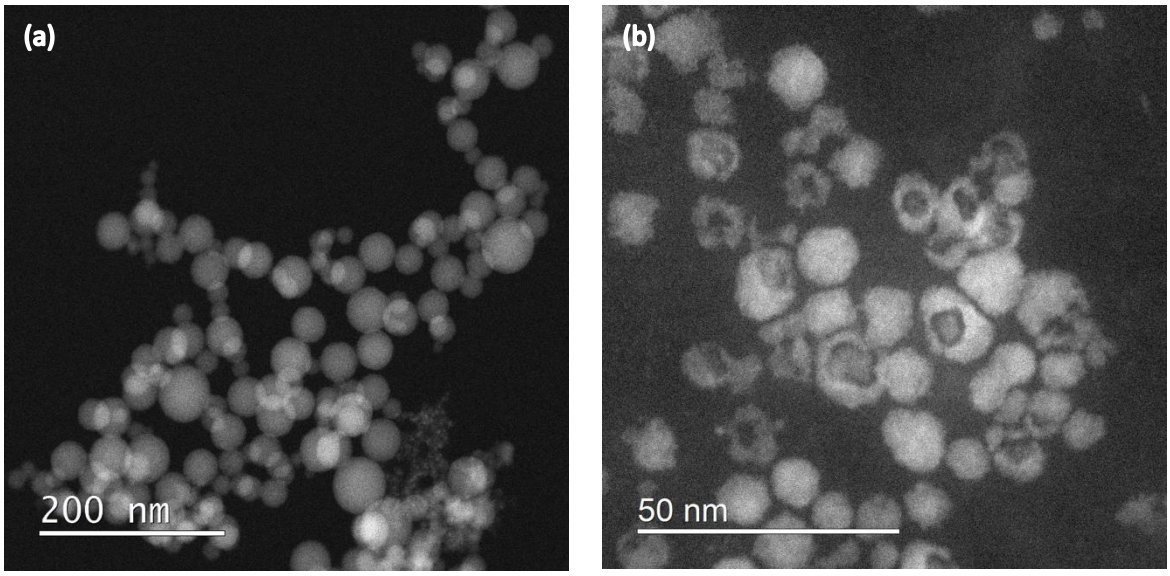

Figure 1 (a) Simulated alumina cosmic dust under microgravity conditions and (b) core-shell formation of Ag nanoparticles during the electrochemical dissolution process.

The talk will then turn to liquid-cell electrochemical TEM, where confined reaction volumes enable direct visualisation of nanoparticle nucleation, growth, ripening, passivation, and dissolution under applied electrical bias [2]. Particular emphasis will be placed on confinement as both a challenge and an opportunity: nanoconfinement alters mass transport, local concentration fields, double-layer overlap, and reaction kinetics, thereby altering the effective reaction environment and leading to conditions that can differ significantly from macroscopic electrochemical conditions. The role of beam-driven radiolysis and radical chemistry will also be emphasised, not only as a source of experimental complexity, but as an active contributor to local redox pathways in liquid-cell TEM [3].

Overall, the presentation will show that direct TEM observation provides a unique bridge between fundamental questions of matter formation, from space dust to advanced nanomaterials, and the fine design of nanoscale processing routes.

Acknowledgements: Authors affiliated with JSI acknowledge the ARIS for financial support under P2-0084, PR-13066-5, J2-60043, GC-0004-3, N1-0401-2, PR-12334 and Z2-50057.

References:

1. Kimura, Y., Ishizuka, S., Šturm, S., Tanaka, K. K., Yamazaki, T., SATOH, Y., ... & INATOMI, Y. (**2018**). Nucleation processes of cosmic dust investigated by microgravity experiments using an airplane. *International Journal of Microgravity Science and Application*, *35*(3), 350305.
2. El Marini, M., Leontev, A., Prasnikar, A., Parpal, M., da Silva, L. J. S., Parapari, S. S., S. Šturm, ... & Ustarroz, J. (**2026**). Electrochemical TEM: Simulating Electrochemistry Coupled with Radiolysis. *ACS Electrochemistry*.
3. Ambrožič, B., Prašnikar, A., Hodnik, N., Kostevšek, N., Likozar, B., Rožman, K. Ž., & Šturm, S. (**2019**). Controlling the radical-induced redox chemistry inside a liquid-cell TEM. *Chemical science*, *10*(38), 8735-8743.

Decoding Urothelial Biology: Multimodal Microscopy from Cell Biology to Bladder Disease

Daša Zupančič[1], Rok Romih[1], Mateja Erdani Kreft[1], Samo Hudoklin[1], Nataša Resnik[1], Andreja Erman[1], Aleksandar Janev[1], Larisa Tratnjek[1], Tadeja Kuret[1], Brina Dragar[1], Jera Jeruc[2], Karmen Wechstersbach[2], Jelena Korać Prlić[2] and Peter Veranič[1]

[1]*Insitute of Cell Biology, Faculty of Medicine, University of Ljubljana, Slovenia*

[2]*Insitute of Pathology, Faculty of Medicine, University of Ljubljana, Slovenia*

[3]*Department of Immunology and Medical Genetics, School of Medicine, University of Split, Croatia*

Presenting and corresponding author: Daša Zupančič, email: dasa.zupancic@mf.uni-lj.si

Abstract:

The urothelium is a highly specialized epithelium that remains remarkably stable under physiological conditions, yet undergoes rapid regeneration and differentiation following injury and is susceptible to a range of diseases. Decoding its structural and functional organization requires integrative histochemical and microscopy approaches that bridge ultrastructure, molecular composition and cellular function. This lecture will present multimodal microscopy strategies that combine electron microscopy (TEM and SEM), lectin histochemistry, combined lectin- and immuno-histochemistry (CLIH), immunohistochemistry, immunofluorescence and proximity ligation assay (PLA) to investigate urothelial biology across spatial scales. These complementary techniques enable detailed analysis of membrane specialization, differentiation processes, lectin binding and endocytic pathways, as well as retinoic acid signalling in urothelial carcinogenesis and cystitis. Selected examples will demonstrate how the integration of structural and molecular imaging provides new insights into urothelial regeneration, cystitis, and bladder cancer. Particular emphasis will be placed on the effects of vitamin A and retinoids in these pathological processes. By linking advanced imaging methodologies with key biological mechanisms, this lecture highlights how multimodal microscopy contributes to a deeper understanding of urothelial function in health and disease, and supports the development of innovative diagnostic and therapeutic strategies.

Keywords: urinary bladder, bladder cancer, cystitis, microscopy, histochemistry, lectins, vitamin A, retinoids

Vabljena predavanja / *Invited lectures*

Aleš Kladnik: *Mikroskopija je okno v biologijo rastlin / Microscopy as a window into plant biology*

Vinko Sršan: *Lorentz electron ptychography: A new frontier in magnetic imaging*

Mattia Fanetti: *Collaborations between microscopy lab networks and industry: the experience gained within Interreg projects*

Urška Kamenšek: *Translating gene electrotransfer into clinical oncology: imaging in plasmid development and evaluation*

Črtomir Donik: *From Laser Cutting to Microscopy: First Results with Rapid Laser-Based Cross-Section Preparation on the Thermo Scientific Helios 5 Laser*

Microscopy as a window into plant biology

Aleš Kladnik[a]

[a]*University of Ljubljana, Biotechnical Faculty, Slovenia*

Contact email: ales.kladnik@bf.uni-lj.si

Plants are beautiful, and when you look at them up close with a microscope, they are truly fascinating. Fresh plant tissue sections usually have sufficient contrast to be observed with bright field microscopy, so additional staining is not necessary. However, for detection of specific compounds, a wide range of histology staining protocols is available. Plant samples can just be observed with a microscope, or we can photograph them using a camera. When documenting microscopic images, it is important to consider the purpose of the image. Images can be used as research data or educational material. Therefore, images should include at least a scaling bar indicating the size of structures shown in the image. We have developed a Fiji plugin to apply an appropriately sized scaling bar onto a spatially calibrated image (https://github.com/aleskl/imagej). Samples are sometimes too large to fit in a single field of view of the camera. In this case, we can stitch a grid of overlapping images into a large panorama overview. When stitching images, we need to ensure that we use the correction of shading, an artifact in light microscopy when image brightness is reduced towards the image edges. Plant samples can also be observed with an epi-fluorescence microscope. Plant cells, especially cell walls, exhibit strong autofluorescence without the addition of external fluorochromes. We have used changes in autofluorescence spectra in alkaline pH to characterise secondary metabolites in cell walls in the transport region of the maize kernel. Autofluorescence can also be used to reconstruct the surface of samples in 3D using structured illumination microscopy (SIM). However, autofluorescence can pose a challenge in detecting signals from fluorochrome-labelled probes, so the type of fluorochrome label should be carefully selected to avoid overlap with the intrinsic fluorescence of the sample. Molecular localisation methods used in our research include immunolocalisation and in situ hybridisation. To avoid signal confusion in fluorescence we prefer to use enzymatic reactions to detect the sites of antibody or nucleic acid probe binding, mainly using alkaline peroxidase-labelled secondary antibodies and NBT/BCIP substrate. The imaging examples above document what can be seen with a microscope, but images can also be used to extract quantitative data from our samples. Objects in an image can be measured manually using measurement tools in image analysis software, or detected and measured automatically using machine vision methods. We used YOLO object detection to automatically measure the dimensions of stomata in leaves of buckwheat genotypes with different ploidy levels. However, automatic object detection methods should be validated by manual measurements in a subset of samples to confirm the accuracy of automatic measurements. An important method in our laboratory is measurement of genome size using image densitometry. The relative amount of nuclear DNA is measured as the optical density of Feulgen-stained nuclei. With this method, we can compare genome size in species differing in ploidy level. We can also measure absolute genome size if we measure optical density in a standard species with known genome size. The most exciting research topic regarding genome size is measurement of somatic endopolyploidy. During differentiation, plant cells often switch to an endoreplication cell cycle, where DNA doubles but the cells and nuclei do not divide, resulting in highly polyploid cells. Cells with multiple genome copies can grow larger, which is beneficial, for example, in storage tissues. We have measured genome size and cell size in seed storage tissue endosperm of maize and related species. Cell size was positively correlated with genome size, but interestingly, in direct correlation with cell surface area, not volume. Together, these examples illustrate how a combination of classical and advanced microscopy techniques, complemented by quantitative image analysis, can provide insights into plant biology, combining structure and molecular biology.

Lorentz electron ptychography: A new frontier in magnetic imaging

Vinko Sršan[a,b], Sergej Ražnjević[a], Matej Komelj[a], Sašo Šturm[a,b,c]

[a] *Jožef Stefan Institute, Department for Nanostructured Materials, Jamova cesta 39, Ljubljana Sl-1000, Slovenia*

[b] *Jožef Stefan International Postgraduate School, Jamova cesta 39, Ljubljana Sl-1000, Slovenia*

[c] *University of Ljubljana, Faculty of Natural Sciences and Engineering, Department of Geology, Ljubljana, Slovenia*

Contact email: vinko.srsan@ijs.si

Quantitative magnetic imaging at the nanoscale is essential for understanding and optimization of functional magnetic materials, from high-performance permanent magnets to emerging spin-textured systems. However, direct imaging of magnetic induction at both high spatial resolution and quantitative accuracy remains challenging.

In this talk, I will review the capabilities of conventional approaches to magnetic imaging methods, starting with Fresnel-mode transmission electron microscopy (Fresnel-TEM) and extending to differential phase contrast scanning transmission electron microscopy (DPC-STEM) case studies of NdFeB-based permanent magnets and skyrmionic systems. I will illustrate how these approaches provide valuable insights into functional material properties and foundational understanding of magnetism while simultaneously highlighting known limitations in terms of spatial resolution, interpretability, and quantitative reliability.

These limitations motivate the development of methods that provide access to higher-resolution imaging. To resolve this limitation, I will introduce Lorentz electron ptychography (LEP), a phase retrieval approach based on simultaneous reconstruction of the specimen phase as well as the electron probe, based on redundant information obtained by oversampled scanning of the specimen. This information redundancy is used for correction of the scanning artifacts as well as determination of the electron-probe aberrations, which consequently improves the spatial resolution. I will demonstrate the improvement of LEP imaging capabilities over conventional approaches on examples of singular magnetic texture features like magnetic domain walls and skyrmion edges.

Finally, I will discuss the practical aspects of LEP, focusing on implementability in routine electron microscopy workflow.

Keywords: Lorentz electron ptychography, Magnetic imaging, Nanomagnetism

This work is supported by the Slovenian Research Agency (ARIS) under grant number P2-0084 and the European Union's Horizon Europe research and innovation program GREENE (grant agreement no. 101129888).

Collaborations between microscopy lab networks and industry: the experience gained within Interreg projects.

Mattia Fanetti[a]

[a] *Materials Research Laboratory, University of Nova Gorica, Vipavska 13c, Ajdovščina 5270, Slovenia*

Contact email: mattia.fanetti@ung.si

Introduction:
One of the challenges for innovation in the regional industry compartment is the application of high-tech technologies in the research and development process. However, especially for SME, it is often impossible to access such technologies (for example, electron microscopy) due to the high cost of equipment and need for specialized expertise. At the same time, several state-of-the-art laboratories are present, in the same region, within academic institutions and research centers. In the field of microscopy alone, there is a huge concentration of high-end microscopes in Ljubljana (JSI, Nanocenter, National Intitute of Chemistry, and others…), but also at University of Nova Gorica, as well as in the Trieste area (CNR-IOM, Area Science Park, University of Trieste, …). A natural way to tackle the challenge is then to find an effective approach to match the needs of companies for specialized technologies and the available research laboratories already present in the regional territory.
In the last years, this approach has been at the base of some Interreg projects, whose objective was to create a collaborative network of laboratories, and to connect them to the regional industrial fabric, in order to raise the awareness about the capability of high-tech approach to solve their production problems by showing it with demonstrative experiments.
In this contribution, realized within ALL-MICRO project [1], this approach is described, with some general description of the created laboratory networks and some case studies of effective collaborations with the industrial world.

Methods: three Interreg projects are considered: RETINA (SLO-AUT Interreg projects, 2017-2020)[2], Nano-Region (ITA-SLO strategic interreg project, 2019-2022)[3] and ALL-MICRO (ITA-SLO standard project, 2024-2026)[1]. In all of them, one core activity was the realization of demonstrative experiments proposed by companies and realized in the regional research institutes, with the aim to show to the enterprises how the high-tech capability and expertise owned in the research labs can be used to address industrial problems.

Results: Overall, in the three considered projects more than 40 experiments proposed by the companies have been realized, together with other actions (summer schools, public events, …) to raise awareness about the capabilities of research laboratories in the region. The collaboration between companies and research labs is not always straightforward, due to the distance between the industrial and the research approaches in solving technological problems. Still, the experience has been positive in the vast majority of cases. In some cases, the collaboration with companies continued beyond the project activities. In all cases, awareness of the potential of high-tech technologies for R&D has increased.

Moreover, a tight collaboration between the regional research laboratories and with technology transfer facilitator (e.g. technology parks) have been established, beneficial not only for mutual technological and expertise support, but also to coordinate for a more effective interface with the potential external users (for example, making common web platforms for external users engagement, e.g. [1,3]).

Discussion and conclusions:
Two main outcomes are evident:
1) the connection and collaboration between research laboratories in the region are beneficial, for increased expertise, technical support and coordinated actions when interfacing with external users.

2) the collaboration between companies and research laboratories, within the scheme of demonstrative experiments as implemented in the Interreg projects, is beneficial in demonstrating to the companies the potential of high-end technologies (included microscopy) for industrial technological innovation.

In perspective, the public funding of demonstrative trial experiments proposed by companies and implemented in the research centers looks a promising scheme for triggering the collaboration between industry and research, and a more permanent funding scheme for these actions is advisable in the regional context.

Acknowledgements: ALL-MICRO is financed by the Interreg VI-A Italy-Slovenia Programme.

References:

1. https://www.ita-slo.eu/en/all-micro , https://all-micro.eu/
2. https://keep.eu/projects/18090/Odpiranje-raziskovalnih-lab-EN/
3. https://2014-2020.ita-slo.eu/nano-region , https://www.nanoregion.eu/

Translating gene electrotransfer into clinical oncology: imaging in plasmid development and evaluation

Urška Kamenšek[a, b], Maja Čemažar[a, c]

[a]*Department of Experimental Oncology, Institute of Oncology Ljubljana, Ljubljana, Slovenia*
[b]*Biotechnical Faculty, University of Ljubljana, Ljubljana, Slovenia*
[c]*Faculty of Health Sciences, University of Primorska, Izola, Slovenia*
Contact email: ukamensek@onko-i.si

Gene electrotransfer (GET) using plasmid DNA (pDNA) represents a promising non-viral approach in cancer gene therapy. At the Department of Experimental Oncology, we have spent over two decades advancing electroporation-based approaches from fundamental research to clinical application. Within the SmartGene.Si project, we established an integrated translational platform spanning rational plasmid design, clinical-grade production, and validation in preclinical models and veterinary clinical studies, ultimately enabling the first-in-human Phase I clinical trial of GET-based gene therapy in Europe using our antibiotic-free interleukin 12 plasmid [1].

Plasmid vectors are circular DNA molecules engineered as non-viral vectors for the delivery of therapeutic genes. Compared to viral vectors, they offer advantages such as improved safety, low immunogenicity, high cargo capacity, and flexible design. However, as they do not efficiently enter eukaryotic cells on their own, their delivery relies on methods such as electroporation. Gene electrotransfer (GET) transiently increases membrane permeability using specific electric pulses (reversible electroporation), enabling efficient intracellular delivery and supporting both local and systemic anticancer approaches.

Imaging technologies play an important role throughout the translational development of plasmid-based gene therapies, from quality control to mechanistic insight and therapeutic evaluation. During plasmid preparation, electrophoresis and chromatography are routinely used to assess identity, purity, and topology, with the supercoiled form being critical for transfection efficiency and clinical use [2]. Advanced imaging methods such as electron microscopy and atomic force microscopy further enable direct visualization of plasmid structure. Following delivery to cells, fluorescence-based high-resolution imaging approaches allow tracking of plasmid uptake, intracellular trafficking, and nuclear localization [3]. Using reporter systems such as green fluorescent protein (GFP), imaging also supports the assessment of transfection efficiency [4]. At the tissue level, non-invasive and intravital reporter gene imaging enable spatiotemporal evaluation of gene expression within tumors and other tissues. Finally, imaging is indispensable for assessing plasmid functionality and therapeutic potential. Reporter systems enable evaluation of promoter activity [5], as well as protein localization and secretion. Moreover, functional imaging enables monitoring of therapeutic responses, including tumor regression, immune cell infiltration, and anti-angiogenic effects [6].

In conclusion, GET of pDNA represents a safe, versatile, and effective approach for cancer treatment, with growing clinical relevance. Imaging and microscopy are integral tools that complement molecular and functional assays in the development of plasmid-based gene therapies, supporting their successful clinical implementation.

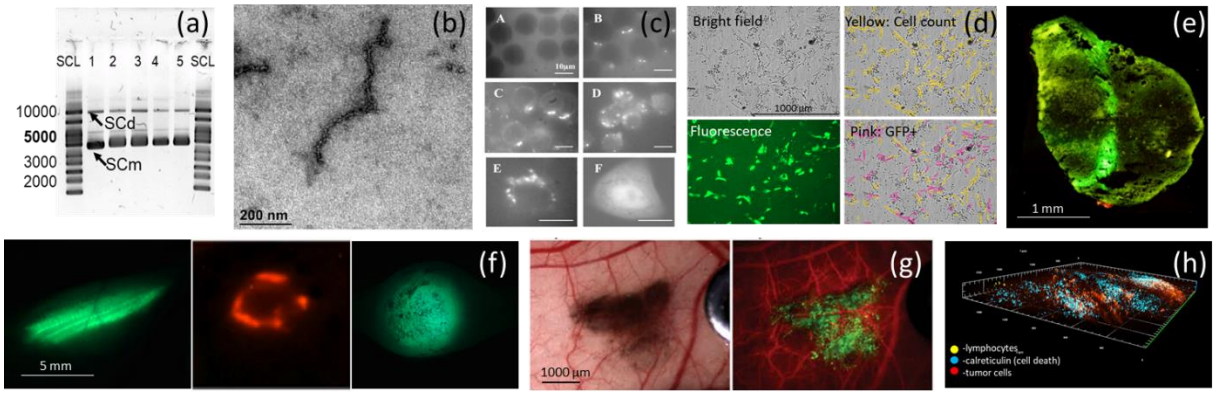

Figure 1: **Imaging plasmid DNA across the gene electrotransfer translational pipeline,** from plasmid quality control to intracellular delivery and in vitro and in vivo therapeutic evaluation. (a) Agarose gel electrophoresis of uncut plasmid DNA (pDNA) demonstrating supercoiled monomer and dimer topoisomer conformations; (b) transmission electron microscopy (TEM) image confirming the supercoiled structure of pDNA (courtesy of Dr. Magda Tušek Žnidarič, National Institute of Biology); (c) visualization of cellular uptake and intracellular trafficking of fluorescently labeled pDNA (Golzio *et al.*, *Proc. Natl. Acad. Sci. U.S.A.* 2002); (d) quantitative assessment of transfection efficiency following gene electrotransfer (GET) of a GFP reporter gene using Gen5 data analysis software (Cytation 1 multimode reader); (e) spatial mapping of GFP expression in frozen tissue sections (Olympus BX51 fluorescence microscope); (f) non-invasive imaging of reporter gene expression in transiently transfected muscle (left), skin (middle), and stably transfected tumors (right) (Zeiss SteREO Lumar.V12 stereomicroscope); (g) dorsal window chamber model showing a fluorescent tumor and rhodamine B dextran-labeled vasculature (Zeiss SteREO Lumar.V12 stereomicroscope); (h) intravital imaging of tumor cell death and immune cell infiltration within the window chamber model (Zeiss LSM 800 confocal laser scanning microscope).

References:

1. P. Strojan et al. *J. Surg. Oncol.* **2025**, 51
2. U. Kamenšek, A. Renčelj, T. Jesenko, T. Remic, G. Serša, M. Čemažar, *Heliyon* **2022**, 8.
3. M. Golzio, J. Teissie, M. P. Rols, *Proc. Natl. Acad. Sci. U.S.A.* **2002**, 99, 1292–1297.
4. U. Kamenšek, T. Božič, M. Čemažar, U. Švajger, *Pharmaceutics* **2025**, 17.
5. U. Kamenšek, G. Serša, M. Čemažar, *Mol. Cancer* **2013**, 12.
6. M. Savarin at al. *Technol. Cancer Res. Treat.* **2018**, 17.

Keyword: plasmid DNA, gene electrotransfer, cancer gene therapy, imaging techniques

From Laser Cutting to Microscopy: First Results with Rapid Laser-Based Cross-Section Preparation on the Thermo Scientific Helios 5 Laser

Črtomir Donik, Irena Paulin, Barbara Šetina Batič, Elena Tchernychova, Matjaž Godec

Institute of metals and technology, Ljubljana

A Thermo Scientific Helios 5 Laser system has recently been installed at the Institute of Metals and Technology (IMT) in consortium with KI, IJS, and ZAG. In this contribution, we present our first experiences and initial results in laser cutting and cross-section preparation of selected metallic materials and multilayer systems. Particular emphasis is placed on rapid access to subsurface regions of interest without the conventional metallographic preparation steps of cutting, sectioning, mounting, grinding, and polishing. The laser-based approach enables site-specific opening of selected areas and preparation of relatively large cross-sections within minutes, significantly reducing sample preparation time. The resulting surfaces are suitable for immediate investigation in the scanning electron microscope (SEM), including high-resolution imaging and energy-dispersive X-ray spectroscopy (EDS) analysis. Initial results demonstrate that meaningful elemental distributions can be obtained directly from laser-prepared cross-sections, allowing fast qualitative and semi-quantitative assessment of compositional variations and interfaces. For applications requiring higher surface quality and reduced damage layers, laser preparation can be effectively combined with subsequent Ga FIB polishing. This hybrid workflow enables the removal of the laser-affected layer and preparation of high-quality cross-sections suitable for detailed microstructural and analytical investigations, including high-resolution SEM imaging and more precise EDS mapping. An initial assessment of the advantages and limitations of laser-based preparation compared with conventional metallographic techniques will also be discussed.
This approach is particularly advantageous for biodegradable Fe–Mn–C-based alloys (ARIS Rebone project J7-70256), enabling rapid investigation of microstructural heterogeneity and degradation-related interfaces, as well as bone and other tissue attachment, which are critical for biomedical performance.

The newly installed instrument opens new possibilities for rapid failure analysis, efficient investigation of coatings and interfaces, and advanced characterization of complex metallic and multiphase materials, combining high throughput with site-specific precision.

The authors acknowledge the financial support from the Slovenian Research Agency ARIS (research project No. J7-70256, and research core funding P2-0132).

ELECTRON MICROSCOPY

Thermo Scientific™ Helios™ 5 Laser PFIB

Fastest high-quality subsurface and 3D characterization at millimeter scale with nanometer resolution.

ThermoFisher SCIENTIFIC

Phenom XL G3 Desktop SEM

Discover the new **Thermo Scientific™ Phenom™ XL G3 Desktop SEM,** the longer-lasting CeB6 electron source reduces downtime and costs, while the improved backscatter electron detector delivers higher contrast, better compositional analysis, and superior signal-to-noise ratio—ideal for both industry and academia.

LONGER LIFE, SHARPER INSIGHTS

High performance and efficiency in a compact design.

NEW

OPTIKA® ITALY

Professional Stereo Microscopes

SLX SERIES - Stereomicroscopes For Higher Education & Laboratory
SZ SERIES - Stereozoom Microscopes For Laboratory & Industry
CL SERIES - Cold Light Illuminators
GEM SERIES - Stereozoom Microscopes For Gemology

Industrial Microscopes

MET SERIES - Metallurgical Microscopes
IS SERIES - Inspection Video Microscopes

WWW.ITR-LAB.SI

ALL YOU NEED FOR ELECTRON MICROSCOPY

ULTIMATE EQUIPMENT SOLUTIONS • CUSTOM SERVICE • HIGH QUALITY FOR OUR CUSTOMERS
PERSONAL PROFESSIONAL APPROACH • COMMITMENT TO YOUR SUCCESS

ITRLAB

Izbrane predstavitve / *Selected talks*

Maryem Lachhab

Urban Bogataj

Andreja Jelen

Darko Makovec

Qiulia Pia Servetto

Katja Fink

Andreja Gajović

Goran Dražić

Gregor Kapun

Andreja Benčan Golob

Rožle Repič

Iztok Dogša

Lidija Korat Bensa

Tim Zaveršek

Darja Feizpour

Boštjan Kokot

Valentina Levak

Shazeb Ahmad

Tina Sever

Investigating Parameter Dependence in 4D-STEM Measurements of $SrTiO_3$ and $BiFeO_3$

Meryem Lachhab [a,b], Victor Regis[a,b], Vinko Sršan [a,b], Tara Gudžulić [c], Katarina Žiberna[a,b], Charles Paillard [d], Andreja Benčan [a,b], Goran Dražić [e], Mojca Otoničar [a,b]

[a] *Jožef Stefan Institute, Jamova cesta 39, SI-1000 Ljubljana, Slovenia*

[b] *Jožef Stefan International Postgraduate School, Jamova cesta 39, SI-1000 Ljubljana, Slovenia*

[c] *Center for Electron Microscopy and Microanalysis, Jožef Stefan Institute, Jamova cesta 39, 1000 Ljubljana, Slovenia*

[d] *Smart Ferroic Materials Center, Physics Department and Institute for Nanoscience and Engineering, University of Arkansas, Fayetteville, Arkansas 72701, USA*

[e] *National Institute of Chemistry, Ljubljana 1000, Slovenia*

Contact email: meryem.lachhab@ijs.si

Understanding local electric fields and lattice distortions at the nanoscale is essential for studying functional oxide materials. In particular, polar ferroelectric perovskites, such as $BiFeO_3$ (BFO), exhibit structural and electronic properties that can be strongly influenced by processing conditions and induced defects [1]. To understand the effect of defects on the functional properties, we first aimed to investigate defect-free perovskite structures by four-dimensional scanning transmission electron microscopy (4D-STEM) [2], to primarily evaluate the influence of experimental parameters in determining local structural and electric-field variations in pristine lattices of the reference cubic $SrTiO_3$ and rhombohedral BFO lattice.

4D-STEM experiments were performed using a pixelated detector by recording convergent beam electron diffraction (CBED) patterns at each probe position during scanning at different convergence angles (CA) (15, 21, 30 mrad) and camera lengths (CL) (145, 285, 460 mm). These changing parameters allowed a trade-off between getting more information from larger recorded diffractions and eliminating distortions coming from lens aberrations or defocus effects due to sample thickness. The diffraction datasets were analysed using py4DSTEM package to extract beam deflections and quantify variations in the centre-of-mass (CoM) shift [3]. Simulations on relaxed BFO structure (by Density Functional Theory) and STO were performed using abTEM python package to support interpretation of the experimental results [4].

The results show that the CA and the CL significantly influence the measured CoM shifts and the intensity distribution within the diffraction disks. In STO (figure1-a), the diffraction patterns remain largely centrosymmetric, providing a stable reference for evaluating parameter dependence. In contrast, BFO (figure1-b) exhibits directionally biased intensity distributions consistent with its polar structure. Both experimental and simulated data show similar trends, confirming the sensitivity of 4D-STEM to local structural and electrostatic variations.

These findings demonstrate that careful optimisation of experimental parameters is crucial for reliable 4D-STEM analysis. The comparison between STO and BFO highlights the potential of this technique for studying polar materials and defect-related phenomena. Future work will focus on applying the optimised methodology to investigate defected structures in BFO such as dislocations, their associated local electric fields and charge density distributions and their influence on the macroscopic properties.

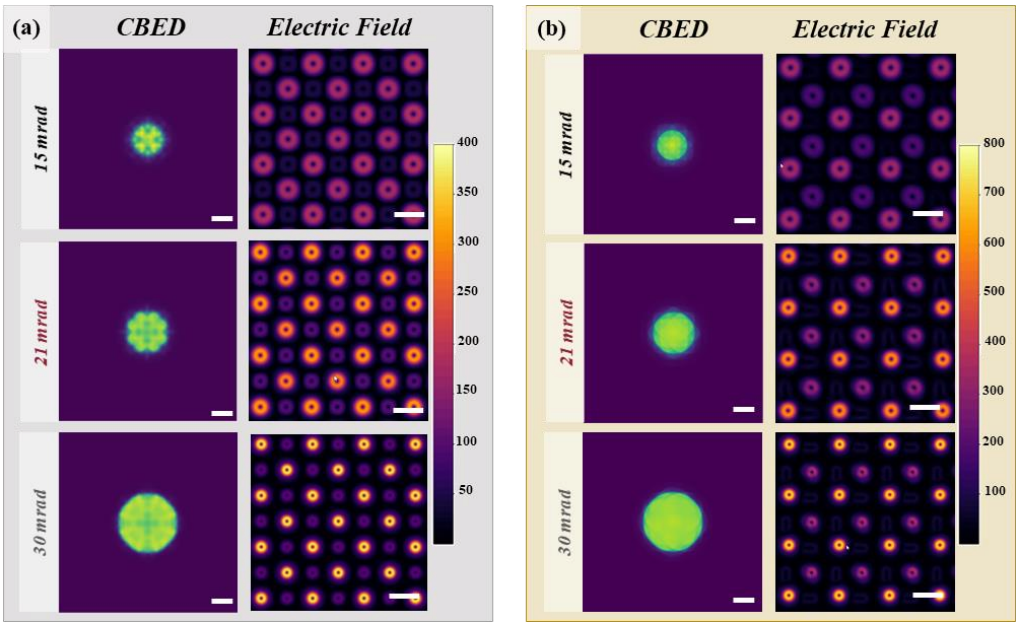

Figure 1: Simulated 4D-STEM results for STO (a) and BFO (b) at convergence semi-angles of 15, 21, and 30 mrad, showing the averaged CBED patterns and reconstructed in-plane electric field maps (V/m). Scale bars: 10 mrad (diffraction) and 200 pm (real space).

References:

1. S. Salmanov *et al.*, Jan. 2025, vol. 45, no. 1, p. 116846.
2. C. Ophus, *Microscopy and Microanalysis*, Jun. 2019, vol. 25, no. 3, pp. 563–582.
3. B. H. Savitzky *et al.*, *Microscopy and Microanalysis*, Aug. 2021, vol. 27, no. 4, pp. 712–743.
4. J. Madsen and T. Susi, Open Research Europe 1:24, 2021.

3D imaging of arthropod morphology using microCT for educational purposes

Urban Bogataj[a], Gregor Bračko[a], Teo Delić[a], Žiga Fišer[a], Rudi Verovnik[a], Miloš Vittori[a], Valerija Zakšek[a], Cene Fišer[a], Rok Kostanjšek[a]

[a]*University of Ljubljana, Biotechnical faculty, Department of biology, (Ljubljana), Slovenia*

Contact email: urban.bogataj@bf.uni-lj.si

Introduction: Arthropods represent the vast majority of all currently known animal species. They thrive in all ecosystems on Earth and exhibit great diversity of functional morphologies. Our project 3D Atlas of Arthropods aims to promote the morphological diversity of arthropods to students of natural sciences, biology teachers, high school students, and nature enthusiasts, and to advance the digitalization in education at the University of Ljubljana. We performed visualization of selected arthropod species from all four major arthropod subphyla to present morphological differences between taxa and to elucidate the associations between the form and function.

Methods: X-ray microtomography was employed to perform the 3D imaging of arthropod specimens, which were acquired from our collection, either fixed in ethanol or dry, and from additional collections in the field, preserved in ethanol. The specimens were contrasted with 1% I_2 solution in 100% ethanol and scanned with a Neoscan N80 (Neoscan) microtomograph. To image the 3D anatomy of the digestive system inside the Colorado potato beetle (*Leptinotarsa decemlineata*), the specimens were fixed in 2.5% glutaraldehyde and 4% formaldehyde in HEPES buffer, dehydrated in graded series of ethanol, contrasted with 1% I_2 solution in ethanol, transferred to HMDS (hexamethyldisilazane), and dried by evaporation of HMDS. For each specimen, a sequence of two-dimensional X-ray projection images were recorded at rotation steps of 0.2° over the span of 360°. This series of images was then used to reconstruct the animal's 3D structure with filtered backprojection, which is the reconstruction algorithm used by the Neoscan N80 system. The obtained 3D reconstruction is a stack of detailed cross-section images in successive planes along the body of the scanned specimen (Fig. 1A). A series of such cross-section images can be rendered as a 3D model of the scanned arthropod. The obtained 3D stack of images was then processed using Dragonfly software (Comet Technologies). In the 3D dataset the body of the specimen was first segmented from the background (Fig. 1B). This subset of voxels representing the entire body of the animal was then segmented into the main body regions (Fig. 1C). For each body region a 3D mesh of its surface was prepared (Fig. 1D). In the open-source Blender software, these meshes were then stitched into a 3D model of a whole animal with body regions displayed in different colours. In 3D datasets of Colorado potato beetles the digestive system was segmented (Fig. 2A).

Results and discussion: 3D models with labelled body regions of specimens belonging to 50 arthropod species from all four arthropod subphyla (Chelicerata, Myriapoda, Crustacea and Hexapoda) were prepared and uploaded to the project's website (http://3datlas.si). Each 3D model is supplied with the description of external anatomy and biology of species, as well as with detailed photographs. At the website, the models are displayed in an interactive 3D viewer, which allows their rotation in all three spatial axes, zooming, and thus observation of the external morphology from different angles at high resolution. The online 3D atlas of arthropod external morphology serves primarily as a digital teaching aid in courses of invertebrate biology, advances the awareness of arthropod biodiversity in general public, and promotes the scientific activity at the University of Ljubljana. We plan to expand the 3D atlas database in two future directions: (i) expand the set of scanned species with additional representatives, to more exhaustively cover the arthropod diversity; (ii) provide in-depth analyses of arthropod body plan, with additional segmentation of the appendages, mouthparts and visualization of internal organ systems (Fig 2B).

Acknowledgements: The project is funded under the development framework of University of Ljubljana. The purchase of the Neoscan N80 microtomograph was co-financed by the Republic of Slovenia, Ministry of Education, Science, and Sport and the European Union from the European Regional Development Fund. The microtomograph, sample preparation laboratory, and supporting

computer equipment are part of the infrastructure center “IC Microscopy of Biological Samples” at the Faculty of Biotechnology (MRIC UL, I0-0022-0481-08), which is part of the University of Ljubljana’s Network of Infrastructure Centers. We thank the students Vito Ham, Vesna Jurjevič, Gaj Kušar and Adrijan Samuel Stell Pičman who participated in the project.

Author contributions: UB performed X-ray microtomography scans of arthropods, 3D data processing and generation of 3D models. GB, TD, ŽF, RV, MV and VZ provided descriptions and photographs of included arthropod species. CF and RK are the project leaders.

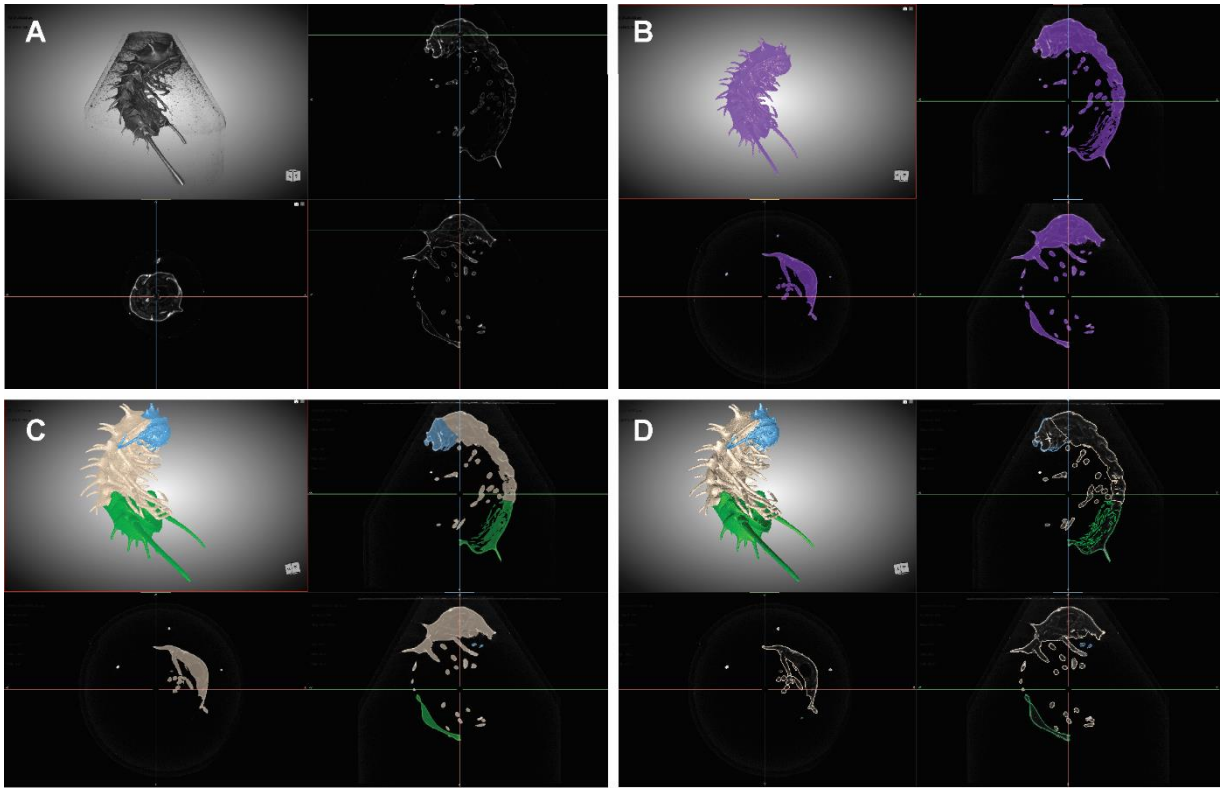

Figure 1: Processing of the 3D dataset. 3D dataset reconstructed from X-ray projection images (A), segmentation of the full body (B), segmentation of body regions (C), generation of 3D surface meshes used in the representation of the specimen in the 3D Atlas (D).

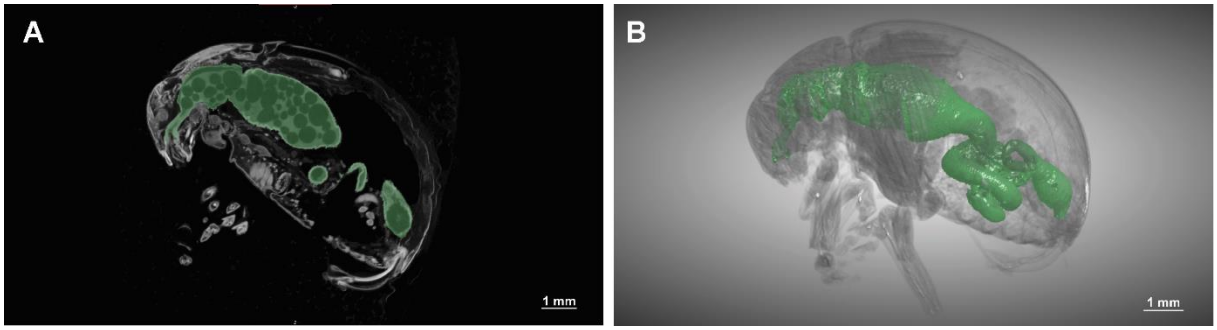

Figure 2: Imaging the 3D anatomy of digestive system in a Colorado potato beetle. Segmentation of the digestive system (A), 3D anatomy of the digestive tract inside of an adult beetle (B).

Structure and nanostructure of the light rare-earths based $Ce_xPrNdSm$ (x = 0.01–1.5) medium-entropy alloys, leading to an unconventional magnetic state

Andreja Jelen[1], Julia Petrović[1], Stanislav Vrtnik[1,2], Primož Koželj[1,2], Jože Luzar[1,2], Peter Mihor[1], Goran Dražič[3], Gregor Kapun[3], Janez Dolinšek[1,2]

[1]*J. Stefan Institute, Ljubljana, Slovenia*

[2]*Faculty of Mathematics and Physics, University of Ljubljana, Slovenia;*

[3]*National Institute of Chemistry, Ljubljana, Slovenia*

We present a study of structure, microstructure, nanostructure and magnetic state of the $Ce_xPrNdSm$ (x = 0.01–1.5) medium-entropy alloys composed of the light rare earths only. Magnetic light rare earths are fundamentally different from the heavy ones, because the crystal-field interaction in the former is able to reduce or completely destroy the ionic magnetic moments at low temperatures. The alloys crystallize in a double hexagonal close-packed structure in the form of a single-phase nanostructured solid solution. The low-temperature magnetic state is inhomogeneous, being a mixture of paramagnetic domains appearing in the crystal regions with larger destruction of the moments and spin glass (SG)-type spin domains in the regions with less destructed moments.

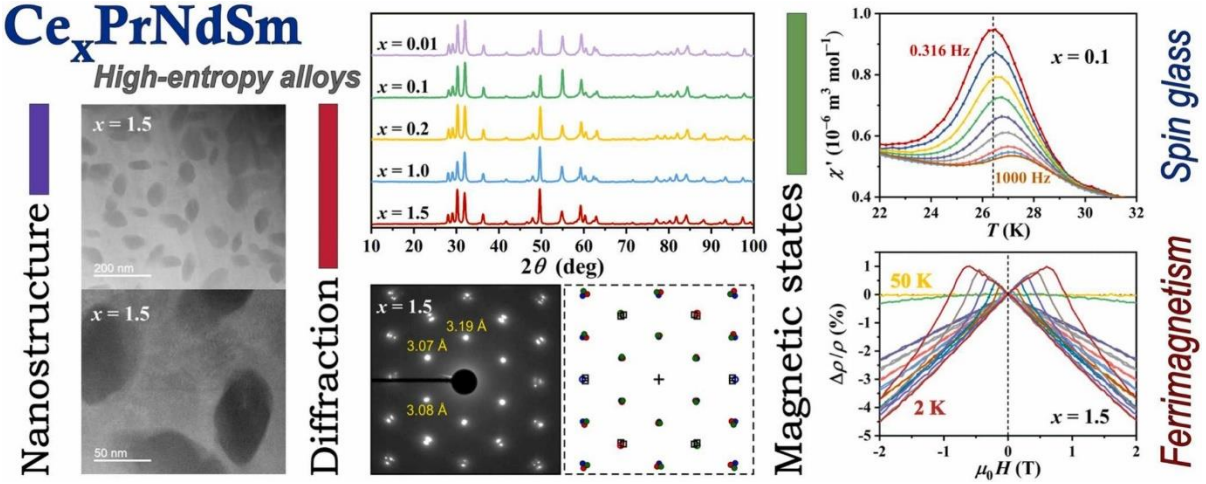

Reference: J. Petrović, S. Vrtnik, A. Jelen et al. Materials Today Communications 51 (2026) 114898.

Structure of Ni-Substituted Barium Ferrite Magnetic Nanoplatelets Synthesized via a Hydrothermal Method: From Stabilization of a β-Alumina-Type Defect Structure to Exchange-Coupled Spinel Ferrite–M-Type Hexaferrite Nanocomposites

Darko Makovec

Department for Materials Synthesis, Jožef Stefan Institute, Ljubljana, Slovenia

Introduction

Barium hexaferrite nanoplatelets exhibit extraordinary magnetic properties dominated by orientation of the magnetic moments perpendicular to the NPLs' basal planes. This extraordinary property in a combination with the platelet shape and the colloidal stability in different liquid media has already led to many innovative applications, including the first ferromagnetic fluids, magneto-optical suspensions and composites, and in medicine [1].

Hexaferrite nanoplatelets exhibit size-dependent structural variations that strongly influence their magnetic properties [2,3]. Here, we investigate the structure of hydrothermally synthesized Ni-substituted barium ferrite nanoplatelets and their annealing-driven structural evolution into epitaxial hexaferrite–nickel ferrite hard–soft exchange-coupled nanocomposites.

Methods

The crystalline structure of the Ni-substituted barium ferrite nanoplates was studied with a probe aberration-corrected STEM (JEOL ARM 200CF operated at 80 kV and Thermo Fisher Scientific Spectra 300 operated at 200 kV).

Results

Incorporation of Ni^{2+} into barium ferrite nanoplatelets induced significant changes in their crystal structure, leading to a severe reduction of magnetic properties already at low Ni^{2+} contents below the solubility limit ($x \approx 0.08$ in the nominal $BaFe_{12-x}Ni_xO_{19}$ composition). In particular, HAADF imaging revealed that the Fe(2b) trigonal lattice sites of the M-type hexaferrite structure were unoccupied in the substituted nanoplatelets. Furthermore, iDPC imaging indicated that depletion of the Fe(2b) sites was accompanied by the formation of neighboring oxygen vacancies. These Fe(2b)–2O vacancy complexes are characteristic of the formation of a β-alumina-type ferrite structure. The structural observations obtained by STEM imaging were confirmed by quantitative EDXS analysis of the nanoplatelet composition.

Exceeding the effective solubility limit of Ni^{2+} in the barium ferrite nanoplatelets led to the epitaxial growth of spinel nickel ferrite on the basal surfaces of the hexaferrite nanoplatelets, yielding composite nanoplatelets consisting of a thin hexaferrite lamella confined between two epitaxial spinel ferrite layers (Figure 2).

Upon annealing at 800 °C, the M-type hexaferrite structure was restored and the Ni-substituted nanoplatelets recovered magnetic properties characteristic of Ni-substituted M-type barium hexaferrite. Annealing of the composite hexaferrite–spinel ferrite nanoplatelets at 800 °C preserved the composite architecture and resulted in rigid hard–soft exchange coupling. In contrast, higher-temperature treatment (1000 °C) produced kinetically stabilized, irregular spinel ferrite–hexaferrite intergrowths rather than the equilibrium W-type hexaferrite predicted by phase equilibria.

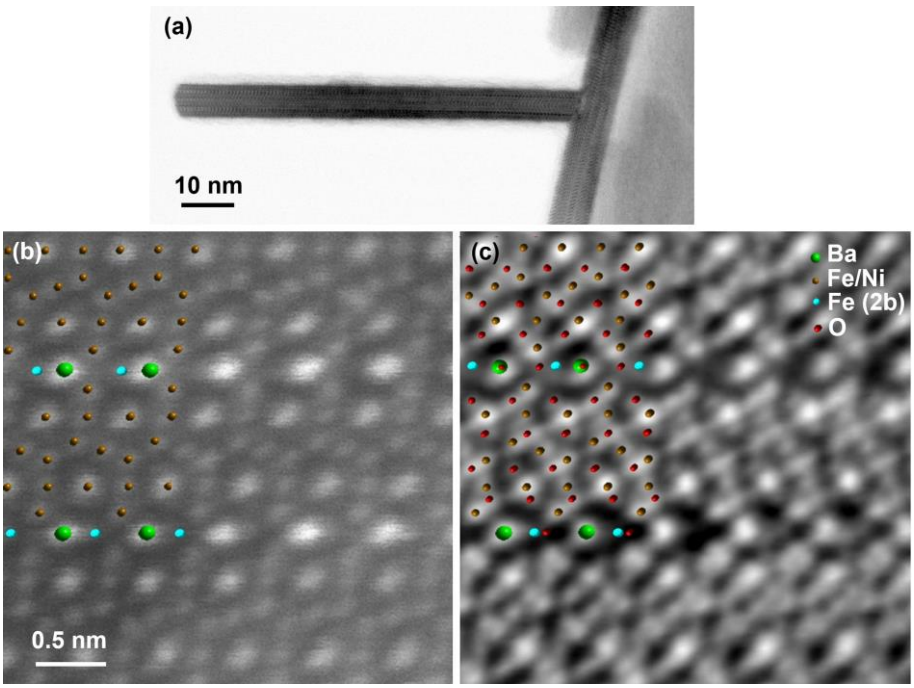

Figure 1. BF (a), HAADF (b) and iDPC images of substituted barium-ferrite nanoplatelet.

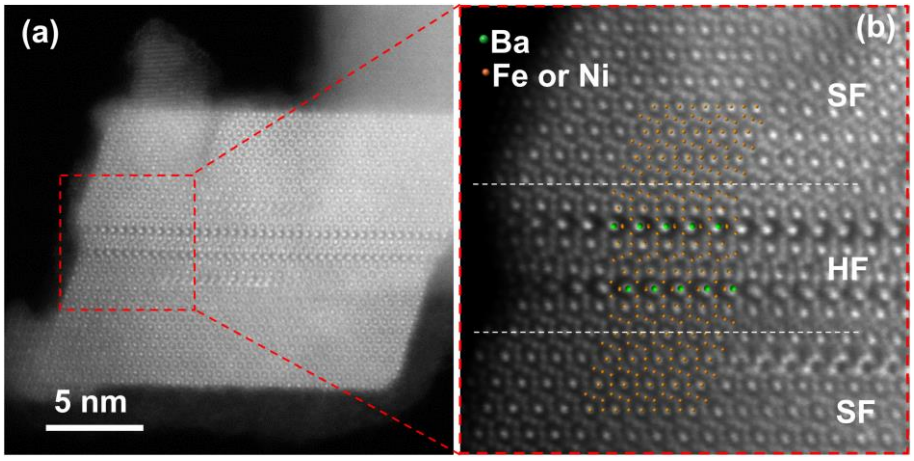

Figure 2. HAADF STEM images of composite nanoplatelet. Structural models of the cubic spinel nickel ferrite (SF) and hexaferrite (HF) structures are superimposed on Figure (b) to illustrate the positions of Ba and Fe/Ni atomic columns.

References:

[1] D. Lisjak, A. Mertelj, Prog. Mater. Sci., **95**, (2018) 286-328.
[2] D. Makovec, B. Belec T. Goršak, *et al.*, Nanoscale **10** (2018) 14480-14491.
[3] B. Belec, G. Dražić, S. Gyergyek, *et al.*, Nanoscale **9** (2017) 17551–17560.

Abiotic and biotic models: a comparative approach for the study of brain mineralogy

Giulia Pia Servetto[1], Alessandra Passarella[1], Ginevra Mango[1], Francesca Montarolo[2], Eriola Hoxha[2], Filippo Tempia[2], Goran Dražić[3], Nada Žnidaršič[4], Enrico Destefanis[1], Ruggero Vigliaturo[1].

[1]*Department of Earth Sciences, University of Turin, Via Valperga Caluso 35, 10125, Turin, Italy*

[2]*Department of Neuroscience of the University of Turin and Neuroscience Institute Cavalieri Ottolenghi, Regione Gonzole 10, 10043 Orbassano, Italy*

[3]*National Institute of Chemistry, Hajdrihova ulica 19, 1000 Ljubljana, Slovenia*

[4]*Biotechnical Faculty, University of Ljubljana, Jamnikarjeva 101, 1000 Ljubljana, Slovenia*

Contact email: giuliapia.servetto@unito.it

Exogenous mineral phases, including magnetite (Fe_3O_4) nanoparticles (NPs), have been detected in the human brain after individuals' exposure to urban particulate matter. The physicochemical state of these NPs and the mechanisms by which they interact with host tissues remain poorly characterized and understood.
The main goal of this study was to characterize exogenous NPs after their exposure to different abiotic and biotic models presenting a generic mammalian brain environment at increasing levels of system complexity. These investigations aimed to evaluate the physicochemical alteration of the magnetite NPs mineralogy when exposed to the surrounding biochemical environments.

We conducted dissolution experiments of magnetite NPs (50-100 nm) with abiotic models such as simulated biofluid (SBF) and simulated soft tissues (SST). In parallel, we used as biotic model cultured mice brain tissues (CMBT), specifically olfactory bulb and frontal cortical regions, exposed to magnetite NPs. After the exposure, CMBT samples were split into two subsamples: one chemically fixed and resin embedded for ultramicrotomy, and the other one chemically digested (in NaClO solution at 13%) to extract the NPs of interest. A combination of analytical techniques was used, such as Powder X-Rays Diffraction (PXRD), Inductively Coupled Plasma Mass Spectroscopy (ICP-MS), inverted optical microscope, Scanning Electron Microscope equipped with X-Rays Energy Dispersive Spectroscopy (SEM-XEDS), probe Cs-corrected Scanning High-Resolution Transmission Electron Microscope (HR S/TEM) coupled with electron diffraction, XEDS elemental mapping, and Dual-range Electron Energy-Loss Spectroscopy (Dual-EELS). PXRD qualitative analysis highlighted the bulk crystallinity of magnetite NPs. ICP-MS confirmed that magnetite NPs tend to adsorb free metal ions due to NPs surface defects. The vertical dimensional distribution measured on the SST optical microscope acquisitions revealed that there is a quite homogeneous distribution of magnetite NP aggregates in the SST section, suggesting that magnetite NP aggregates interacted with the entire aggregate surface exposed to the SST. Moreover, pre- and post- interacted magnetite NPs exposed to abiotic models showed some alterations, especially on the nanoscale. Some of the post- interacted magnetite NPs showed interplanar distances at the boundary that are more compatible to ferric Fe-oxide such as lepidocrocite (γ-FeO(OH)), goethite (α-Fe^{3+}O(OH)), and others were more compatible to the ferrous Fe-oxide wüstite (FeO) rather than magnetite. The ultrastructural localization of magnetite in CMBT ultrathin sections confirmed the effective internalization of NPs of interest within the tissues, while the mineralogical characterization of magnetite NPs conducted on chemically digested CMBT confirmed the alteration of magnetite NPs boundary after the interaction with CMBT like the post- interacted magnetite NPs with abiotic models.

The combination of abiotic and biotic models proved efficient for investigating the alteration of magnetite NPs, and future works will be performed using more complex abiotic models, as well as *in vivo* experiments.

Live Imaging of Spatial Calcium Signatures in Potato Roots and Leaves During Interaction with Endophytic Bacteria

Katja Fink[1], Miha Tome[1], Sergej Praček[1], Anže Županič[1], Lara Likar[1], Tina Arnšek[1], Kristina Gruden[1]

[1] *Department of Biotechnology and Systems Biology, National Institute of Slovenia, Ljubljana, Slovenia*

Contact email: katja.fink@nib.si

Introduction:
Plants rely on complex signalling networks to perceive microbial signals and activate appropriate immune responses. Beneficial endophytic bacteria, such as *Bacillus subtilis* and *Paenibacillus sp*., have been shown to enhance plant resistance to pathogens including potato virus Y [1], although the spatial and temporal dynamics of the underlying signalling processes remain poorly understood. The main objective of this study is to characterize calcium-based signalling patterns and hormone-associated responses induced by beneficial microbes and local tissue damage in potato plants**.**

Methods:
We employ transgenic potato lines expressing genetically encoded fluorescent sensors for cytosolic calcium, GCaMP3 and stress-related hormonal signalling pathways (jasmonic and salicylic acid). Immune responses are monitored in intact leaves and roots under controlled biotic stress conditions. Endophytic bacteria are applied either to the root system or locally to leaf tissues, combined with mechanical wounding to simulate natural stress scenarios. Real-time imaging is performed using live confocal microscopy, including a long working distance objective that enables minimally invasive monitoring of intracellular calcium dynamics in intact plant tissues. Imaging protocols are optimized to improve signal stability during extended time-lapse acquisition. Spatial signal propagation and temporal response characteristics are analysed at the cellular level.

Results:
Preliminary observations indicate that both beneficial bacterial application and local leaf wounding trigger rapid and spatially structured calcium transients in potato tissues. Distinct signal propagation patterns are observed between roots and leaves, suggesting tissue-specific modulation of immune signalling. Initial experiments further suggest that beneficial bacteria may influence the pattern of calcium responses associated with stress perception.

Discussion and conclusions:
Our methodological framework enables high-resolution tracking of calcium signalling dynamics in physiologically intact plants with minimal disturbance. The observed spatial complexity of calcium responses supports the concept of a tissue-dependent calcium signalling code involved in beneficial-mediated immune priming [2]. This approach provides a valuable platform for dissecting interactions between calcium signalling and hormonal pathways during plant–microbe interactions. Future work will focus on quantitative analysis of signal signatures and their correlation with downstream defense gene expression and hormonal signalling in stress response, contributing to the development of sustainable crop protection strategies.

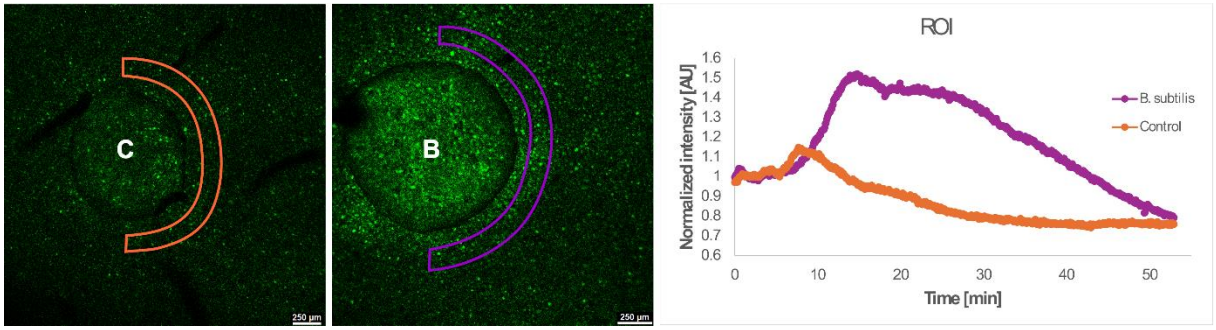

Figure 1: Calcium dynamics following *B. subtilis* stimulation. Application of a droplet containing *B. subtilis* ("B") or water as a control ("C") onto leaves of calcium sensor plants (GCaMP3) triggered calcium fluxes in epidermal cells. Regions of interest used for quantification (right image) were selected from confocal images at an equal distance from the droplet application site (orange: control, purple: *B. subtilis*). Scale bar: 250 µm.

References

1. J.N. Kalatskaja et al., *Int. J. Plant Biol.* **2023**, *14*, 312-328.
2. A. Bhar et al., *Front. Plant Sci.* **2023**, *14*, 1138252.

The quaternary W-based refractory alloy for fusion application

Andreja Gajović[a], Sandra Drev[b], Kristina Tomić Luketić[a], Toni Dunatov[a], Mario Matić[a], Juraj Ovčar[a], Miha Gunde[a], Jasminka Popović[a], Željko Skoko[c], Tonči Tadić[a], Miran Čeh[b]

[a]*Ruđer Bošković Institute, (Zagreb), Croatia*

[b]*Jožef Stefan Institute, (Ljubljana), Slovenia*

[c]*University of Zagreb, Faculty of Science, Department of Physics, (Zagreb), Croatia*

Contact email: Andreja.Gajovic@irb.hr

Introduction: Development of fusion-based power plants (FPPs) is of paramount importance for the European Green Deal initiative of lowering carbon emissions, since FPPs do not generate CO_2 or other substance harmful to the atmosphere. In the context of achieving FPP reliability, one of the important points is the effect of high energy fusion neutrons (MeV range) on the component materials of the fusion reactor. Tungsten and tungsten-based alloys are defined as high heat flux (about 10 MW/m^2) materials for plasma facing components e.g. first wall and diverter [1]. To prepare and study larger number of different compositions of alloys as candidates for fusion materials, magnetron sputtering is shown as method of choice. Since quaternary W-based alloy WTaVCr could be promising fusion material with highly resistant to irradiation [2], we prepared WTaVCr thin films and studied its structural properties as well as chemical composition before and after irradiation by heavy ions.

Methods: By magnetron sputtering, we deposited WTaVCr films of variable thicknesses on a silicon substrate. The films were characterized using X-ray diffraction (XRD), scanning electron microscopy (SEM), energy-dispersive X-ray spectroscopy (EDS) and atomic resolution scanning transmission electron microscopy (STEM), both before and after irradiating the samples by heavy ions (Cu) accelerated to 8 MeV in RBI accelerator center. Moreover, a highly-performant machine-learned interatomic potential [3] was employed to perform atomistic simulations of bulk and surface WTaVCr.

Results: In as-deposited WTaVCr thin film samples, XRD measurements have revealed the co-existence of two high entropy alloy phases, both characterized by body-centered cubic (BCC) crystal structures with differing unit cell parameters. As-deposited sample of 1 μm thickness dominantly contains BCC structure with a unit-cell parameter a=3.191(2) Å with interplanar distances d_{011}=2.25 Å and d_{022}=1.13 Å (Figure 1a), and minority BCC phase with unit-cell parameter a=3.126(3) Å (with interplanar distance of d_{011}=2.21 Å). In as-deposited sample of 2 μm thickness the amount of phase with BCC having larger unit-cell parameter, a=3.191(2) Å, decreased while the BCC phase having smaller unit-cell parameter, a=3.126(3) Å, increased. Moreover, the heating of the 1 μm thick WTaVCr thin film also induce the same phenomena of increase of the amount of BCC phase with smaller unit-cell parameter. Finaly, after irradiating as-deposited sample of 1 μm thickness with 8 MeV heavy ions (Cu) in dose of 1 dpa we observed that it caused complete transition of the film in the BCC phase with the smaller unit cell (a=3.126(3) Å), initially found in the minority of the as-deposited samples.

The observed phenomena, that the increase of the amount of phase with the smaller unit cell by increasing the thickness of the film or by heating the film, indicated possible relaxation of the WTaVCr crystal lattice. Therefore, the complete transition of the film to the phase with the smaller unit cell by bombardment with 8 MeV heavy ions indicated that irradiation induce ordering of the crystal lattice instead of an expected increase of the defects. To elucidate the observed phenomena and confirm whether irradiation really induce the relaxation of crystal lattice, theoretical simulations of bulk and surface WTaVCr were performed. Probability of WTaVCr to form a BCC bulk crystal of unit cell length "a" as calculated using the tabGAP [4] machine-learning interatomic potential is shown in Figure 1 b). The simulation indicates that 3.12 is the global minimum of WTaVCr BCC crystal lattice.

This statement has approved experimentally by EDS. EDS measurements in SEM as well as STEM imaging in combination with EDS mapping show that all the elements (W, Ta, V and Cr) are homogenously distributed in all the crystal grains in sample irradiated by 8 MeV heavy ions (Figure 2), while the measured atomic ratio of elements observed in crystal lattice of as-deposited sample in comparison to their ratio after irradiation was comparable, within statistical deviation.

Discussion and conclusions: In the course of Rietveld refinements, the line broadening analysis has also been conducted. It was found that line profiles of WTaVCr structure with larger unit-cell (present in as-deposited sample) are broader compared to those of WTaVCr structure with smaller unit-cell obtained after the irradiation. Such broadening is caused by the presence of significant distortions within the crystal lattice of as-prepared sample due to the different atomic radii occupying the same crystallographic position yielding the micro-strain value ϵ that is significantly larger compared to the micro-strain present in the irradiated WTaVCr having smaller unit-cell. Observed decrease in micro-strain indicates that the irradiation causes the significant reduction in number of distortions and the relaxation of deformations originally present within the as-prepared crystal lattice finally also leading to the observed decrease of unit-cell parameters.

From these observations and theoretical analysis, we conclude that the system, as initially deposited, is located in a substrate-induced local minimum, while irradiation of the quaternary W-based alloy WTaVCr induce relaxation in thermodynamically stabile phase.

Acknowledgment: This work has been supported by European union NextGenerationEU within RBI program KP3-25 and by Croatian Science Foundation under the project IP-2025-02-7971.

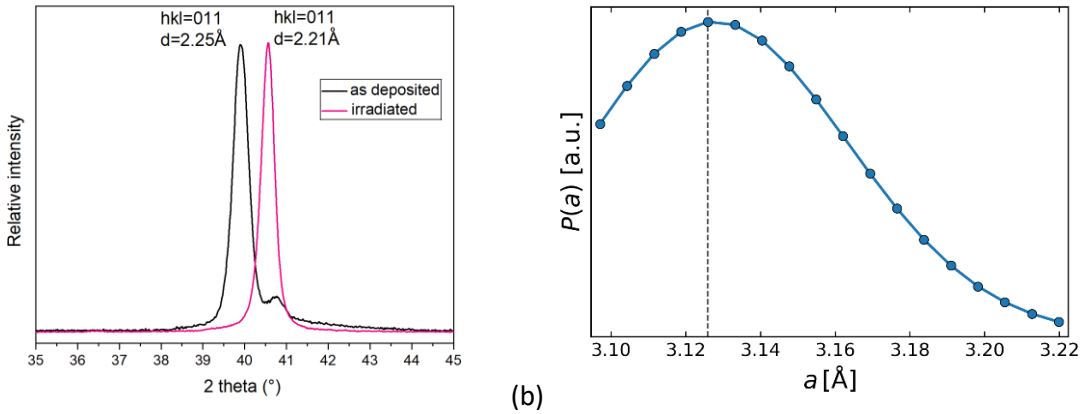

(a) (b)

Figure 1: X-ray diffraction pattern of WTaVCr film as deposited and after irradiation by 8MeV Cu (a), probability of WTaVCr to form a BCC bulk crystal of unit cell length "a" (b).

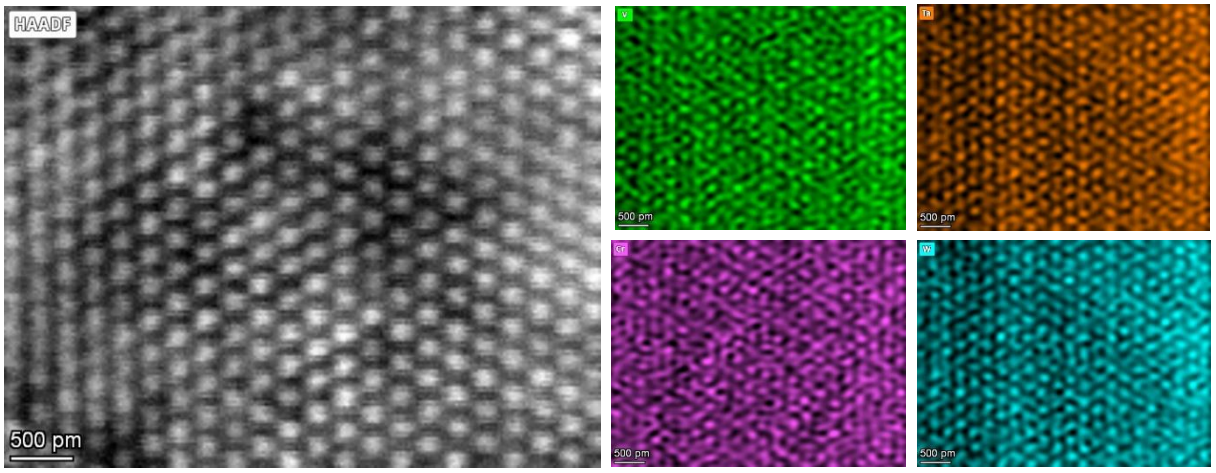

Figure 2: HAADF and EDS maps of WTaVCr film after irradiation *by 8 MeV Cu*. Scale bars are *5*00 pm.

References:

1. G. Pintsuk, G. Aiello, S. L. Dudarev, M. Gorley, J. Henry, M. Richou, M. Rieth, D. Terentyev, R. Vila, *Fusion Eng. Des.* **2022**, *174*, 112994.
2. O. El-Atwani, N. Li, M. Li, A. Devaraj, J. K. S. Baldwin, M. M. Schneider, D. Sobieraj, J. S. Wróbel, D. Nguyen-Manh, S. A. Maloy, E. Martinez, *Sci. Adv.* **2019**, *5* (3), eaav2002.
3. J. Byggmästar, D. Sobieraj, J. S. Wróbel, D. K. Schreiber, O. El-Atwani, E. Martinez, D. Nguyen-Manh, *Acta Materialia* **2025**, 121276.
4. J. Byggmästar, K. Nordlund, F. Djurabekova, *Phys. Rev. Materials* **2022,** *6*, 083801.

Combining 4D-STEM with Machine Learning for Ferroelectric Materials Characterization

Goran Dražić [a,b,c], Katarina Žiberna [b,c], Janina Roknić [b,c], Matic Poberžnik [d], Anton Kokalj [d], Matej Martinc [e], Sašo Džeroski [e] and Andreja Benčan Golob [b,c]

[a]*Department of Materials Chemistry, National Institute of Chemistry, Ljubljana, Slovenia*

[b]*Electronic Ceramics Department, Jožef Stefan Institute, Ljubljana, Slovenia*

[c]*Jožef Stefan International Postgraduate School, Ljubljana, Slovenia*

[d]*Physical and Organic Chemistry Department, Jožef Stefan Institute, Ljubljana, Slovenia*

[e]*Knowledge Technologies Department, Jožef Stefan Institute, Ljubljana, Slovenia*

Contact email: goran.drazic@ki.si

Four-dimensional scanning transmission electron microscopy (4D-STEM) provides a powerful platform for studying ferroelectric materials. By recording diffraction patterns at every point of a scanned region, the technique enables atomic-scale mapping of local electrostatic fields, yielding insights into the local atomic arrangement, polarisation vector, and crystallographic defects [1]. Such detailed structural insight is essential for clarifying switching behaviour and improving material performance in devices like actuators and sensors; however, reliably determining specific parameters such as polarisation orientation remains difficult in certain material families.

Here, we concentrate on lead-free sodium potassium niobate (KNN), where standard polarisation analysis approaches encounter limitations. We therefore explore a strategy for identifying polarisation orientation and point defects (e.g., vacancies in cation and oxygen sublattices) by merging conventional STEM and 4D-STEM analysis with an artificial intelligence (AI) framework.

To achieve this, experimental 4D-STEM data were collected on two Cs probe-corrected instruments: an ARM 200CF (JEOL) equipped with a Merlin pixelated detector (Quantum Detectors) and a Spectra 300 (Thermo Fisher Scientific) fitted with an EMPAD pixelated detector. In parallel, we used QSTEM software [2] to simulate 4D-STEM datasets from crystallographic KNN models with different polarisation directions and defect levels. These models, including their point defects, were structurally optimised using density functional theory (DFT) as implemented in Quantum ESPRESSO [3]. The resulting simulated data served as training material for neural networks.

From the experimental 4D-STEM datasets, we derived centre-of-mass shift vector fields, which reflect the momentum imparted to the electron beam by local electrostatic potentials. These vector fields enabled the extraction of differential charge density distributions for both defect-free KNN and structures containing point defects. Notably, the charge density maps obtained from 4D-STEM closely matched those from direct DFT calculations. Additionally, by applying a machine-learning approach, we were able to pinpoint the positions of oxygen vacancies within the model structures [4]. Based on these outcomes, we will discuss the advantages of integrating simulations, 4D-STEM, and machine learning for determining the magnitude and orientation of polarisation and for detecting structural defects in complex oxide systems.

This work is supported by the Slovenian Research and Innovation Agency (Projects No. P2-0105, P2-0103, P2-0393, J7-4637, J2-70101, and GC-0001).

References:
[1] C. Ophus, Microscopy and Microanalysis, **2019**, 25, 563–582
[2] C. Koch, Determination of core structure periodicity and point defect density using quantitative high-resolution transmission electron microscopy, **2002**, Ph.D. thesis, Arizona State University
[3] P. Giannozzi et al., J. Phys.: Condens. Matter, **2017**, 29, 465901
[4] M. Martinc et al., arXiv:2603.15582, **2026**

Razbijanje mitov: Razširitev področja uporabe sodobnih večionskih plazemskih sistemov FIB

Gregor Kapun[a], Jan Jerovšek[a], Blaž Jaklič[b], Jan Žuntar[b], Tara Gudžulić[b], Saša Kos[b], Goran Dražić[a], Robert Dominko[a]

[a]*Kemijski inštitut, Ljubljana, Slovenija*

[b]*Institut Jožef Stefan, Ljubljana, Slovenija*

Kontaktni email: gregor.kapun@ki.si

V znanstveni skupnosti se je tehnologije plazemskega fokusiranega ionskega snopa (pFIB) oprijel sloves orodja, namenjenega izključno hitri obdelavi velikih prečnih prerezov in 3D volumnov. Še vedno prevladuje zmotno prepričanje, da pFIB ne dosega natančnosti, kakovosti depozicije in čistoče, ki so potrebne za zahtevne nanostrukturne aplikacije, tradicionalno rezervirane za sisteme z galijevim (Ga) virom. V pričujočem delu te mite izpodbijamo s prikazom zmogljivosti sodobnega sistema Helios Hydra 5 UX z večionskim virom (Xe^+, Ar^+, O^+ in N^+). Dokazujemo, da pFIB ni le konkurenčna alternativa, temveč v vrsti naprednih aplikacij celo prekaša standardne sisteme Ga-FIB.

Tako imenovani »mit o natančnosti« smo naslovili z implementacijo naprednih algoritmov za oblikovanje snopa in uporabo orodja AutoScript za optimizirano poravnavo kolone. Dosežen dinamični razpon ionskih tokov (od 2,5 µA do 1 pA) je omogočil izjemno natančno, t.i. »kirurško« obdelavo vzorcev na nanometrski skali. Rezultati so pokazali, da uporaba argonovih ionov (Ar^+) pri nizkih pospeševalnih napetostih (2 kV ali manj) v končni fazi poliranja omogoča pripravo TEM lamel s tanjšo amorfno plastjo in čistejšimi faznimi mejami kot pri uporabi Ga+. To je ključnega pomena predvsem pri materialih, občutljivih na galij, kjer je nezaželeno formiranje zlitin pogosto kritična težava. Posebno pozornost smo posvetili vprašanjem kontaminacije in zanesljivosti. Raziskali smo učinkovitost integriranega zaščitnega zaklopa, ki varuje elektronsko kolono in detektor EDX tudi pri nizkih tokovih (do 1 nA). V povezavi s krio-mizo (Cryo-Stage) sistem deluje kot učinkovita past za kontaminante; hlapni produkti, nastali pri ionskem jedkanju, se prednostno odlagajo na najhladnejših površinah, kar ščiti objektivni del kolone in vanjo integrirane detektorje ter zagotavlja ultra-čisto vakuumsko okolje. Takšna konfiguracija omogoča tudi hitro ionsko jedkanje polimerov in lahkih elementov pri tokovih do 2,5 µA brez nezaželenega termičnega taljenja vzorca. Na področju nanofabrikacije smo s ksenonovim snopom (pri 12 kV) dosegli ionsko inducirano nanašanje (IBID) platine z znatno višjo prevodnostjo v primerjavi z Ga-FIB, kar pripisujemo manjši vsebnosti ogljika v depozitu in odsotnosti implantacije galija. Navpične progaste artefakte (curtaining) na velikih površinah smo uspešno odpravili z uporabo tehnologij rotacijske ionske erozije (Spin Milling) in nihajne ionske erozije (Rocking Mill), ki zagotavljata zrcalno gladko površino prečnih prerezov.

V zaključni fazi smo preučili vpliv strojnega učenja (ML) na avtomatizacijo procesov v ekosistemu Helios Hydra 5 UX. Integracija algoritmov na podlagi nevronskih mrež v programsko opremo AutoTEM 5 in Auto Slice & View 5 predstavlja ključen premik v zanesljivosti delovanja. Za razliko od klasične korelacije sivin ti algoritmi omogočajo robustno sledenje tudi degradiranih ali delno uničenih orientirnih markerjev (fiducials), kar zagotavlja stabilnost v okoljih z nizkim kontrastom. Tehnologija omogoča avtomatizirano poravnavo snopa, fokusa in stigmatorjev, kar učinkovito zmanjšuje vrzel v ločljivosti med plazemskimi in galijevimi viri ter zagotavlja vrhunsko kakovost obdelave brez primere v prejšnjih generacijah plazemskih naprav.

Viri:

1. Vasquez, D. R., et al., Microscopy and Microanalysis, **2025**, 31(7): 36–37.
2. Mulcahy, N., et al., Nanoscale Horizons, **2025**, 10(12): 3486–3498.
3. Slamkova, D., et al., Thermo Fisher Scientific, **2022**, Application Note AN0174.
4. Thermo Fisher Scientific, **2024**, Technical Datasheet DS0517.

Nanoscale Elasticity and Plasticity in Ferroelectric Perovskites

Andreja Benčan Golob[a], Katarina Žiberna[a], Hana Uršič[a], Goran Dražić[b]

[a]*Electronic Ceramics Department, Jožef Stefan Institute, Ljubljana, Slovenia*

[b]*Department of Materials Chemistry, National Institute of Chemistry, Ljubljana, Slovenia*

Contact email: andreja.bencan@ijs.si

The nanoscale mechanical behavior of ferroelectric perovskites is critical for the reliability of microelectromechanical systems. Using nanoindentation in combination with various advanced electron microscopy techniques and atomic force microscopy, we investigate how microstructural features, grains, pores, and domain architecture, govern the elastic and plastic properties of three separate systems.

For $0.9Pb(Mg_{1/3}Nb_{2/3})O_3–0.1PbTiO_3$ thick films fabricated by aerosol deposition, post-deposition annealing induces pore redistribution and local grain growth, increasing hardness and Young's modulus by ~16% through film densification and substrate modification, while the unique nanostructure maintains crack resistance [1].

In polycrystalline $BiFeO_3$ ceramics, nanoindentation from 200 µN to 2 mN reveals decreasing hardness (9.9 to 7.7 GPa) and reduced modulus (113.7 to 90.9 GPa). The indentation size effect governs hardness evolution, while modulus reduction reflects microstructural defects within the growing interaction volume. First pop-in analysis uncovers a sequence of plastic deformation mechanisms through homogeneous dislocation nucleation, dislocation multiplication into arrays, and grain subdivision, phenomena resembling metallic behavior rather than typical ceramic deformation [2].

In $(K_{0.5}Na_{0.5})NbO_3$ single crystals, the reduced elastic modulus is highly domain-dependent. While the average modulus is ~130 GPa, 20% anisotropy is observed across 90° domain walls, with one side elastically harder and the other softer, whereas 60° domain walls exhibit no mechanical contrast. Elasticity also varies between domains with differing piezoelectric activity, demonstrating a complex structure-property relationship influenced by both intrinsic domain wall properties and extrinsic contributions from neighbouring domains and tip interactions.

References:

[1] K. Žiberna, M. Šadl, A. Drnovšek, G. Dražić, H. Uršič Nemevšek, A. Benčan, Crystals. **2023**, *13*, 3, 1-10.

[2] K. Žiberna, M. Koblar, M. Bah, F. Levassort, G. Dražić, H. Uršič Nemevšek, A. Benčan, Journal of the European Ceramic Society, **2024**, *44*, 12,7025-7031.

[3] K. Žiberna, M. Koblar, A. Bradeško, M. Bah, F. Levassort, G. Dražić, H. Uršič Nemevšek, A. Benčan, Journal of the European Ceramic Society, **2025**, *45*, 15, 117566 1-5.

3D Visualisation of Wood: 3D X-ray computed microtomography and 3D printing

Rožle Repič[1], Lidija Korat Bensa[1], Daša Krapež[2], Maks Merela[2]

[1]*Slovenian National Building and Civil Engineering Institute, Department of Materials, (Ljubljana), Slovenia*

[2]*University of Ljubljana, Biotechnical Faculty, Department of Wood Science and Technology, (Ljubljana), Slovenia*

Contact email: rozle.repic@zag.si

Introduction Research in the field of wood science often involves the study of fresh, technological, or archaeological samples, which vary greatly in terms of their characteristics and preparation methods for conventional observation techniques such as microscopy. X-ray computed microtomography (µCT) has emerged as an important method, particularly for degraded or archaeological wood, as it eliminates the need for sample preparation such as cutting, drying, or sputtering. This allows valuable artifacts to be viewed in their natural state, maintaining structural integrity for further analysis or long term monitoring. µCT analysis in the field of heritage science enables non-invasive insight into the internal structure of artifacts, supporting detailed material analysis and conservation planning. In addition, it allows for digital archiving, enables access to data for the wider research community, and facilitates the production of precise 3D replicas. This research focuses on utilizing µCT data not only for visualization but also for the development of 3D-printed physical replicas using advanced biocomposite filaments.

Methods The internal structures of wood samples including spruce, pine, beech, and oak were scanned at submicron resolution using an Xradia µCT-400 (Xradia, USA) or an EasyTOM XL Ultra µCT (RX Systems, France) system. At least 1,601 projections were acquired during a full 360° rotation. Computer-aided 3D reconstruction of acquired datasets was performed using X-ACT software (RX Solutions) or XRM Reconstructor (Xradia, USA). After reconstruction, advanced image filtering, segmentation, and 3D object preparation (e.g., .stl files) were performed using Avizio Fire software (Thermo Fisher Scientific, USA). For filament production, wood particles were sieved through a 237 µm mesh and compounded with polylactic acid (PLA). These filaments contained wood particle ratios ranging from 10% to 20%. Final physical models were fabricated at a 1:500 scale using fused filament fabrication (FFF) on Prusa XL (Prusa, CZ) or Creality (Creality, CN) printers.

Results Reconstructed datasets enabled the digital histological sectioning in any orientation, which is crucial for dendrochronological studies and wood identification without damaging the original sample. Slices can be oriented in space after scanning, which is most practical for further analysis and eliminates the need for oriented sample preparation. Research into filament quality showed that thermal modification (TM) of wood particles at 200 °C significantly improved the composite properties. Filaments with TM particles exhibited lower surface roughness and reduced porosity compared to those with non-modified particles.

Discussion and conclusions The synergy of µCT and 3D printing represents a powerful advancement for wood science and cultural heritage conservation among others. µCT is now widely used for non-destructive wood identification and anatomical analysis, including especially fragile heritage objects where sampling is unacceptable. At the same time, 3D scanning and printing are emerging technologies to document, reproduce, and present in example cultural heritage and wider in accessible and didactic forms. Presented work is at the intersection of these developments, using µCT not only for diagnosis, analysis and documentation, but as a strong and accurate basis for manufacturing enlarged or even didactic models. The enlarged µCT-based models presented here makes micron sized

anatomical features and hidden damage accessible to students, conservators, and the public. This approach is particularly promising in example for historical musical instruments and other high-value objects, where internal structure is critical to interpretation and conservation decisions, but is inaccessible by conventional imaging techniques. While commercial filaments use fine wood flour (particle size < 100 µm), this study justifies the use of larger particles to act as a reinforcement, given that extrusion parameters are optimized to prevent nozzle clogging. It expands the design space of wood–polymer composites beyond conventional formulations and suggests a route to mechanically more robust and stable prints. The resulting 3D-printed replicas serve as state-of-the-art educational tools, providing a tangible way to explore complex anatomical features that otherwise remain hidden within the structure of wood.

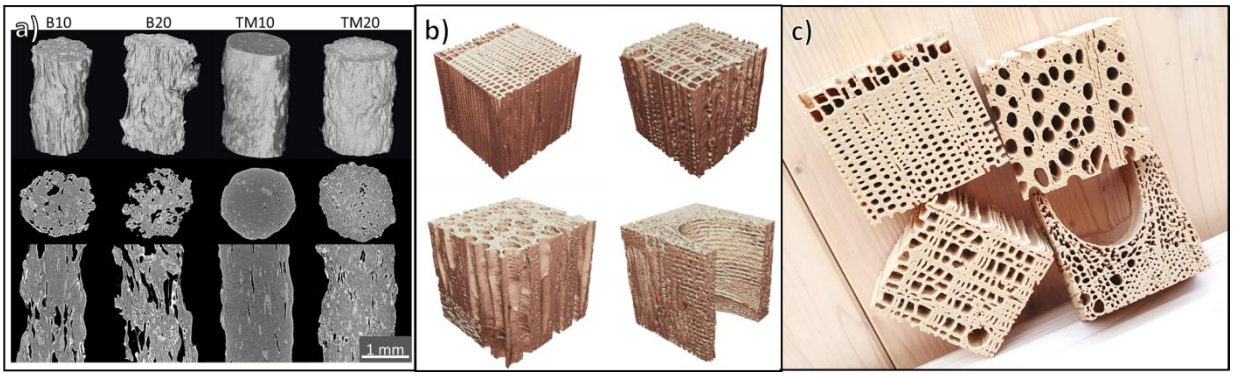

Figure 1: a) PLA fillaments containing 10% or 20% of beech wood particles (B10 and B20) or 10% or 20% of thermally modified beech wood particles (TM10 and TM20); b) digital 3D wood models, derived from µCT data; c)1500 times magnified and 3D printed models of wood.

Acknowledgments The authors acknowledge the financial support of the Slovenian Research and Innovation Agency (ARIS) (P4-0015, P4-0430, P2-0273, J7-50226).

Structural basis of antibiotic tolerance in biofilms

Mojca Blaznik, Marko Volk, Barbara Kraigher, Alba Calonge-Sanz, Gema Barco-García, Urška Vajngerl, David Stopar & Iztok Dogša

University of Ljubljana, Biotechnical Faculty, Ljubljana, Slovenia

Contact email: iztok.dogsa@bf.uni-lj.si

Introduction: Biofilms are structured microbial communities with increased tolerance to antibiotics. While many studies focus on cellular biochemical mechanisms, the role of biofilm architecture as a physical determinant of antibiotic efficacy remains underexplored. We show that biofilm structural integrity plays a decisive role in antibiotic daptomycin efficacy and highlight how microscopy enables direct visualization of biofilm architecture, matrix organization, and structural disruption [1].

Methods: Biofilms of *Bacillus subtilis* (wild type and matrix-deficient strains lacking the exopolysaccharide EpsA-O and the extracellular protein TasA) were grown under controlled conditions. Confocal laser scanning microscopy (CLSM) was used for 3D structural characterization of intact biofilms (Fig. 1) before and after sonication, while DIC microscopy assessed aggregation in resulting suspensions. Extracellular matrix components were visualized by Indian ink negative staining. Microscopy was combined with daptomycin treatment of intact and disrupted biofilms to correlate structure with antibiotic efficacy and killing dynamics. Ongoing work includes fluorescent labeling of daptomycin with BODIPY-FL and planned FRAP measurements of antibiotic mobility.

Results: Microscopy revealed major architectural differences between wild-type and EPS-deficient biofilms: wild type formed dense, cohesive 3D structures, whereas mutants showed reduced integrity. Negative staining confirmed the presence and spatial organization of matrix components, including EpsA-O. After disruption, wild-type biofilms retained larger aggregates, while mutants dispersed into single cells. These structural differences strongly affected antibiotic response: intact biofilms were highly tolerant to daptomycin, whereas disruption markedly increased its efficacy and killing rate, demonstrating a central role of physical organization in treatment outcomes.

D**iscussion and Conclusions:** Biofilm architecture and matrix-dependent cohesion are key determinants of daptomycin tolerance. Microscopy enabled direct linking of structure, matrix composition, aggregation behavior, and antibiotic efficacy. These findings establish biofilm structure as a functional factor in antimicrobial susceptibility rather than a passive scaffold. Ongoing work with fluorescent daptomycin and FRAP will quantify how biofilm architecture influences antibiotic mobility, providing a direct link between structure and transport.

Acknowledgements: This work was supported by ARIS (J1-3021, P4-0116), including microscopy infrastructure at MRIC UL (I0-0022-0481-08), Biotechnical Faculty, University of Ljubljana, Slovenia.

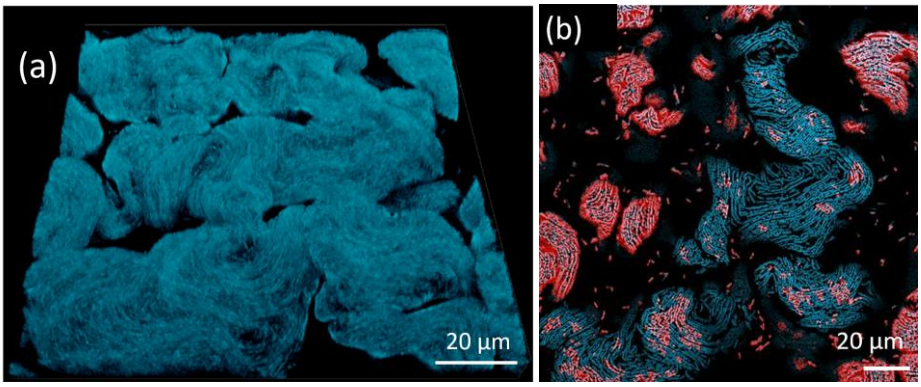

Figure 1: 3D-reconstructed CLSM maximum intensity projection of *B. subtilis* biofilm (a); Optical slice showing the effect of dapytomycin: red cells are dead (b), [1].

References:

1. M. Blaznik, M. Volk, B. Kraigher, A. Calonge-Sanz, G. Barco-García, D. Stopar, I. Dogša, *npj Biofilms Microbiomes* **2025**, 11, 232, https://doi.org/10.1038/s41522-025-00864-x

X-ray Microtomography as a Diagnostic Tool for the Restoration of Slavko Tihec's Kinetic *Aquamobile series*

Lidija Korat Bensa[a], Rožle Repič[a], Klara Retko[b,c], Simona Škorja[d]

[a] *Slovenian Building and Civil Engineering Institute, (Ljubljana), Slovenia*

[b] *IPCHS, Research Institute, (Ljubljana), Slovenia*

[c] *UL, Faculty of Chemistry and Chemical Technology, (Ljubljana), Slovenia*

[d] *Museum of Modern Art, (Ljubljana), Slovenia*

Contact email: lidija.korat@zag.si

Introduction: Slavko Tihec (1928–1993) is regarded as one of the most influential Slovenian sculptors of the 20th century, distinguished by his innovative use of industrial materials, modern technologies, and kinetic principles. One of the hallmarks of his oeuvre is the Aquamobile series – kinetic sculptures consisting of water-filled vessels with floating elements in constant motion. This study examines the sculpture *Vertikale*, held in the collection of the Museum of Modern Art in Ljubljana. The work comprises a complex hydraulic system, including a water basin with an electric pump and internal piping, a basin cover, and 21 buoyant components designed for random, continuous movement. The inherent nature of the work, which depends on continuous interaction between mechanical components and a liquid medium, has led to significant physical and chemical degradation. Prolonged exposure to water, mechanical wear from friction, and the natural ageing of synthetic materials have necessitated a comprehensive conservation treatment. This research analyses the specific degradation patterns observed on three floating components (P0, P1 and P2).

Methods: E-RIHS.si (Slovenian node of the European Research Infrastructure for Heritage Science) member institutions offer access to advanced methodologies and techniques specifically for cultural heritage applications. ZAG provides access to state-of-the-art, highly specialised equipment like Computed micro-tomography (µCT) system, enabling advanced analysis in heritage science. A notable feature of ZAG's micro-tomography (µCT) facility is its large scanning chamber, which allows high-resolution imaging of large objects that typically exceed the capacity of standard systems. Using these capabilities, the floating components of the installation were analysed. These polyester-based elements, oval with semicircular ends, are internally weighted and fitted with an approximately one-metre vertical rod. In the absence of original technical documentation or artists' blueprints, micro-tomography was crucial in characterising the internal composition of the base structures. The study also focused on identifying structural damage, such as cracks and weakened joints, and assessing degradation phenomena at the surface/water interface. This non-destructive, three-dimensional assessment provided essential insights into the long-term stability and preservation state and requirements of these kinetic components.

Results: Advanced computed micro-tomography, combined with extensive segmentation and 3D visualisation, revealed the intricate internal architecture of the sculpture's body and semicircular joints. Analysis of the three samples showed significant structural differences. The investigation identified a complex arrangement of compartments, adhesive layers, and textile reinforcements, and revealed manufacturing artefacts such as air bubbles within the polyester matrix or brush/finger traces from manufacturing. High-resolution imaging enabled precise mapping of structural vulnerabilities, including paint degradation, limescale deposits on the surface and stress cracks at critical connections.

Discussion and conclusions: These findings offer unprecedented insights into the artist's technological methods, suggesting an experimental or iterative approach to fabricating each element, and support a data-driven assessment of deterioration caused by continuous water exposure. Beyond its immediate diagnostic value, this research highlights the critical role of advanced imaging in preserving complex kinetic art, where internal structural data are often lacking. This study establishes a solid foundation for future assessment and the development of an optimal conservation strategy, ensuring

that material selection for the next conservation treatment is evidence-based and chemically compatible with the original polyester-based matrix.

Acknowledgments: This work was supported by the Slovenian Research and Innovation Agency and Slovenian node of the European Research Infrastructure for Heritage Science (I0-E012, P2-0273, I0-0032).

Implementation of serial SEM-based volume electron microscopy for use with urothelial tissue samples

Tim Zaveršek[a], Samo Hudoklin[a]

[a]*University of Ljubljana, Faculty of Medicine, Institute of Cell Biology, (Ljubljana), Slovenia*

Contact email: tim.zaversek@mf.uni-lj.si

Introduction. The urothelium is the epithelial tissue lining the urinary bladder that forms the blood-urine permeability barrier. This barrier depends on highly specialised apical cells that derive from underlying progenitors. Binucleate intermediate cells containing fusiform vesicles (FVs) are thought to serve this progenitor role, undergoing a differentiation process characterised by extensive organelle reorganisation [1]. The function of any cell is defined by the ultrastructure and spatial organisation of its organelles. Therefore, resolving the three-dimensional (3D) organisation of binucleate urothelial cells is key to understanding the process of umbrella cell formation.

Transmission electron microscopy (TEM) can visualise the ultrastructure of biological samples. However, the need for ultrathin sectioning limits TEM to essentially two-dimensional images, which can misrepresent the true shape of biological structures. Volume electron microscopy (vEM) is a fast-growing field that bridges the gap between 2D images and 3D structures by visualising biological structures in three dimensions [2]. Several vEM approaches are based on serial imaging of the sample with scanning electron microscopy (SEM): array tomography (AT), serial block-face SEM (SBF-SEM) and focused ion beam SEM (FIB-SEM). AT involves serial sectioning of samples with an ultramicrotome, mounting the section array on a flat conductive surface, such as a silicon wafer or a conductive glass coverslip, and imaging the sections with SEM. SBF-SEM uses an ultramicrotome to cut slices from the sample inside the SEM vacuum chamber, imaging the block-face rather than individual sections. FIB-SEM operates on a similar principle, except that a FIB is used to remove material instead.

Sample preparation for vEM methods demands some adaptations. Often, staining protocols that imbue samples with large amounts of heavy metals (megametal protocols) are used, which have the dual effect of increasing image contrast while also increasing sample conductivity.

After acquiring the vEM image stack, the slices need to be aligned and elements of interest visualised in 3D. This is achieved by annotation (segmentation) of the biological structures of interest on each slice, yielding a 3D volume ready for visualisation.

We aim to implement a vEM workflow to generate and analyse AT and SBF-SEM data, including sample preparation, imaging, segmentation and the generation of 3D models of biological structures.

Methods. Urinary bladders of male and female 8–16-week-old BALB mice were excised and cut into ~2 mm^2 pieces, fixed with 4% formaldehyde and 2% glutaraldehyde in 0.1 M cacodylate buffer and stained according to a modified megametal protocol (Deerinck et al.) [3]. Briefly, samples were stained in 2% OsO_4 with 1.5% potassium ferrocyanide in 0.1 M cacodylate buffer, followed by 1% thiocarbohydrazide, a second round of staining with 2% OsO_4, incubation in 1% uranyl acetate, and finally lead aspartate, pH 5.5. Thorough rinsing with distilled water was performed after each step. The samples were dehydrated with acetone, embedded in Durcupan (Sigma-Aldrich) and polymerised at 60 °C. For AT, glue (Pattex Universal Classic), diluted 1:3 in xylene, was applied to one side of the sample block before sectioning with an ultramicrotome (section thickness 70 nm). The sections were collected on gold sputtered (SCD 005 Sputter Coater, Bal-Tec) and APTES-covered coverslips and imaged with SEM (Quanta FEG 250) with no on-section contrasting. For SBF-SEM, we removed most of the excess resin before embedding (minimal resin embedding [4]) covered the sides of the trimmed sample with conductive silver epoxy resin (EM-Tec), then imaged and sectioned with SBF-SEM (Quanta FEG 250, Gatan 3View). Acquired images were aligned with the Linear Stack Alignment with SIFT plugin [5] in FIJI [6], then segmented with Microscopy Image Browser [7] and visualised with Slicer3D [8].

Results. AT: Serial sectioning of the sample block resulted in ribbons collectively containing over 120 serial sections without disruption (Fig. 1a). As a standard diamond knife boat (Diatome) was used, we cut classical glass coverslips down to fit the boat width and installed a home-made drain system to control the water level during section pickup. The coverslips were sputtered with 4–6 nm of gold to increase conductivity. Best imaging results were obtained by detecting backscattered electrons in the

SEM running at 2 kV. (Fig. 1b). Although the contrast of biological membranes varied among the cells, it was overall sufficient quality to allow for unambiguous recognition of cells and organelles (e.g., nucleus, mitochondria, FVs, Golgi apparatus; Fig. 1b, c), and even sub-organelle structures (e.g., mitochondrial cristae; Fig. 1d). Sample charging was not a problem in AT. Samples fixed and embedded in the same way were also used for SBF-SEM, where charging artefacts were significant. Charging was further reduced by covering the sides of the sample with silver epoxy resin, as well as using it to attach the sample to the pin. It was necessary to align the micrographs prior to segmentation. Segmentation and 3D reconstruction revealed that some intermediate urothelial cells containing FVs in their cytoplasm (arrows in Fig. 1b) are binucleated (Fig. 1e).

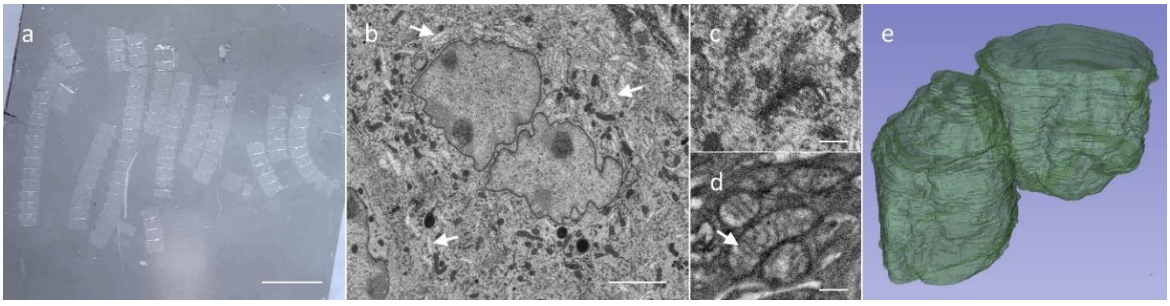

Figure 1: a) 121 serial sections collected on gold-covered coverslip for AT. b) SEM micrography of an intermediate urothelial cell with FVs (arrows) in cytoplasm. c) Closeup of Golgi apparatus and d) mitochondria with visible cristae (arrows) from the AT dataset. e) 3D reconstruction of nuclei.

Discussion and conclusions. We implemented an SBF-SEM and AT vEM sample preparation and imaging workflow, using urothelium tissue samples. SBF-SEM offers the advantage of automated data acquisition. AT, while also capable of automated imaging, can be performed without specialised equipment or dedicated software, at the cost of considerable time investment from a skilled operator. Sections for AT are mounted onto a flat, conductive surface. Indium tin oxide-coated coverslips are used traditionally, but represent a practical limitation due to their high cost. We demonstrate that gold sputtered coverslips are a viable alternative, introducing no noticeable charging or focussing issues, while preserving optical transparency and compatibility with correlative light and electron microscopy. Megametal staining ensures high sample conductivity and improves image contrast. The latter benefits both AT and SBF-SEM, while the former is particularly important for SBF-SEM, where charge accumulation in non-conductive embedding resin reduces image quality. Minimal resin embedding further reduced sample charging. Staining was variable within samples, reflecting inconsistent heavy metal infiltration across the dense tissue. Nevertheless, organelles and sub-organelle structures were reliably identifiable, demonstrating the protocol's suitability for subcellular morphological analysis.

Digital section alignment was more challenging for the AT dataset, where we had to not only account for translation, but also deformation and rotation of the sections. Manual segmentation is very time-consuming. There is therefore a strong incentive to automate this process using machine learning, but the biological and technical variability inherent to vEM datasets currently prevents any single universal solution. Some progress has been made toward automatic segmentation of urothelial vEM datasets [9]; however, a fully automated pipeline remains out of reach.

In conclusion, the recent installation of an SBF-SEM microscope at the Institute of Cell Biology and the establishment of a vEM workflow provides a foundation for future studies of the three-dimensional organisation of organelles in relation to cell and tissue function.

References:

1. Dalghi, M.G., et al., *Physiol Rev*, **2020**. *100*, 1621-1705.
2. Peddie, C.J., et al., *Nature Reviews Methods Primers*, **2022**. *2*, 51.
3. Konopova, B. and J. Tyc, *Front Zool*, **2023**. 20 p. 29.
4. Deerinck TJ, Bushong EA, Thor A, Ellisman, *NCMIR*, **2010**. *16*, 1138-1139.
5. Lowe, D.G., *International Journal of Computer Vision*, **2004**. *60*, 91-110.
6. Schindelin, J., et al., *Nat Methods*, **2012**. *9*, 676-82.
7. Belevich, I., et al., *PLoS Biol*, **2016**. *14*, e1002340.
8. Kikinis R, et al., *Intraoperative Imaging Image-Guided Therapy*, **2014**. *3*, 277–289
9. Zerovnik Mekuc, M., et al., *Comput Methods Programs Biomed*, **2022**. *223*, 106959.

Advanced Transmission Electron Microscopy of Gold Nanoparticles: Methodological Approaches and Nanoscale Structural Analysis

Darja Feizpour
Institute of Metals and Technology, Lepi pot 11, 1000 Ljubljana, Slovenia
Contact email: darja.feizpour@imt.si

Gold nanoparticles (AuNPs) are widely studied functional nanomaterials whose properties are strongly governed by their nanoscale structure. Transmission electron microscopy (TEM) remains one of the most powerful techniques for their direct characterization, enabling simultaneous evaluation of morphology, crystallinity, and chemical composition with high spatial resolution.

This contribution focuses on advanced TEM-based investigation of AuNP systems, highlighting both analytical capabilities and methodological considerations essential for reliable nanoscale characterization. The study combines high-resolution TEM imaging, selected-area electron diffraction (SAED), and energy-dispersive X-ray spectroscopy (EDS) to assess particle size distribution, morphology, crystallographic structure, and compositional homogeneity.

Special emphasis is placed on the interpretation of TEM data, including identification of lattice fringes, crystallographic orientation, and structural defects, as well as analysis of particle aggregation and interparticle interfaces. The work further addresses critical experimental aspects such as sample preparation strategies, optimization of imaging conditions, and the influence of electron beam–matter interactions on nanoparticle stability and image contrast.

A key aspect of the study is the differentiation between intrinsic structural features and artefacts induced during TEM observation, which is particularly important for nanoscale systems sensitive to beam effects. The presented approach demonstrates how careful methodological design and data interpretation enhance the reliability of TEM analysis and support the establishment of robust structure–property correlations.

Overall, the work underlines the central role of advanced TEM techniques in the characterization and understanding of gold nanoparticle systems, providing a foundation for their controlled design and application in technologically relevant fields.

Keywords: transmission electron microscopy (TEM), gold nanoparticles (AuNPs), SAED, EDS, nanoscale analysis, electron beam effects

Presentation of the Centre for Advanced Optical Microscopies at J. Stefan Institute (cNOM) and its recent implementation of automated large field-of-view SIM+2.5D+QPI microscopy

Boštjan Kokot[a], Cody Tripp[a], David Kopitar[a], Luka Šalamun[a], Ervin Mustafić[a], Hana Kokot[a], Janez Štrancar[a,b], Iztok Urbančič[a]

[a]*J. Stefan Institute, Ljubljana, Slovenia*

[b]*Infinite LLC, Maribor, Slovenia*

Contact email: bostjan.kokot@ijs.si

Introduction

Due to the variability of biological samples, the repeatability and reliability of research in biophysics and biology relies on performing a large number of measurements, which in the case of microscopy means capturing and analysing a multitude of microscopic images. The need for fast, automated microscopy is therefore increasing. On the other hand, the complexity of biological samples necessitates the use of complementary advanced imaging approaches – preferably simultaneously – which increases the need for multi-modal optical setups.

Presentation of cNOM

The Centre for Advanced Optical Microscopies (cNOM, center za Napredne Optične Mikroskopije)[1] was established at the J. Stefan institute in 2022 with the aim of improving the accessibility of both "work-horse" and state-of-the-art optical microscopes that are suitable for measuring biological samples. The Centre joined the EuroBioImaging network in 2025 as part of the SiMBION hub.

cNOM currently combines 7 different fluorescence-based optical microscopes (some of which are shown on Figure 1), including wide-field (confocal) microscopes, several fully-automated high-throughput confocal/STED laser-scanning microscopes and advanced multi-modal microscopes. To give two examples of advanced multi-modal microscopes: a system that combines fluorescence microscopy with a micromanipulator, spectrometer and optical coherence tomography, and a system that combines automated confocal laser-scanning and super-resolution STED microscopy with fluorescence lifetime imaging, spectral imaging, two-photon microscopy, reflectance microscopy, and also enables intelligent microscopy with content-aware selection of (sub)regions of interest based on live analysis of measurements.

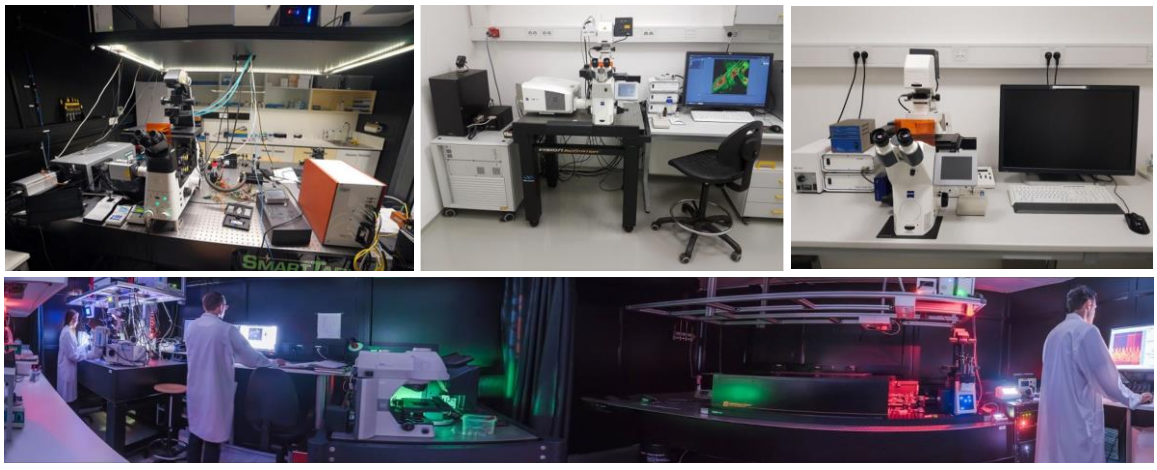

Figure 1: cNOM aims to improve the accessibility of "work-horse" and state-of-the-art optical microscopes, suitable for imaging biological samples

To increase the number of dyes that we can simultaneously image and distinguish, we are developing

a general spectral decomposition (cross-talk correction) algorithm. With three lasers and detectors, combined with gated detection, we plan to be able to record and reliably decompose 8-12 dyes of different cell organelles.

The microscopes in cNOM are positioned in laboratories that are registered for work on BSL1 samples (BSL2 in more than half of the laboratories) and most have a CO_2-, temperature- and humidity-stabilised environment for biological samples. Although they are especially appropriate for imaging living samples, they are often used on non-living systems as well. Most of the microscopes are automated and use an auto-focus to enable multi-day measurements, several of them being automated in-house using Python scripts.

Recent implementation of automated large field-of-view SIM+2.5D+QPI microscopy in cNOM

As the need for tracking of fast events and for quickly scanning large areas of the sample with good resolution grew, cNOM decided to build an automated large field-of-view fluorescence microscope with three complementary modalities (Figure 2 left). Structured Illumination Microscopy (SIM)[2] allows the user to capture a large field of view with excellent slicing and resolution at faster frame-rates (20 s for a 280 µm x 280 µm field of view at a resolution of 230 nm, Figure 2 right). For comparison: acquiring an equivalent image with a scanning confocal microscope takes 12 x longer (240 s). We have additionally equipped the microscope with projection imaging (2.5D microscopy)[3], which speeds up the capture of a projection image from a sample slice up to 13 µm thick by 10x (compared to acquiring images at multiple depths and max-projecting them in post-processing). We also added Quantitative Phase Imaging (QPI), which can be used to obtain the spatial distribution of the refractive index in a sample – even if the sample is not fluorescently labelled. The implementation of this microscope is in the final stages and the microscope is expected to be open for use in 2026.

Conclusion

The microscopes included in cNOM enable cutting-edge research in biophysics and biology due to their automation and unique combination of modalities, which enable gathering of large numbers of microscopy images to improve statistics and reliability of findings, as well as investigating the same living biological sample with several complementary optical microscopies. The vision of cNOM is to master and develop advanced optical microscopy techniques to facilitate wider use in interdisciplinary fields of research and applications.

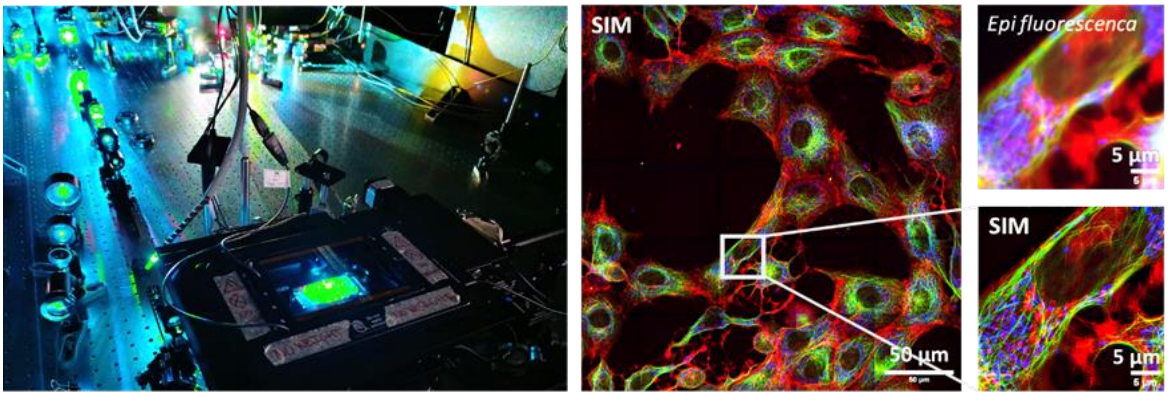

Figure 2: Left: Automated large field-of-view microscope, combining SIM, 2.5D and QPI microscopy. Right: Stitched panorama of living cells with a 280 µm field of view and 230 nm resolution, obtained in 20 s using SIM microscopy.

References:

[1] "Center for Advanced Optical Microscopies," can be found under https://cnom.ijs.si/, **2026**.
[2] A. Markwirth, M. Lachetta, V. Mönkemöller, R. Heintzmann, W. Hübner, T. Huser, M. Müller, *Nat. Commun.* **2019**, *10*, 4315.
[3] J. Ren, K. Y. Han, *Opt. Express* **2021**, *29*, 27530.

Robust quantification of multiplexed fluorescent proteins in plant tissues

Valentina Levak[1,2], Anže Županič[1], Karmen Pogačar[1,2], Nastja Marondini[1], Katja Stare[1], Tina Arnšek[1], Katja Fink[1], Kristina Gruden[1], Tjaša Lukan[1]

[1]National Institute of Biology, Slovenia; [2]Jožef Stefan International Postgraduate School, Slovenia

Genetically encoded biosensors are one of essential tools in biological research. They enable visualization of molecules of interest from the subcellular level to entire organism level *in vivo* and can be used to monitor presence of small molecules, gene expression, protein activity, and protein degradation spatiotemporally. However, multiplexing fluorescent biosensors in plants is notoriously difficult due to spectral overlap and strong autofluorescence from chlorophyll. In this study, we investigated the potential of multiplexing biosensors based on the selection of reporter fluorescent proteins. We characterized the emission spectra, fluorescence lifetimes, and relative brightness of diverse fluorescent proteins in plant leaves. We show that selected proteins exhibit comparable brightness, supporting their use in co-expression experiments and reliable quantification of individual signals. To separate overlapping signals, we applied two different linear unmixing approaches and compared them to results obtained without unmixing. We identified channel separation unmixing approach as the most suitable for biosensors. Additionally, we show how unmixing with the selected approach can be applied to separate autofluorescence and we validated this approach in virus-infected cells by following organelle dynamics *in vivo*. Overall, our work demonstrates that biosensors can be multiplexed, even when their emission spectra overlap.

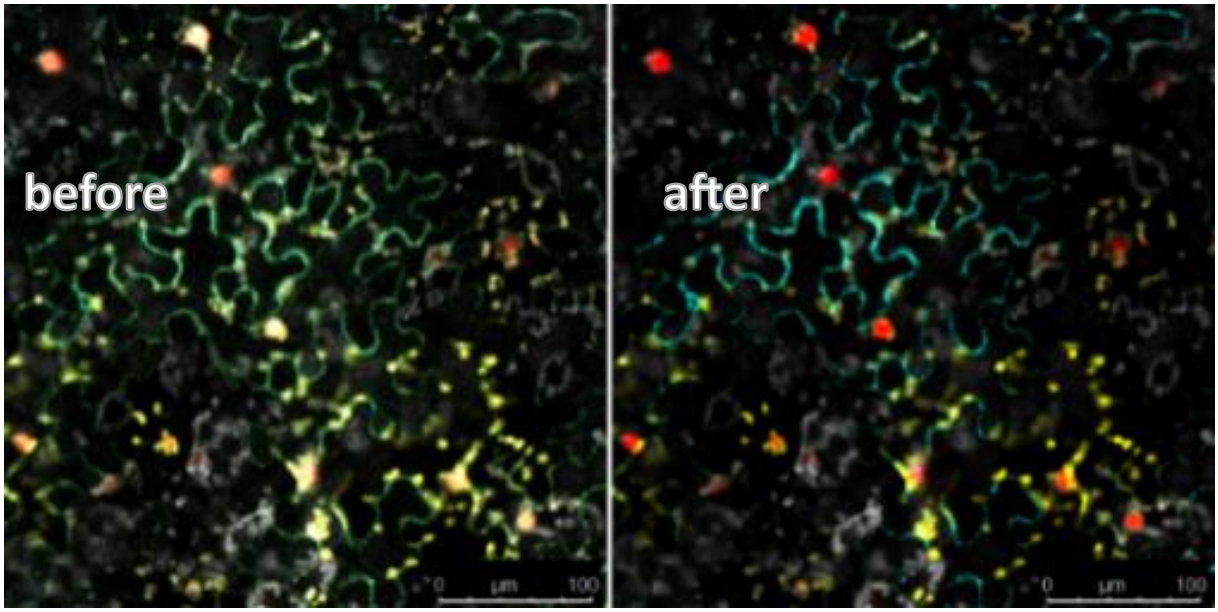

Focused Electron Beam-Induced Heating (FEBH) as a Tool for Local Modification of Materials

Shahzeb Ahmad[a], Matjaž Valant[a], Sandra Gardonio[a], Mattia Fanetti[a]

[a] *Materials Research Laboratory, University of Nova Gorica, Vipavska 13c, Ajdovščina 5270, Slovenia*

Contact email: mattia.fanetti@ung.si

Introduction: The increasing demand for flexible, high-resolution, and simplified nanofabrication techniques has driven the development of mask-less lithography approaches. Among them, mask-less and resist-less lithography techniques have the additional advantage of lower process complexity. Focused ion beam (FIB) processing can achieve high resolution (<10 nm), but it requires a FIB apparatus, it is limited to etching process and it may issue material damage or contamination [1, 2]. Direct Laser Writing (DLW) also offers mask-less patterning via localized laser-induced heating, but its resolution is generally limited to the micrometer scale [3].

In this work, we present a novel mask-less and resist-less nanofabrication approach, Focused Electron Beam induced Heating (FEBH), based on the local heating produced by an electron beam (e-beam) incident on a surface, which can be implemented within a conventional Scanning Electron Microscope (SEM). The purpose of this study is to demonstrate that localized e-beam heating can be used for controlled nanoscale material modifications, enabling precise patterning and local triggering of temperature-enabled phenomena. This approach aims to provide an additional versatile tool in nanofabrication workflows, with higher spatial resolution than DLW and accessible within standard SEM systems.

Methods: Thermal modification experiments, as well as characterization of samples before and after irradiation, were performed within a standard field-emission SEM (JEOL JSM-7100F TTLs). The experiments were conducted to investigate the effects of local e-beam heating on indium (In), vanadium pentoxide (V_2O_5), and bismuth selenide (Bi_2Se_3). Indium thin film of 40 nm thickness was deposited in vacuum onto a SiO_2 (200 nm)/Si substrate by e-beam sputtering system. V_2O_5 pellets were fabricated by hydraulically pressing of V_2O_5 powder. Bi_2Se_3 crystals with thickness of 30–40 μm were extracted by an ingot synthesized by Bridgman method. Thin flakes of Bi_2Se_3 with thickness ≤100 nm were mechanically exfoliated from the bulk crystal and scotch-tape transferred onto SiO_2 substrates. A coating of 10 nm of C was applied to avoid charging. In order to estimate the temperature rise at the surface of selected substrates, calculations were performed according to the Reimer's model for heat dissipation in SEM described in [4]. A focused e-beam was employed in spot mode to induce the localized heating in the selected materials. For the assisted focused e-beam heating (A-FEBH) experiments, a heating stage was mounted in the SEM, to increase the specimen base temperature during FEBH processing.

Results: When individual islands of In (approximately 200 nm wide and 40 nm thick) are irradiated with an e-beam under high-current conditions, localized heating causes them to melt, as shown in Fig. 1(a). The melted region remains confined to an area of a few hundred nanometers. Cathodoluminescence analysis of locally irradiated V_2O_5 indicated a reduction in the band gap, consistent with a thermally triggered semiconductor-to-metal transition. The calculated local temperature raising (according to Reimer's model [4]) is consistent with the transition temperature (260°C) reported in the literature [5]. As shown in Fig. 1(b), FEBH also induces nanoscale hole formation on the surface of Bi_2Se_3 crystal, but only above a threshold E≥15 keV. By introducing assisted-FEBH (A-FEBH), i.e. by rising the temperature of the whole specimen with a heating stage, hole formation is enabled even at low energies (5–10 keV) on the surface of Bi_2Se_3 crystal, confirming a thermally assisted mechanism. A-FEBH approach also enables controlled nanoscale patterning in thin flakes of Bi_2Se_3 (Fig. 1(c)), with enhanced localization at lower beam energies.

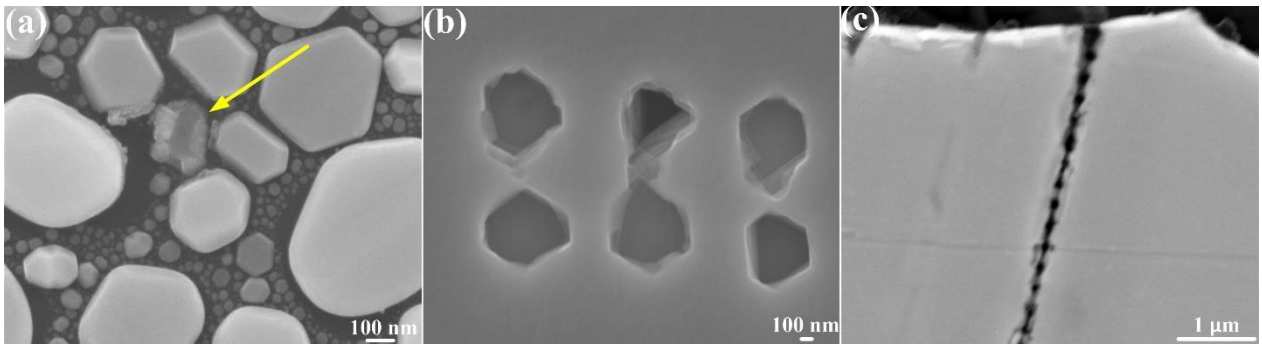

Figure 1: SEM images illustrating the FEBH effects on (a) an In particle (the irradiated particle is indicated by arrow), (b) surface of Bi_2Se_3 crystal, and (c) A-FEBH–induced patterning on a thin Bi_2Se_3 flake.

Discussion and conclusions: From these results we can conclude that, on suitable substrates, FEBH approach can easily generates localized high temperatures (>300 °C) within a standard SEM. FEBH approach can be used to achieve local modification, e.g. the etching of Bi_2Se_3 surface. Hole formation in Bi_2Se_3 occurs through a synergistic mechanism combining local e-beam induced Bi-Se bond breaking, and thermally activated Se sublimation. We also found that Reimer's model alone is insufficient to explain these modifications. To extend the achievable temperature range, the A-FEBH approach is also presented, which combines FEBH with in-situ substrate heating using a heating stage. In the case of Bi_2Se_3, A-FEBH enables controlled hole formation at lower E (5 keV) in bulk $Bi2Se_3$. We demonstrate that assisted heating is essential for patterning thin Bi_2Se_3 flakes, where optimized low-energy conditions (10 keV) allow ~100 nm features with minimal surrounding damage (Fig. 1(c)).
This work demonstrates a mask-less and resist-less nanofabrication method based on localized e-beam induced heating (FEBH/A-FEBH) in a standard SEM, enabling controlled nanoscale melting, phase transition, and patterning in materials such as Bi_2Se_3 without complex lithography approaches. This approach bridges the gap between high-resolution lithography techniques and simpler direct-writing methods, while remaining widely accessible. Future work will focus on improving thermal modeling, optimizing beam parameters for precise feature control, and extending the method to other functional materials.

References:

1. P. Basu, J. Verma, V. Abhinav, R.K. Ratnesh, Y.K. Singla, V. Kumar, Int. J. Mol. Sci. **2025**, 26, 3027.
2. K. Karimi, A. Fardoost, N. Mhatre, J. Rajan, D. Boisvert, M. Javanmard, Micromachines. **2024**, 15, 1274.
3. T. Pinheiro, M. Morais, S. Silvestre, E. Carlos, J. Coelho, H.V. Almeida, P. Barquinha, E. Fortunato, R. Martins, Adv. Mater. **2024**, 36, 2402014.
4. L. Reimer, Scanning electron microscopy: physics of image formation and microanalysis. 2nd ed. **1995**, Springer Series in Optical Sciences, vol.45, 57-134.
5. A.Pérez-Pacheco, D.Acosta-Najarro, R.Castañeda-Guzmán, H.Cruz-Manjarrez, L.Rodriguez-Fernandez, J.Pineda-Santamaría, M. Aguilar-Franco, J. Appl. Phys. **2013**, 113.

Tracking hot-deformation behavior of duplex steel with EBSD

Tina Sever, Franc Tehovnik, Irena Paulin

Institute of Metals and Technology, (Ljubljana), Slovenia

Contact email: tina.sever@imt.si

Lean duplex stainless steels feature a dual-phase microstructure, ideally in equal proportion of ferrite (body-centered cubic) and austenite (face-centered cubic crystal lattice). Their hot workability depends on the balance of phase softening processes during thermomechanical processing. Due to their excellent mechanical properties, weldability, and resistance to stress-corrosion cracking, these steels are utilized in the construction of storage tanks and piping for the chemical, oil and gas, and pulp and paper industries.

This study examines microstructural evolution in 1.4162 lean duplex steel deformed at 10 s^{-1} between 950 and 1300 °C to simulate industrial hot rolling.
Phase fractions were quantified by light microscopy (ASTM E562), while electron backscatter diffraction (EBSD) was used to analyze the influence of temperature on the softening processes: dynamic recovery (DRV), dynamic recrystallization (DRX), and grain growth.

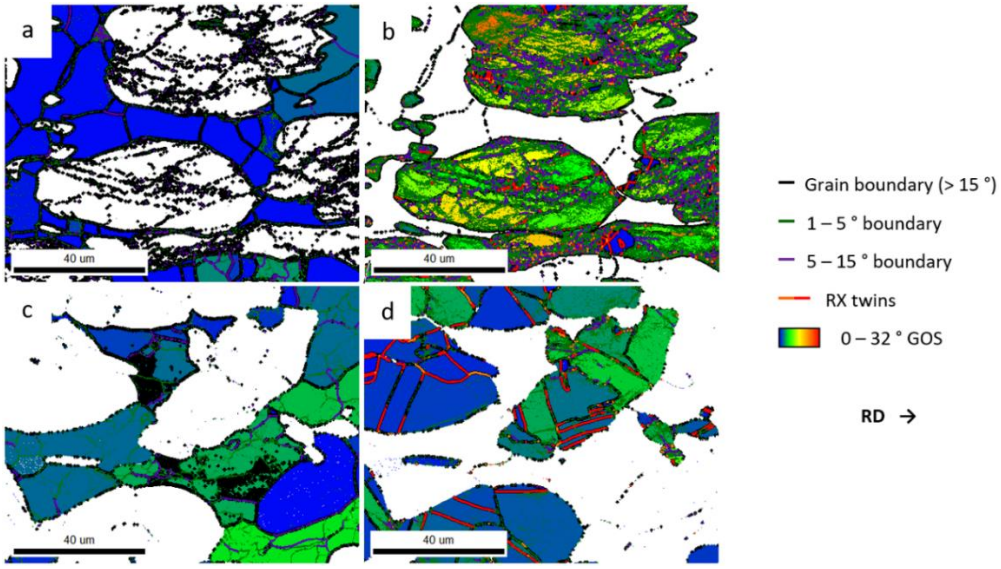

Figure 1: Boundaries and grain orientation spread (GOS) of ferrite (a) and austenite (b) at 950 °C, ferrite (c) and austenite (d) at 1150 °C.

At 950 °C, austenite hardens as it remains deformed due to insufficient temperature for DRX, while ferrite softens with DRV and DRX. This mismatch in the behavior of the phases causes localized strain that can lead to cracking. At 1150 °C, austenite undergoes DRX, releasing strain by decreasing dislocation density and forming twin boundaries. Ferrite continues to recover, forming subgrains, and recrystallize. Above 1150 °C, grains grow too coarse and the ferrite fraction increases (62:38), which leads to unfavorable decrease in strength of this steel.

EBSD proves effective for tracking phase-specific softening processes, supporting optimization of thermomechanical processing in lean duplex steels. Their properties can be further enhanced by microalloying.


SpeciOn
For science. For tomorrow.
Leica
MICROSYSTEMS
AUTHORIZED
PARTNER
HITACHI
www.specion.si

Predstavitve sponzorjev / *Sponsor presentations*

Zlati sponzor Thermo Fischer Scientific

Srebrni sponzor JEOL

Srebrni sponzor Zeiss

Srebrni sponzor Specion

From Atoms to Cells: Cryo-EM and Cryo-FIB Enabling In Situ Structural Biology

Radovan Spurny

Thermo Fisher Scientific, Czech Republic

Contact email: radovan.spurny@thermofisher.com

Abstract

Cryo-electron tomography (cryo-ET) enables three-dimensional visualization of macromolecular assemblies within their native cellular environment, providing structural information in situ that complements high-resolution approaches on purified specimens. By collecting tilt-series images from vitrified samples and reconstructing volumetric tomograms, cryo-ET reveals cellular architecture and molecular organization in a near-native state, and—when combined with subtomogram averaging—can deliver sub-nanometer detail for repetitive complexes.

A central requirement for cellular cryo-ET is the preparation of thin, electron-transparent specimens. Cryogenic focused ion beam (cryo-FIB) milling has become an enabling step for producing high-quality lamellae from cells and tissues, improving accessibility of intracellular regions and increasing the fraction of usable area for data collection. Correlative targeting approaches, contamination control, and lamella quality are key practical factors that strongly influence downstream acquisition and reconstruction.

Volume EM provides complementary 3D context at larger length scales by mapping cellular and tissue ultrastructure across micrometers to millimeters. Integrated with cryo-ET, volume EM supports multi-scale studies that link organelle- and cell-level architecture to molecular detail at targeted regions of interest.

Overall, cryo-ET—together with cryo-FIB sample preparation and complementary volume EM—provides a scalable route to connect molecular structures with cellular context, enabling mechanistic insights directly within intact cells and tissues.

The latest development in DualBeam technology for Materials Science

Min Wu

Thermo Fisher Scietific

This presentation will introduce the history of focused ion beam technology including ion source development from the early days and ion column design evolution at FEI company and Thermo Fisher Scientific.

It will also cover the overview of the latest advancement in both hardware and software perspective for FIB technology. The recent application development in focused plasma ion beam field will be shared including special usecases using Oxygen ion beam and Argon ion beam for various materials, and new opportunities for beam sensitive samples in Materials Science powered by dedicated cryo workflow and inert gas transfer solutions. It will also discuss the latest software innovation including newly developed automated cross section software and automated serial sectioning software Auto Slice & View 5 featuring unique spin mill technology, rocking mill technology and 3D TOF-SIMS capability. The benefits of using different primary ion beam such as Oxygen and Argon plasma beam for TOF SIMS data collection will be demonstrated as well.

Introducing the new ZEISS Crossbeam 750 with Gemini 4 column and ZEISS EMToolkit SW

Wolfgang Schwinger[1]
Manoj Mathew[2]

Corresponding Author: wolfgang.schwinger@zeiss.com
[1]Carl ZEISS GmbH, Laxenburgerstr. 2, 1100 Wien
[2]Carl Zeiss Microscopy GmbH, Kistlerhofstraße 75, Munich

For any advanced FIB/SEM application like sub 50 nm TEM lamella or atom-probe tip preparation, for milling beam sensitive samples, 3D tomography or precise site-specific preparation, the ability to mill and watch the ongoing milling-process unfold live with the electron beam is key.

With the all-new **Crossbeam 750** introducing the new **ZEISS Gemini 4** electron column fast, distortion free live observation is finally at your hand. The new high-dynamic-range (HDR) FIB-mill & SEM capability maintains a clear, high-resolution SEM view at any FIB condition, from rapid milling with high FIB currents down to fine polishing at 0.5 keV. This real-time clarity, paired with the Gemini 4 electron optics, allows to fine-tune processes as they work—reducing rework, improving yield and delivering highly uniform lamellae on the first pass.

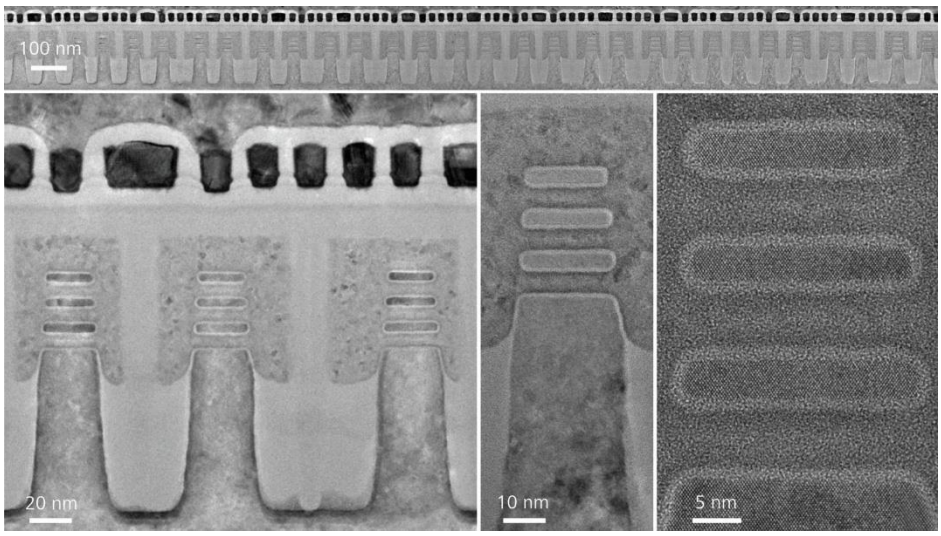

TEM image of 3nm GAA-FET SRAM prepared with Crossbeam 750

In the second part of this talk we will present ZEISS **EM toolkit**, a new and innovative software tool for easy automatization of imaging workflows on ZEISS electron microscopes by using the standard API interface. The user can built workflows using drag-and-drop building blocks, eliminating the need for time consuming coding (although parallel phyton scripting is available). Bulit in AI-based detection algorithms significantly enhance accuracy and repeatability compared to labour-intensive manual processes.

New auto-functions and customizable measurement capabilities ensure precise and reliable correlation between metrology data statistics and processing conditions. Logics and conditional loops allow for simple setup even of complex and demanding analytical workflows.

Silver Sponsor presentation: SPECION

Matej Novak

Specion, Slovenia

Contact email: matej.novak@specion.si

This lecture provides an introduction to sample preparation for electron microscopy and an overview of the main types of electron microscopes used in modern materials, life-science, and industrial analysis. The first part focuses on the key principles of preparing specimens for high-resolution imaging and microanalysis, including cleaning, fixation, dehydration, embedding, sectioning, coating and ion milling. Special attention is given to how preparation quality influences image contrast, resolution, charging, contamination, and the reliability of analytical results.

The second part presents a structured overview of the electron microscopy portfolio, including scanning electron microscopy and transmission electron microscopy. The lecture highlights the typical applications, advantages, limitations, and selection criteria for each instrument type. By connecting sample preparation strategies with microscope capabilities, the talk aims to help participants choose suitable workflows for specific research and quality-control tasks.

Sekcija posterjev / *Poster section*

Bor Arah	P-01
Ginevra Mango	P-02
Blež Belec	P-03
Janina Roknić	P-04
Sara Michelini	P-05
Alessandra Passarella	P-06
Tina Petrišič	P-07
Andreja Erman	P-08
Maja Deutsch	P-09
Tara Gudžulić	P-10
Špela Saje	P-11
Živa Pipan Tkalec	P-12
Anastasia Samodurova	P-13
Tanja Vajs	P-14
Saša Kos	P-15
Francisco Ruiz-Zepeda	P-16
Matej Hočevar	P-17
Rok Kostanjšek	P-18
Hristina Obradović	P-19
Lea Žibret	P-20
Polona Mrak	P-21
Aleksander Učakar	P-22
Marko Kolenc	P-23
Sorour Semsari Parapari	P-24
Ruggero Vigliaturo	P-25
Nina Križaj Kosi	P-26
Vedran Kojic	P-27
Jerica Pleško	P-28
Veno Kononenko	P-29
Polona Umek	P-30
Stjepan Dolić	P-31
Nina Daneu	P-32
Valentina Perc	P-33
Sergej Ražnjević	P-34
Tim Sotelšek	P-35
Sana Saeed	P-36
Elena Tchernychova	P-37
Tina Radošević	P-38
Matejka Podlogar	P-39
Matejka Podlogar	P-40

A Slice of Random Access Memory

Bor Arah[a], Anja Pajek[a],

[a]*CEMM, Institute "Jožef Stefan", 1000 Ljubljana, Slovenia*

Contact email: bor.arah@ijs.si

Introduction

The massive price increases of Random Access Memory (RAM) that started in October 2025 are caused by a global shortage of these complex electronics. While the shortage itself was caused by the spike in demand due to the massive worldwide datacenter investment, increasing supply to meet that demand in the short term is a difficult proposition due to the complexity of the end-product and the manufacturing hardware itself. To elucidate the impossibility of immediate supply expansion, we present here a tomography of a modern stick of RAM, serving as a direct visualization of the complexity of modern electronics. This complexity demonstrates why scaling manufacturing is not a simple matter of investment with immediate returns. Due to their intricate and varied internal structures, these electronics serve as an ideal case study to demonstrate how tomography can be utilized in materials research.

Methods

The sample was prepared by cutting the stick of RAM using an IsoMet 1000 diamond disc saw, followed by manual grinding using SiC grinding paper to remove the plastic mould and part of the Si die. The sample was then attached to a standard SEM Al pin via carbon tape and coated with ~10 nm of C to ensure conduction. Ion milling on the Thermo Fisher Scientific Helios 5UC Focused Ion Beam (FIB) was used for the area-of-interest preparation before proceeding with the tomography. Elemental mapping was conducted using an Oxford Instruments UltimMax EDS detector. Finally, ImageJ[1] was used to align the 2D SEM micrographs into a 3D stack, enabling a layer-by-layer volumetric reconstruction of the RAM's internal geometry.

Results

We have successfully prepared and analysed the sample, creating a 3D data stack. The sliced area has a width (x) of 142 µm and a depth (y) of 15 µm, with 10 µm (z) of the sample milled in approximately 200 slices, each 50 nm thick. This resulted in a final examined volume of 21,300 µm³. Electron images and EDS maps were recorded at an HV of 5 kV.

Discussion and conclusions

The project served to both explore the complexity of modern day electronics to elucidate the underlying reasons for the shortage, and to explore and demonstrate the capabilities of the recently acquired hardware and software at CEMM.

References:

1. Schindelin, J., Arganda-Carreras, I., Frise, E. et al., *Nat. Methods* **2012**.

Aberration corrected STEM-XEDS and Dual-EELS characterization of the Pb and magnetite interaction in a simulated biofluid

Ginevra Mango[1], Alessandra Passarella[1], Ruggero Vigliaturo[1]

[1]*Department of Earth Sciences, University of Torino, Torino, Italy*

Contact email: ginevra.mango@unito.it

Introduction

Lead is a relevant occupational contaminant in industrial settings. Inhaled or ingested Pb might reach the bloodstream, where elemental Pb and Pb nanoparticles (NPs) smaller than 200 nm can cross the blood-brain barrier, contributing to several diseases. In biological systems, excess metals may precipitate or accumulate, and in particular Pb strongly affects the central nervous system altering synapse formation and neuronal plasticity.

The brain environment contains phosphates, enabling Pb-phosphate precipitation. Moreover, the presence of both endogenous and exogenous magnetite (Fe_3O_4) NPs in the human brain might play a role in Pb complexation. Accordingly, magnetite surfaces offer reactive Fe-OH groups able to bind cations such as Pb^{2+}. The aim of this study is determining the physicochemical state of magnetite before and after the interaction with Pb in a simulated biofluid (SBF), measuring the Fe valence state at the particles surface and near-surface, and identifying any newly formed secondary Pb phase.

Materials and Methods

To mimic the conditions of the human brain, we used a SBF, specifically a phosphate-buffered saline (PBS) The reaction between Pb and magnetite was carried out at 39 °C for 48 h. The solid precipitate was recovered, rinsed, and analyzed. The samples before and after interaction were characterized using a multi-analytical approach combining Powder X-Ray Diffraction (PXRD), X-ray Photoelectron Spectroscopy (XPS), Scanning Electron Microscopy (SEM) coupled with X-Ray Energy-Dispersive Spectrometry (XEDS), and Aberration Corrected Scanning Transmission Electron Microscopy (acSTEM-XEDS) combined with Dual-range Electron Energy-Loss Spectroscopy (Dual-EELS).

Results

The more frequent morphologies of post-interaction magnetite are cubic, spherical, and ellipsoidal. Ellipsoidal morphology was not observed in the pre-interaction sample. STEM-XEDS and correlative Dual-EELS detected the presence of Pb on post-interaction magnetite surfaces, as well as the presence of a newly formed crystalline Pb-phosphate phase. The precipitation of a Pb-phosphate phase is compatible with the pyromorphite-group mineralogy. Moreover, the magnetite core crystal-state was unchanged after the interaction with SBF.

Discussion and future developments

These results suggest that magnetite NPs likely act as nucleation sites and has reactive substrates in vivo. Furthermore, Pb adsorption occurs via complexation with deprotonated surface hydroxyl groups ($\equiv Fe\text{-}O^-$).

Future work includes simulating soft tissues, verifying the model on human tissues, and performing 4D-STEM analyses, since the understanding of Pb speciation at oxide surfaces contributes to the mechanistic determination of its mobility and toxicity in a biological environment. Subsequently, it will be desirable to compare results from different experimental set-ups to foresee the evolution of related pathological processes.

Application of Scanning and Transmission Electron Microscopy in the Magnets Manufacturing Industry: A Case Study with Kolektor Mobility d.o.o.

Blaž Belec[a], Karla Kosmač[b], Boris Saje[b], Mattia Fanetti[a]

[a]*Materials Research Laboratory, University of Nova Gorica, Slovenia*

[b] *Kolektor Mobility d.o.o., Logatec, Slovenia*

Elektronski naslov: blaz.belec@ung.si

Collaboration between academia and industry is essential for translating advanced microscopy into practical insights for materials development. In this contribution we present a case study conducted within ALL-MICRO project (Interreg ITA-SLO program), a cross border network connecting research microscopy facilities with industry and public institutions[1]. ALL-MICRO promotes shared expertise and infrastructures among the partners, and enables companies and external users to access advanced characterization tools.

This contribution highlighting the collaboration between the Materials Research Laboratory and Kolektor Mobility d.o.o., and demonstrating how advanced electron microscopy can support industrial materials analysis. The objective of the study was to understand why NdFeB magnetic powder treated with a silane additive exhibits lower coercivity after compounding with a polymer. One possible explanation was that silane modifies the powder morphology.

NdFeB powders modified with silane were investigated using optical microscopy, SEM, and TEM combined with EDX spectroscopy. While optical and SEM observations suggested predominantly micrometre sized particles, TEM revealed that these particles are in fact hierarchical agglomerates composed of highly crystalline nanometre scale platelets. STEM EDXS analysis further showed that the silica-based coating is non uniform, with regions of incomplete surface coverage as well as significant amounts of free amorphous silica. However, no visible changes in the particle structure or morphology were observed after silica coating.

The study demonstrates how electron microscopy provides critical insight into powder morphology and coating efficiency, revealing the true nanoscale structure and size distribution of the powders. These nanoscale features, which can be observed only with advanced instrumentation, may significantly influence the magnetic properties of the final product, highlighting the importance of bridging academic characterization capabilities with industrial material development.

Acknowledgements: ALL-MICRO is financed by the Interreg VI-A Italy-Slovenia Programme.

REFERENCES:

1. *Official ALL-MICRO project website*: https://www.ita-slo.eu/en/all-micro.

Atomic-Scale Analysis of Ti Doping in Alkaline Niobate Ferroelectric

Roknić Janina[1, 2], Žiberna Katarina[1, 2], Bradeško Andraž[1], Drnovšek Aljaž[3], Koblar Maja[1], Kmet Brigita[1], Drnovšek Silvo[1], Malič Barbara[1, 2], Dražić Goran[4], Benčan Golob Andreja[1, 2]

[1]Electronic Ceramics Department, Jožef Stefan Institute, Ljubljana, Slovenia

[2]Jožef Stefan International Postgraduate School, Ljubljana, Slovenia

[3]Department of Thin Films and Surfaces, Jožef Stefan Institute, Ljubljana, Slovenia

[4]Department of Materials Chemistry, National Institute of Chemistry, Ljubljana, Slovenia

Contact email: janina.roknic@ijs.si

Ferroelectric potassium sodium niobate ($(K_{0.5}Na_{0.5})NbO_3$, KNN) has emerged as a lead-free alternative to conventional piezoelectrics, such as lead zirconate titanate, since its potential was first demonstrated by Saito et *al* [1]. While chemical modification is commonly used to tailor its functional properties, the atomic-scale mechanisms by which dopants influence the local structure remain insufficiently understood. Atomic-scale studies of acceptor-doped KNN, where lower-valence ions create charge-compensating defects such as oxygen vacancies[2], can reveal dopant effects on local polarization and lattice distortion. For example, Yan et *al*. used scanning transmission electron microscopy (STEM) to show that a gradient distribution of Cu^{2+} ions in KNN directly tailors the local domain structures and defect chemistry, enabling the coexistence of high polarizability and restricted domain-wall motion[3].

In this contribution, we investigate structural and compositional properties of undoped and Ti-doped KNN ceramics (with nominal compositions of 0.1, 0.2, 0.5, and 1.0 mol% Ti) using a combination of electron microscopy techniques and multislice image simulations.

At the macroscopic level, X-ray diffraction confirms that all compositions retain a pure perovskite phase with no detectable secondary phases. However, microstructural analysis by scanning electron microscopy reveals Ti-dependent secondary-phase formation, Nb-rich and Na-deficient regions, and increasing Ti segregation at grain boundaries with increasing dopant concentration. Ti doping also suppresses grain growth, leading to a bimodal grain-size distribution at intermediate concentrations (0.1–0.5 mol%), consistent with previous reports[4,5].

At the atomic level, HAADF-STEM image simulations were performed using the QSTEM multislice code[6] based on the orthorhombic KNN structure (ICSD #186310). Sample thicknesses of 4–20 nm were considered, with thermal diffuse scattering included via 30 frozen phonon configurations and random A-/B-site occupancies.

Simulations indicate that B-site displacements remain below the ~5 pm detection limit and are therefore unreliable for direct experimental interpretation. While simulated B-site intensities are slightly higher in undoped KNN due to Nb's higher atomic number relative to Ti, this contrast diminishes with increasing thickness. Experimentally, measured displacements are nearly an order of magnitude larger than simulated values, partly due to projection effects: in the $[100]_{pc}$ orientation, only eight of twelve possible orthorhombic displacement vectors are visible. No statistically significant difference in B-site intensity was observed between undoped and Ti-doped KNN, suggesting that sample thickness (30–70 nm) dominates over chemical contrast.

These findings highlight the critical influence of both sample thickness and projection geometry on the atomic-scale interpretation of KNN-based materials. They provide guidance for future studies aiming to correlate dopant distributions with local structure in this material.

[1] Y. Saito et *al*., "Lead-Free Piezoceramics," *Nat*., vol. 432, pp. 84-87, 2004.
[2] Z.-H. Zhao et *al*., "The formation and effect of defect dipoles in lead-free piezoelectric ceramics: A review," *SM&T*, vol. 17, pp. 1-11 (e00092), 2019.
[3] L. Yan et *al*., "Gradient-Acceptor-Doping Breaks the Piezoelectric Trade-Off in Lead-Free (K,Na)NbO3 Ceramics," *Adv. Mater.*, pp. 1-13 (e21306), 2025.
[4] X. Vendrell et *al*., "Improving the functional properties of $(K_{0.5}Na_{0.5})NbO_3$ piezoceramics by acceptor doping," *J. Eur. Ceram. Soc*., vol. 35, pp. 125-130, 2015.
[5] L.-Q. Cheng et *al*., "Fine-Grain Densification in Faceted Grain Ceramics via Chemical Modification," *Adv. Funct. Mater*., pp. 1-10 (e12006), 2025.
[6] C. Koch, PhD Thesis, Arizona State University, 2002.

This work is funded by the Slovenian Research and Innovation Agency (Young Researcher Project within P2-0105; J2-70101).

Bacteria–cell interactions in an advanced model of the gut epithelium

Sara Michelini [a], Marjan Bele [b], Damjana Drobne [a], Ines Mandič Mulec [c], Katarina Šimunović [c]

[a] *University of Ljubljana, Biotechnical faculty, Department of Biology, Ljubljana, Slovenia*

[b] *National Institute of Chemistry, Department of Materials Chemistry, Ljubljana, Slovenia*

[c] *University of Ljubljana, Biotechnical faculty, Department of Microbiology, Ljubljana, Slovenia*

Contact email: sara.michelini@bf.uni-lj.si

Introduction: Campylobacteriosis, primarily caused by *Campylobacter jejuni*, remains the leading bacterial cause of gastroenteritis in the EU and a major foodborne disease worldwide, most commonly associated with contaminated poultry. Infection typically presents as an acute gastrointestinal illness characterized by diarrhea (often bloody), abdominal pain, and fever, and may, in some cases, lead to severe post-infectious complications. Despite ongoing control efforts and the development of promising probiotic strategies, rising antibiotic resistance and variable intervention efficacy continue to limit the reduction of *Campylobacter* in the food chain and the mitigation of consumer risk. Therefore, the development of novel therapeutic and preventive approaches requires the investigation of host–pathogen interactions using advanced, physiologically relevant *in vitro* models that better recapitulate intestinal complexity and infection dynamics than conventional monocultures.
Methods: Thus, in this study, we examined the interaction of *C. jejuni* with three intestinal *in vitro* models of increasing complexity. These cultures are established on Transwell inserts, which, after long-term culture, allow the formation of a well-differentiated epithelial barrier that mimics key properties of the gut epithelium. The models included are Caco-2 monocultures, representing an epithelial barrier composed exclusively of enterocyte-like cells; Caco-2/HT29-MTX cocultures, representing a barrier composed of enterocyte-like and mucus-producing goblet-like cells; and Caco-2/HT29-MTX/Raji B triple cultures, representing a barrier composed of enterocyte-like, goblet-like, and M-like cells. In the latter model, Raji B cells are added to the basolateral compartment of the Transwell system during model preparation to induce the differentiation of a subset of Caco-2 cells into M-like cells, which possess antigen-sampling capacity and transcytotic activity. Once differentiation is complete, Raji B cells are removed, and the samples are ready for treatment. Collectively, these models reproduce key features of the human small intestine, including absorptive, mucus-secreting, and transcytotic functions. Following epithelial barrier formation, the models were exposed to *C. jejuni* for 16 hours. Host–pathogen interactions were then assessed by quantifying bacterial adhesion, invasion, and translocation across the different epithelial layers. Sample morphology was subsequently examined using scanning electron microscopy (SEM) (Thermo Fisher Apreo 2 S UHR/HR-SEM equipped with an Oxford Ultim Max 100 EDS system, 5 kV), following standard fixation with Karnovsky fixative, osmium impregnation, graded ethanol dehydration, HMDS drying, and gold/palladium coating.
Results: Our results demonstrate that *C. jejuni* interactions with the intestinal epithelium are strongly influenced by model complexity and cellular composition. In particular, the inclusion of mucus-producing goblet cells and M-like cells significantly altered bacterial adhesion and translocation patterns, highlighting their critical role in modulating infection dynamics. Morphological evaluation further revealed distinct interaction patterns across the three models. For instance, Caco-2 monocultures formed a well-differentiated epithelial monolayer characterized by dense microvilli, while infection induced the differentiation of some enterocytes into cells exhibiting an M-like phenotype and promoted the secretion of filamentous extracellular polymeric substances (EPS) by *C. jejuni*. Under these conditions, the bacteria appeared stressed, often failing to separate after replication and losing their characteristic spiral morphology. In Caco-2/HT29-MTX cocultures, HT29-MTX cells formed dome-like structures with vesiculated microvilli, surrounded by enterocytes. Mucus was likely lost during sample preparation and was therefore not visible. In infected samples, flakes of extracellular polymeric substances (EPS) were observed, but elongated (unseparated) *C. jejuni* were absent, although the bacteria had once again lost their characteristic spiral morphology. In the triple-

culture model, M-like cells were successfully generated, and HT29-MTX domes remained evident. As in the Caco-2 monoculture*, C. jejuni* produced filamentous EPS and displayed signs of stress (Figure 1A–B).

Discussion and conclusions: These findings underscore the influence of epithelial complexity on bacterial morphology, localization, and host interaction patterns, as well as the importance of using more physiologically relevant culture models to investigate bacteria–cell interactions.

Acknowledgments: This work was supported by ARIS project J4-4550.

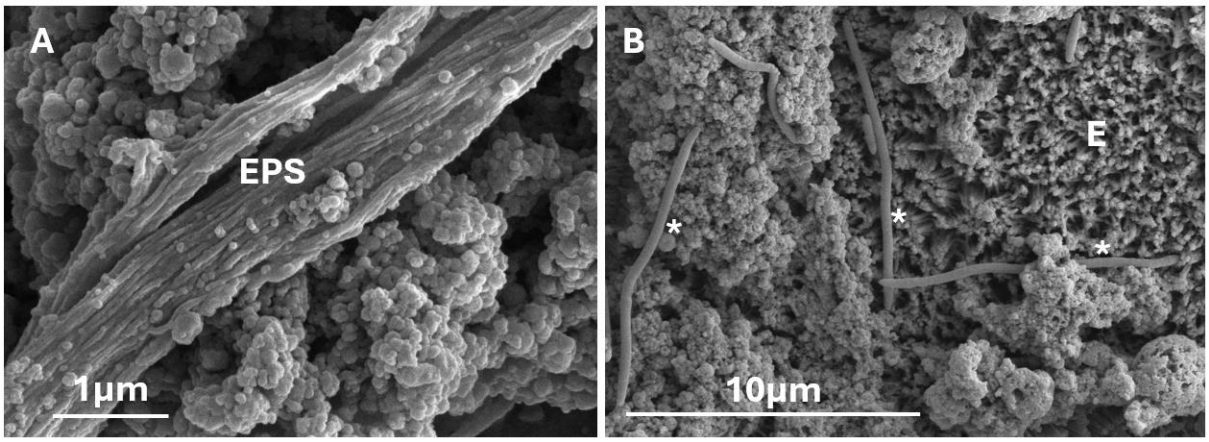

Figure 1. SEM image of a Caco-2/HT29-MTX/Raji B triple culture exposed to *C. jejuni* for 16 h. The bacteria produced EPS and appeared stressed (asterisks), exhibiting impaired separation after replication and a loss of their characteristic spiral morphology. E, enterocytes; EPS, extracellular polymeric substances.

Characterization of Al_2O_3 and MgO powders: morphometry and oxidation mechanisms

Alessandra Passarella[1], Ginevra Mango[1], Giulia Pia Servetto[1], Valérie Tschamber[2], Cornelius Schönnenbeck[2], Jean-François Brilhac[2], Ruggero Vigliaturo[1]

[1] *Department of Earth Sciences, University of Torino (Torino), Italy*

[2] *Laboratoire Gestion des Risques et Environnement (EA2334), Université de Haute-Alsace (Mulhouse), France*

Contact email: alessandra.passarella@unito.it

Introduction

Metal powders are promising carbon-free energy carriers. This is possible since energy can be stored by reducing metal oxides and later released through metal-air combustion. Understanding the physicochemical proprieties (including mineralogy and morphology) of the oxidation products is essential to optimize combustion efficiency and reduction cycle performance.

This study presents the characterization of Al_2O_3 and MgO powders produced under different experimental conditions, and combustors with the aim of identifying the oxidation mechanisms.

Methods

Al_2O_3 samples were collected from a Palas flame burner under three initial powders composition: excess Al setup (Palas 5.5), excess Al and water injection setup (Palas 5.5 + H_2O) and low Al setup (Palas 4). For each initial powders condition, two fractions were collected from the upper (TOP) and lower (BOTT) parts of the collection chamber. MgO samples were produced by oxidation of Mg powders of two size fractions (sample GM151: 50-70 µm and sample GM122: 70-100 µm) in a fixed bed reactor at 1°C/min up to 700°C in 5% O_2/He. All samples were characterized by Powder X-Ray Diffraction (PXRD), Scanning Electron Microscopy coupled with X-ray Energy-Dispersive Spectrometry (SEM-XEDS) and Transmission Electron Microscopy (TEM).

Results

PXRD analysis of all Al_2O_3 samples highlighted the presence of transition Al-containing phases, with TOP fractions systematically showing more thermically stable phases than BOTT fractions. Residual Al was detected in Palas 5.5 samples, consistent with incomplete oxidation due to an excess of Al availability. In Palas 4, where less Al was available, oxidation was more complete compared to Palas 5.5 samples, and no residual Al was detected in the TOP fraction.

SEM morphometric analysis of Al_2O_3 samples highlighted the presence of larger aggregates in BOTT fractions across all samples, while TEM dimensional analysis showed that particle size is identical in TOP and BOTT. TEM morphological analysis highlighted the presence of two particle populations in Al_2O_3 samples: spherical particles, from melting and solidification processes and polygonal particles, showing an anisotropic crystal growth. The polygonal fraction has a higher concentration in Palas 5.5 samples, compared to Palas 4 sample.

PXRD of the two samples of MgO highlighted only periclase in both samples, highlighting complete oxidation of the two samples with no intermediate phases. Sample GM122 displayed higher crystallinity degree than the sample GM151. SEM images of MgO samples highlighted micrometric aggregates (~100 µm) with surface covered with lamellar structures. TEM analysis of MgO samples highlighted the presence of different morphologies such as prismatic, rod-like, cubic, and rounded in both MgO samples.

Discussion and conclusions

The differences in polygonal fractions between Al_2O_3 samples are consistent with Al availability in each setup. An excess of Al in Palas 5.5 leads to incomplete oxidation and partial solid-state oxidation, while

less Al in Palas 4 leads to more complete oxidation. Polygonal particles were interpreted as the product of controlled solid-state oxidation, with the potential of preserving the original Al grain shape. In the MgO system, the gradual temperature ramp possibly favored solid-state oxidation, producing ordered structure, visible at SEM resolution.

Future work includes high resolution TEM investigation and Dual-range Electron Energy-Loss Spectroscopy (Dual-EELS) on particles of both systems to confirm the proposed mechanisms, and investigation of particle size and oxidation temperature effects, with the long-term goal of connecting oxidation conditions to energy carriers performance.

Comparative Analysis of Sample Preparation Techniques for SEM Imaging of Fixed Cells *In Vitro*

Tina Petrišič[a], Sara Michelini[a], Veno Kononenko[a], Marjan Bele[b], Blaž Tomc[b], Matej Hočevar[c], Damjana Drobne[a]

[a]*University of Ljubljana, Biotechnical faculty, Department of Biology (Ljubljana), Slovenia*
[b]*Chemical institute (Ljubljana), Slovenia*
[c]*Institute of Metal Materials and Technologies (Ljubljana), Slovenia*

Contact email: tina.petrisic@bf.uni-lj.si

Introduction: For high-resolution visualization of cell surface morphology by scanning electron microscopy (SEM), sample preparation is a critical step. In this study, we focused on the effects of post-fixation and conductive coating as potential sources of artifacts. We systematically evaluated the impact of different osmium tetroxide post-fixation protocols and gold–palladium (Au–Pd) coating thicknesses on the selected cell line.

Methods: Human alveolar basal epithelial cells derived from lung adenocarcinoma cells (A549) were cultured on glass coverslips for 24 hours to ensure adequate adhesion and spreading. Following primary chemical fixation in modified Karnovsky fixative (2.5% glutaraldehyde and 0.4% paraformaldehyde in sodium phosphate buffer) overnight at 4 °C, samples were subjected to one of three post-fixation conditions: no osmium treatment, single osmium tetroxide fixation (1 hour), and double osmium tetroxide fixation (2 × 1 hour). All samples were dehydrated through a graded ethanol series and subsequently dried using hexamethyldisilazane (HMDS). In addition, to assess the influence of conductive coating, samples were Au–Pd coated with varying thickness: no coating, 2 nm, 2 + 2 nm, and 2 + 2 + 8 nm. Images were acquired using the Everhart–Thornley Detector (ETD) and the in-column detectors T1 (SE), T2 (BSE), and T3 (mixed signal) integrated into the SEM column (Thermo Fisher Scientific Apreo). Different accelerating voltages were used to capture images (900 V and 15 kV). Imaging at identical locations was performed to enable a direct comparison of coating effects after each subsequent coating step.

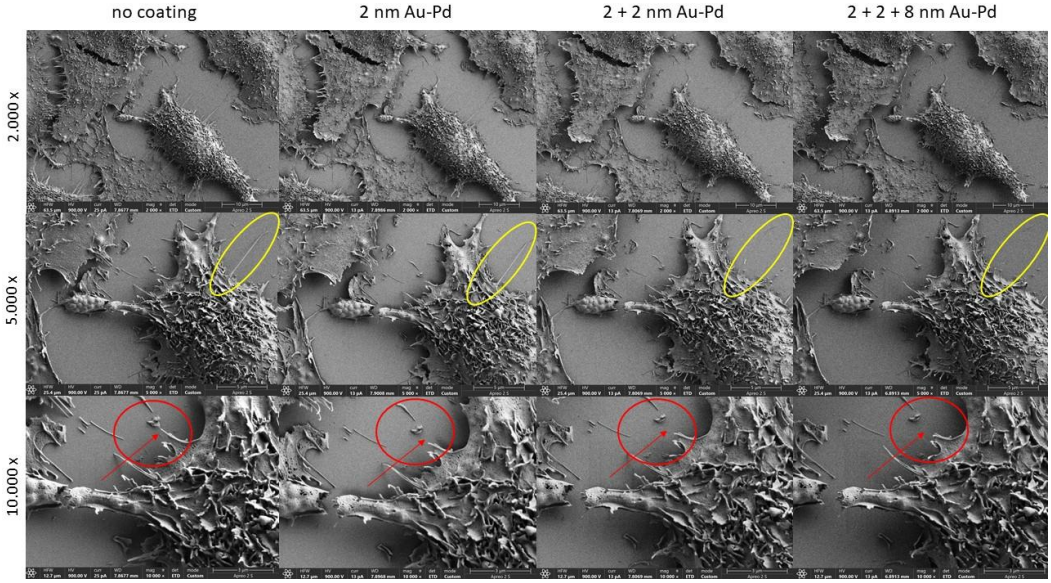

Figure 1: SEM images of samples with different conductive coatings but identical post-fixation (1 × 1 hour OsO_4). The yellow circle, red circle, and red arrow indicate cell protrusions that were clearly visible in the uncoated sample but were progressively damaged or lost at the identical location after subsequent coating steps.

Results: The results demonstrate that post-fixation with osmium tetroxide, whether applied once or twice, does not produce significant differences in overall image quality or preservation of cellular morphology. Across all tested magnifications (1.000× to 10.000×), cell surface structures remained consistently preserved regardless of osmium treatment. Minor differences, such as enhanced contrast in lipid-rich regions, were observed in osmium-treated samples, particularly under specific detector conditions, however, these did not substantially affect appearance of surface morphology.

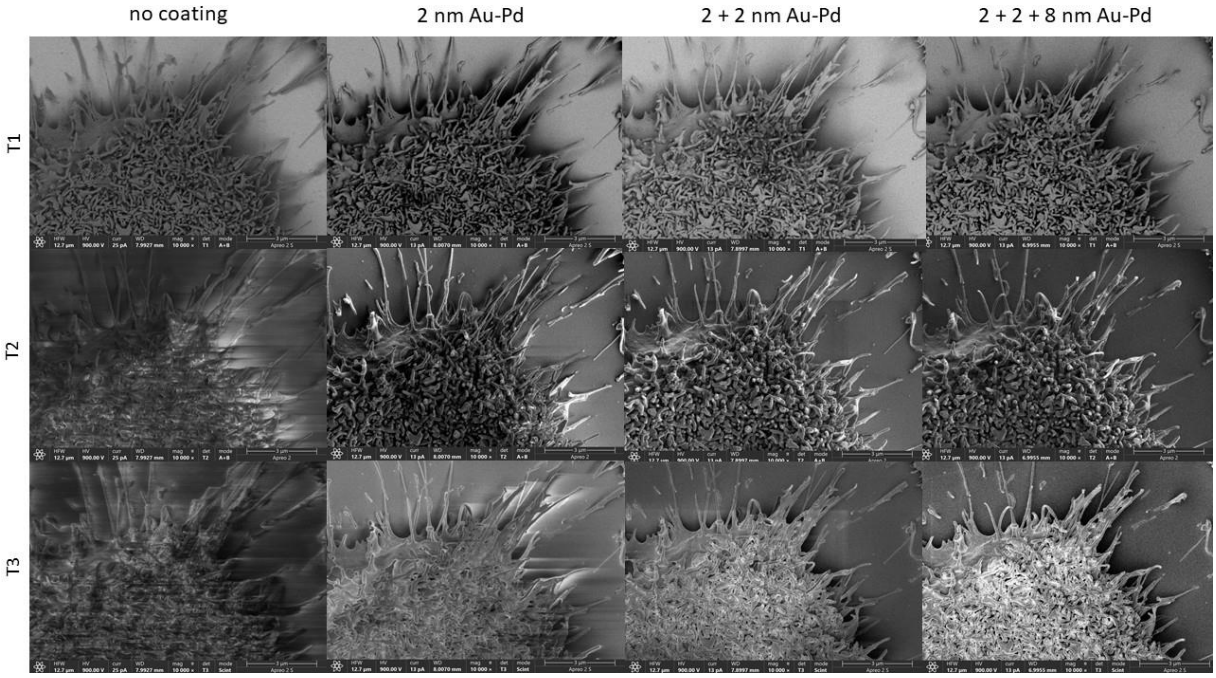

Figure 2: SEM images showing effect of coating on detector performance.

Next, the conductive coating thickness had a pronounced impact on imaging quality at higher accelerating voltages (15 kV). Uncoated samples exhibited strong charging effects, resulting in image distortion, reduced clarity, and signal instability. Application of a thin 2 nm Au–Pd layer partially reduced charging. Progressive coating (2 + 2 nm and 2 + 2 + 8 nm) significantly improved image stability, contrast, and resolution. At lower accelerating voltages (900 V), conductive coating thickness had no effect on imaging quality. However, the coating process significantly affected delicate cell protrusions which were gradually damaged and removed during each step of the coating procedure (transport, handling, coating) (Figure 1).
Detector performance was also influenced by coating thickness (Figure 2). T2 and T3 detectors showed substantial improvements in signal quality with thicker coating, enabling clearer visualization of fine surface structures. In contrast, ETD and T1 detectors provided acceptable imaging at lower coating levels but remained susceptible to charging in uncoated samples. These findings indicate a strong interaction between detector type and coating thickness, suggesting that optimal imaging requires consideration of both parameters.

Conclusions: This study demonstrates that conductive coating is a key determinant of SEM image quality in fixed A549 cells, outweighing the influence of osmium tetroxide post-fixation. Au–Pd coating effectively minimizes charging artifacts and significantly enhances image clarity and resolution, particularly when combined with advanced detectors such as T2 and T3.
In contrast, osmium tetroxide post-fixation does not substantially affect the preservation of cell morphology under the tested conditions.
These findings provide clear and practical guidance for SEM sample preparation, highlighting those efforts should prioritize coating optimization rather than modification of post-fixation protocols. Overall, the results support improved standardization of SEM methodologies and enable more reliable interpretation of cellular morphology *in vitro*.

Comprehensive microscopic analysis of urinary bladder telocytes

Andreja Erman[a], Manca Jernejc[a], Urška Dragin Jerman[a]

[a]*Institute of Cell Biology, Faculty of Medicine, University of Ljubljana, Slovenia*

Contact email: andreja.erman@mf.uni-lj.si

Introduction: Telocytes, elusive cells found in connective tissue, remain largely uncharacterised in many organs, including the urinary bladder. Despite increasing research on telocytes, some of their characteristics in the urinary bladder wall still require clarification. A well-described structural feature that distinguishes telocytes from fibroblasts is the presence of extremely long cytoplasmic extensions called telopodes. This unique feature continues to justify the use of transmission electron microscopy (TEM) as the gold standard for their identification even today. Another approach for differentiating telocytes from other interstitial cells is immunolabelling, which enables the detection of their specific molecular markers [1, 2, 3].

Methods and aim: Using immunofluorescent and immunogold labelling, along with various microscopy techniques ranging from light to electron microscopy, we aimed to examine the morphology, immunophenotype, cell junctions, localisation, and organisation of telocytes within the connective tissue of the lamina propria in mouse urinary bladders.

Results: Using conventional TEM, we confirmed the typical ultrastructural features of telocytes, including very long prolongations, an ovoid nucleus with a thin rim of surrounding cytoplasm rich in mitochondria, a considerable number of caveolae, fibronexus-type attachment plaques connecting to the extracellular matrix, and the absence of a basal lamina. In addition, we observed numerous budding and shed extracellular vesicles, including large multivesicular cargo aggregates previously reported in rat cardiac telocytes [4]. Extensive immunolabelling revealed different immunophenotypes of telocytes and, consequently, diverse telocyte subpopulations localised in various regions of the lamina propria. Regarding their localisation and organisation within the lamina propria, fluorescence and confocal laser scanning microscopy demonstrated that telocytes are aligned parallel to the urothelium and interconnected into a belt lying beneath the fibroblasts in the lamina propria. Three-dimensional confocal analysis revealed that telocytes appear as flattened cells with ribbon-like telopodes. Although these extensions appear thin under TEM, confocal imaging showed their broader, flattened morphology aligned parallel to the urothelial surface, with their wider side facing the urothelium.

Discussion and conclusions: These data, collected by various approaches, provide a more comprehensive insight into the structural characteristics of urinary bladder telocytes, further helping to elucidate the functions of these neglected connective tissue cells. Moreover, the results obtained in this study serve as a basis for further analysis of telocytes and their roles in different urinary bladder pathologies, such as cystitis and cancer.

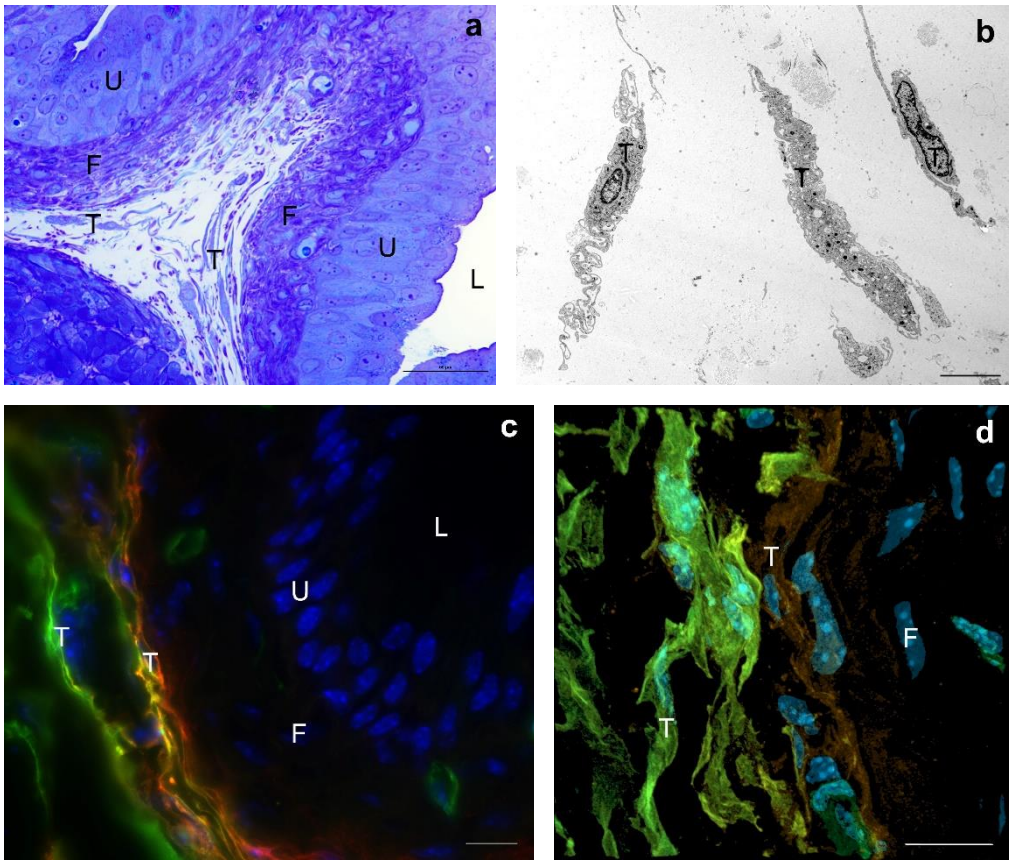

Figure 1: Telocytes of the mouse urinary bladder in a semi-thin section (toluidine blue staining) under a light microscope (a), in an ultrathin section under a transmission electron microscope (b), in a thin cryosection (5 µm) immunolabelled for CD34 (green fluorescence) and ENTPD2 (red fluorescence) under a fluorescence microscope (c), and in a thick cryosection (30 µm) immunolabelled for CD34 (green fluorescence) and ENTPD2 (red fluorescence) under a confocal microscope (d). In images c and d, cell nuclei are labelled with the fluorescent dye DAPI (blue fluorescence). T-telocyte; F-fibroblast; U-urothelium; L-lumen of the urinary bladder. Scale bars: 50 µm (a), 6 µm (b), 10 µm (c, d).

References:

1. Popescu LM, Faussone-Pellegrini MS. J Cell Mol Med. **2010**, 14(4), 729-40.
2. Gevaert T et al. J Urol. **2014**, 192(5), 1555-63.
3. Traini C et al. J Cell Mol Med. **2018**, 22(1), 195-206
4. Fertig ET, Gherghiceanu M, Popescu LM. J Cell Mol Med. **2014**, 18(10), 1938-43.

De novo design of nanobodies for immunohistochemical detection of Piezo1 mechanoreceptor in the urinary bladder

Maja Deutsch[a], Davor Babič[b], Rok Romih[a]

[a] *Institute of Cell Biology, Faculty of Medicine, University of Ljubljana, Slovenia*

[b] *Institute of Biochemistry and Molecular Genetics, Faculty of Medicine, University of Ljubljana, Slovenia*

Contact email: maja.deutsch@mf.uni-lj.si

Introduction

Immunohistochemistry (IHC) is a method for studying the localisation of proteins within tissues and cells using light and electron microscopy, relying on antibodies that bind to specific target proteins. In most IHC applications immunoglobulins G (IgGs) are used; these Y-shaped molecules have a molecular weight of approximately 150 kDa and consist of two heavy and two light chains. Their variable regions form the antigen-binding site, which recognises a specific epitope on the target protein. Antibodies can be monoclonal, recognising a single epitope, or polyclonal, recognising multiple epitopes on the same antigen [1]. Due to their relatively large size (13.7 × 8.4 nm), IgGs may have difficulty accessing epitopes that are sterically hidden or embedded within large protein complexes [2]. Single-domain antibodies (nanobodies) are therefore increasingly being explored as an alternative due to their significantly smaller size (~15 kDa) [3].

Piezo1 is a mechanosensitive ion channel that opens in response to plasma membrane stretching and mediates mechanotransduction in many tissues. This trimeric transmembrane channel consists of three identical protomers, each containing 38 transmembrane helices: two contribute to the central ion pore, while the remaining 36 are organised into nine transmembrane helical units (THUs) forming the blade. A beam on the cytoplasmic side of the plasma membrane connects the blade to the pore, and an extracellular cap domain regulates channel gating [4].

Piezo1 likely contributes to mechanotransduction in the urinary bladder, which undergoes stretching during micturition cycles. However, the localisation of Piezo1 in cells of different layers of the urinary bladder wall – i.e. urothelium (consisting of apical, intermediate, and basal cells), lamina propria (containing nerve endings and interstitial cells) and detrusor (smooth muscles) – is still not resolved.

The aim of our study was to compare IHC results obtained with different commercial antibodies against Piezo1 in the urinary bladder and then computationally design nanobodies that would detect Piezo1 in different IHC applications.

Methodology

To localise Piezo1 channels, mouse urinary bladders were prepared for immunofluorescence on frozen sections (IF-Fr). The bladders were fixed in 4 % formaldehyde, embedded in OCT medium and cut into 7 µm sections. Samples were immunolabelled with different primary antibodies against different epitopes on Piezo1 (Proteintech 15939-1-AP and 28511-1-AP, Novus Biologicals NBP2-75617) and secondary antibodies labelled with Alexa Fluor 555 or Alexa Fluor 647. Cell nuclei were stained with DAPI. Samples were imaged using a fluorescence microscope (AxioImager Z.1, Zeiss).

We employed a computational strategy to first assess epitope accessibility and then guide nanobody design. We generated candidate nanobody structures using the BoltzGen programme, which enables the design of potential binding domains based on the structural properties of the target protein. We generated a large library of candidate nanobody structures and filtered them according to predefined structural and binding criteria to identify the most promising candidates [5], which we subsequently evaluated using root mean square deviation (RMSD) analysis to assess the stability of the modelled nanobody–protein interactions.

Results

Piezo1 antibody 15939-1-AP (Fig. 1a) labelled the plasma membrane of all urothelial cells with a weak signal in the lamina propria and detrusor; 28511-1-AP (Fig. 1b) showed the strongest staining in

intermediate and basal cells, weaker in apical cells, and none in the lamina propria or detrusor; NBP2-75617 (Fig. 1c) labelled all urothelial cells as well as the lamina propria and detrusor.
Computational analysis of the 3D structure of Piezo1 and the relative size of the channel revealed that the epitopes recognised by the primary antibody 15939-1-AP are likely inaccessible, as they are buried within the cap domain formed by the trimeric assembly of Piezo protomers (Fig. 2a). This structural arrangement suggests that the size of conventional antibodies limits their access to these epitopes. Computational design yielded 64,000 potential nanobody candidates, which were filtered down to seven for further evaluation. These seven designed nanobodies showed stable three-dimensional structures with accessible binding sites on the Piezo1 channel (Fig. 2b). RMSD analysis confirmed structural consistency among the generated models, indicating their suitability for potential further development and experimental validation (Fig. 2c).

Discussion and conclusions

The results highlight the limitations of conventional antibodies in detecting large membrane protein complexes, such as the Piezo1 channel. Divergent staining patterns observed with different antibodies targeting the same protein complicate the interpretation of protein localisation and its role in normal urothelial function and urinary tract diseases. These findings emphasise the importance of developing complementary detection strategies for structurally complex proteins. Nanobodies represent a promising alternative due to their smaller size, which may facilitate access to sterically hindered epitopes. In this study, computationally designed nanobody candidates showed structurally stable binding models, supporting their potential for further development. However, these results represent an initial step, and experimental validation will be required to confirm the binding specificity and applicability of the designed nanobodies for immunohistochemical detection of Piezo1 mechanosensitive ion channels. More broadly, this approach may also open new possibilities for IHC detection of other structurally complex membrane proteins.

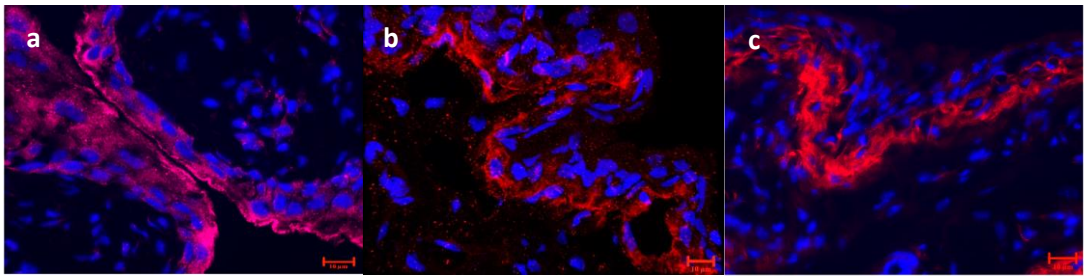

Figure 2: Immunofluorescence labelling of Piezo1 on frozen sections with antibody 15939-1-AP (a), 28511-1-AP (b) and NBP2-75617 (c).

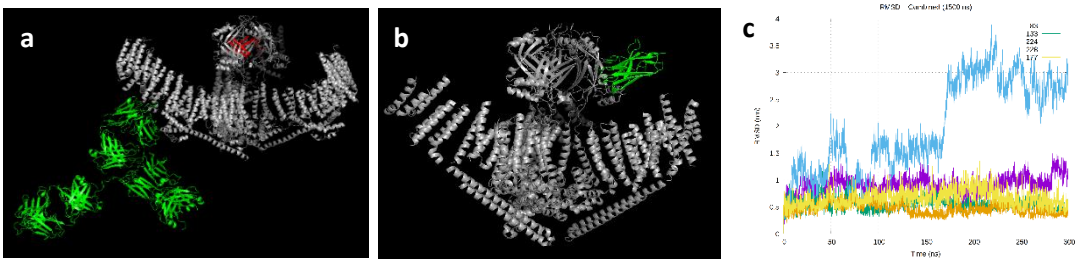

Figure 2: 3D model of (a) antibody or (b) nanobody (green) binding to Piezo 1 channel (grey). The epitope recognized by antibody 15939-1-AP is shown in red. (c) RMSD analysis of the modelled nanobody–Piezo1 complexes.

References

[1] G. V. Childs: *Elsevier* **2014**, 3775–3796.
[2] G. Griffiths, J. M. Lucocq, *Histochem Cell Biol* **2014**, 142, 347–360
[3] B. Jin, S. Odongo, M. Radwanska, S. Magez, *IJMS* **2023**, 24
[4] Y. Shan, X. Guo, M. Zhang, M. Chen, Y. Li, M. Zhang, D, *eLife* **2025**, 13
[5] H. Stark, F. Faltings, M. Choi, idr., BoltzGen: Toward Universal Binder Design. **november 24, 2025**.

Depth damage profiling in silicon substrates during focused ion beam chemical vapor deposition

Tara Gudžulić[1,2], Saša Kos[1], Gregor Kapun[2,3] and Miran Čeh[1,2]

[1]*Center for Electron Microscopy and Microanalysis, Jožef Stefan Institute, Ljubljana, Slovenia*

[2]*Jožef Stefan International Postgraduate School, Ljubljana, Slovenia*

[3]*National Institute of Chemistry, Department of Materials Chemistry, Ljubljana, Slovenia*

Corresponding author: tara.gudzulic@ijs.si

Focused Ion Beam (FIB)-assisted chemical vapor deposition (CVD) is widely used in materials science for site-specific milling, nanopatterning, and preparation of transmission electron microscopy (TEM) lamellae with nanometer precision. In dual-beam FIB-SEM instruments, both ion-beam induced deposition (IBID) and electron-beam induced deposition (EBID) can be used to deposit protective layers prior to lamella preparation. [1]

Although these processes are routinely employed, the high-energy interaction between the beam and the substrate can induce structural damage, which is a critical consideration in material characterization. This is particularly problematic for thin films, where surface-level defects or ion implantation can alter the entire material's functional properties. In contrast, such damage is often negligible for bulk materials where the affected volume is minimal relative to the whole. [2,3]

In this study, the influence of beam-assisted deposition conditions on substrate damage formation was systematically investigated on silicon wafer (110). Particular attention was given to the formation of amorphous layers, defect structures, ion implantation effects, and sputtering induced damage beneath the deposited layers. [4]

Depositions were performed using a Thermo Fisher Helios 5UC dual-beam system equipped with a Ga^+ ion source. Protective layers were deposited prior to lamella preparation using semi-automated procedure with Thermo Fisher AutoTEM 5 software. Top-down in-situ lift-out TEM lamellae (10 × 2 × 7 µm) were cutout and thinned to electron transparency. Lamellae were analyzed using a Thermo Fisher Talos F200X G2 operated at 200 kV.

Organometallic precursors, including naphthalene ($C_{10}H_8$), methylcyclopentadienyl(trimethyl)platinum ($CH_3C_5H_4$)Pt(CH_3)$_3$ and tungsten hexacarbonyl ($W(CO)_6$), were used to evaluate different surface damage profiles. [5] We prepared three types of sample protection depositions:

(i) EBID and IBID using W,
(ii) EBID and IBID using Pt,
(iii) simultaneous deposition consisting of W and C used for both EBID and IBID.

The results provide comparative insight into damage mechanisms associated with IBID and EBID deposition routes and establish guidelines for optimizing protective layer deposition during TEM sample preparation. The findings contribute toward predictive strategies for minimizing FIB-induced damage across different classes of materials.

Keywords: Focused Ion Beam, chemical vapor deposition, protective layers, EBID, IBID, AutoTEM 5.

Acknowledgement: Infrastructure Center for Electronic Microscopy and Microanalysis, Jožef Stefan Institute, Ljubljana, Slovenia.

References:

[1] B. W. Kempshalla, L. A. Giannuzzi, B. I. Prenitzer, F. A. Stevie, S. X. Da, *Comparative evaluation of protection coatings and focused ion beam chemical vapor deposition processes, American Vacuum Society.* **2002,** *20(1)*, 286–290.

[2] W. Y. Kwong, W. Y. Zhang, *Electron-Beam assisted platinum deposition as a protective layer for FIB and TEM applications, Conference: Semiconductor Manufacturing Excellence*, Munich, Germany, **2005**.

[3] A. Sabouri, C. J. Anthony, P. D. Prewett, J. Bowen, H. Butt, *Effects of current on early stages of focused ion beam nanomachining, Materials Research Express*. **2015**, *2(5)*, 1–8.

[4] B. C. Park, Y. C. Park, H. J. Lee, K. Kim, *Transmission electron microscopy study of damage layer formed through ion beam induced deposition of platinum on silicon substrate, Journal of Vacuum Science & Technology B, Nanotechnology and Microelectronics.* **2010**, *28(6),*31–37.

[5] J. Uzuhashi, T. Ohkubo, *Systematic study of FIB-induced damage for the high-quality TEM sample preparation, Ultramicroscopy*. **2024***, (262).*

Visualization of intracellularly degraded 2D material by FIB/SEM

Špela Saje[a], Francesco Tatti[b], Bashiru Ibrahim[c], Eugenia Valsami-Jones[c], Damjana Drobne[a]

[a]*Department of Biology, University of Ljubljana, Večna pot 111, SI-1000 Ljubljana, Slovenia*

[b] *Thermofisher Scientific – Div. Materials and Structural analysis, FEI Italia, Viale Bianca Maria 21, 20122 Milan, Italy*

[c] *School of Geography, Earth and Environmental Sciences, University of Birmingham, Edgbaston, B15 2TT, United Kingdom*

Contact email: spela.saje@bf.uni-lj.si

Introduction: Two-dimensional (2D) materials such as graphene oxide (GO) have attracted significant interest in biomedicine due to their unique structural and chemical properties. However, their intracellular fate, particularly their stability and degradation mechanisms, remains poorly understood. While biochemical assays suggest that GO can undergo enzymatic degradation, direct nanoscale visualization of these processes inside cells is still lacking [1–3]. In this work, we employ focused ion beam–scanning electron microscopy (FIB/SEM) to visualize graphene oxide (GO) and its structural state within cells. To assess its biological degradation, we complemented FIB/SEM imaging with spectroscopic and biochemical analyses.

Methods: A549 human lung adenocarcinoma cells were seeded on glass coverslips, allowed to adhere, and subsequently incubated with GO suspensions (30 µg/mL) for 24h to enable material internalization. Following incubation, samples were washed and chemically fixed in a modified Karnovsky fixative (2.5% glutaraldehyde and 0.4% paraformaldehyde in sodium phosphate buffer) overnight at 4 °C. Samples were then post-fixed twice using an osmium–thiocarbohydrazide–osmium (OTO) protocol. Dehydration was performed using a graded ethanol series and HMDS and left to air dry. Air dried samples were mounted on SEM holders and sputter-coated with gold/palladium for imaging with SEM. Imaging and FIB milling were performed using a Thermo Fisher Scientific SCIOS 2 FIB/SEM system. To evaluate enzymatic degradation, GO samples were incubated with human myeloperoxidase (hMPO) in the presence of NaCl and H_2O_2 [4]. Peroxidase activity was monitored over 24h to assess enzyme-mediated interaction and degradation of GO. Raman spectroscopy was performed to analyze structural changes, focused in variations in the D-to-G band intensity ratio used as an indicator of material structural modifications (formation of defects and oxidative damage to the GO lattice).

Results: FIB/SEM imaging confirmed the internalization of GO within cells, with cross-sectional views revealing its localization in intracellular compartments (Fig. 1b,c). High-magnification images revealed a crumpled morphology with a loss of sharp edges, while the layered structure of GO flakes remained visible within cells, indicating partial structural modification with some preserved features (Fig. 1c). In contrast, SEM imaging of GO outside cells showed well-defined, intact sheet-like structures with sharper edges and clear layering (Fig. 1a). Raman spectroscopy revealed a decrease in signal intensity after 24 h and slight increase in the D-to-G band intensity ratio after 24h, indicating structural modification and increased defect formation in GO (Fig. 1d, e).

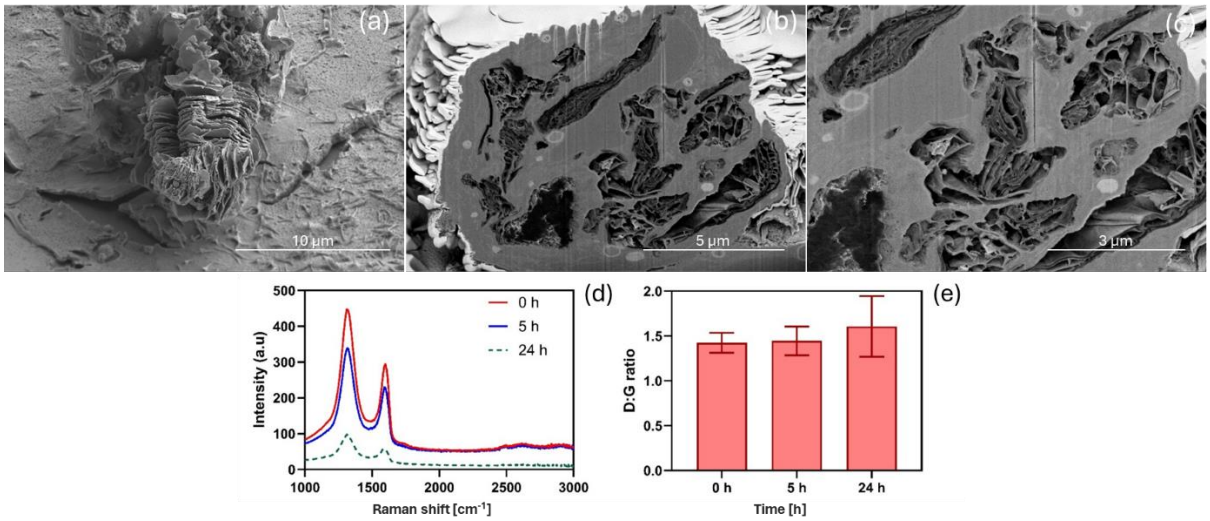

Figure 1. FIB/SEM micrographs and Raman spectra of graphene oxide (a) SEM image of extracellular GO flakes, showing typical sheet-like morphology. (b) FIB/SEM cross-section revealing GO within cellular compartments. (c) High-magnification FIB/SEM image highlighting the layered structure of GO inside the cell. (d) Raman spectra of GO before (0 h) and during (5h, 24 h) treatment. (e) Corresponding D-to-G band intensity ratios, indicating structural modification and defect formation. Scale bars are shown in the bottom right corner of each image.

Discussion and conclusions: Peroxidase assays demonstrated that GO undergoes only partial enzyme-mediated oxidative transformation, reflected by a slight increase in the D-to-G ratio. In contrast, GO within cells exhibited greater structural modification. This difference likely arises because the intracellular environment contains a complex mixture of enzymes and reactive species that can more extensively alter GO's structure than peroxidase alone. These results underscore the importance of combining imaging, spectroscopic, and biochemical approaches to fully assess the intracellular fate and biostability of 2D materials. In particular, direct visualization of GO within cells provides critical insight into the complex processes affecting its structure that cannot be captured by single-enzyme assays alone.

ACKNOWLEDGEMENT Study was supported by project ACCORDs that received funding from the European Union's Horizon Europe Framework Programme under grant agreement No 101092796. We thank also Slovenian Research and Innovation Agency (ARIS; J1-50014; J1-2482, P1-0184, P1-0153) and the Infrastructural Centre for Microscopy of Biological samples (MRIC UL, I0-0022-0481-08) at the Biotechnical faculty University of Ljubljana.

References:

1. D. Drobne, *Nanoimaging* **2013**, 950, 275-292.
2. T. Mesarič, L. Baweja, B. Drašler, D. Drobne, D. Makovec, P. Dušak, A. Dhawan, K. Sepčić, *Carbon* **2013**, 62, 222-232.
3. T.P. Dasari Shareena, D. McShan, A.K. Dasmahapatra, P.B. Tchounwou, *Nano-Micro Lett.* **2018**, 10, 53.
4. R. Kurapati, J. Russier, M. A. Squillaci, E. Treossi, C. Ménard-Moyon, A. E. Del Rio-Castillo, E. Vazquez, P. Samorì, V. Palermo, A. Bianco, *Small* **2015**, 11(32), 3985–3994.

Direct immunofluorescence and serology in autoimmune blistering disease

Živa Pipan Tkalec[a], Tara Golubić[a], Matic Bošnjak[a], Milanka Živanović[a]

[a] *MF, Inštitut za patologijo (Ljubljana) Slovenija*

Contact email: ziva.pipan-tkalec@mf.uni-lj.si

Introduction: Autoimmune blistering diseases are a rare heterogeneous group of disorders primarily mediated by autoantibodies, presenting with blister formation and/or erosions on the skin and/or mucous membranes (1). These diseases can broadly be classified into pemphigoid and pemphigus disease groups, as well as dermatitis herpetiformis (2).

Methods: The study included 83 patients with biopsy-proven autoimmune blistering diseases obtained from January 2025 to December 2025, all in whom serological testing was performed. Serological analysis included indirect immunofluorescence on normal human skin and salt-split skin, as well as enzyme-linked immunosorbent assay (ELISA) testing. Skin biopsies were examined by light microscopy and direct immunofluorescence using standard diagnostic protocols.

Results: Bullous pemphigoid was the most frequently encountered autoimmune blistering disease. Direct immunofluorescence of skin biopsies of 53 patients showed linear IgG and C3 deposits along the epidermal basement membrane. Anti-BP180 and anti-BP230 pemphigoid antibodies were detected in the serum of 46 patients. Four patients were diagnosed with linear IgA dermatosis, with direct immunofluorescence showing linear IgA and C3 deposits along the epidermal/epithelial basement membrane. In two of these patients, linear deposits were also detected by indirect immunofluorescence. One patient was diagnosed with epidermolysis bullosa acquisita. In this case, direct immunofluorescence showed linear IgG and C3 deposits along the epidermal basement membrane, while no circulating antibodies were detected in serum. Skin biopsies of 11 patients with pemphigus showed granular deposits of IgG, IgA, and C3 in the intercellular spaces between cells of epidermis/epithelium. Anti-desmoglein 1 and anti-desmoglein 3 antibodies were detected in 9 patients with pemphigus disease. Fourteen patients with dermatitis herpetiformis were included; direct immunofluorescence of skin biopsies showed granular IgA deposits in the dermal papillae of 11 patients.

Conclusion: Our statistical data from 2025 demonstrated that bullous pemphigoid represented the majority of diagnosed autoimmune blistering diseases (63,9%). The study confirms that autoimmune blistering diseases are a heterogeneous group of diseases requiring a multi-modal diagnostic approach. Therefore, the combination of serological testing (ELISA tests and indirect immunofluorescence) and direct immunofluorescence of skin biopsies remains the gold standard for differentiating between these heterogeneous autoimmune blistering diseases. While serological tests (ELISA) provide high specificity for pemphigoid and pemphigus diseases, direct immunofluorescence remains essential for the definitive diagnosis of dermatitis herpetiformis, linear IgA bullous dermatosis and cases with negative serological studies such as epidermolysis bullosa acquisita.

1. NV. Beek, D. Zillikens, E. Schmidt, Dtsch Arztebl Int. 2021, 118, 413–20.
2. L. Sollfrank, V. Schönfelder, M. Sticherling, Front Immunol. 2023, 14, 1-11.

Effect of Austenitization on the Microstructure and Hardness of C35 Steel

Urban Černe, Anastasia Samodurova, Aleš Nagode

Department of Materials and Metallurgy, Faculty of Natural Science and Engineering, University of Ljubljana, Slovenia

Contact email: anastasia.samodurova@ntf.uni-lj.si

The control of microstructure through the heat treatment is a key factor in optimizing the mechanical properties of carbon steels. The aim of this study was to investigate the influence of austenitization temperature, holding time and cooling rate on the microstructure and hardness of C35 steel.

Specimens were subjected to austenitization at temperatures of 800 °C, 900 °C, 1000 °C and 1100 °C with holding times of 0.5 h, 4 h and 8 h. After austenitization samples were either quenched to obtain martensitic structures or normalized to produce ferrite–pearlite microstructures.

Microstructural evolution was performed using light microscopy and scanning electron microscopy (SEM). Grain size analysis included the evaluation of prior austenite grain size in quenched samples and ferrite grain size in normalized samples using standard metallographic methods. Hardness was measured using the Rockwell method (HRC) for quenched samples and the Vickers method (HV) for normalized samples.

The results show a strong dependence of microstructure on austenitization temperature and holding time. A pronounced increase in prior austenite grain size was observed at temperatures of 1000 °C and above, where abnormal grain growth occurred, particularly for longer holding times.

In normalized samples a bimodal grain size distribution was identified at 1000 °C. Furthermore, Widmanstätten ferrite was observed in samples treated at 1000 °C and 1100 °C, with its formation becoming more pronounced at longer holding times.

In quenched samples, predominantly martensitic structures were obtained, with prior austenite grain coarsening leading to larger martensitic packets. In some cases, the presence of Widmanstätten ferrite was also detected due to decarburization and, subsequently, lower hardenability.

Hardness measurements showed a decreasing trend with increasing austenitization temperature and holding time.

The study confirms that austenitization parameters play a critical role in controlling the microstructure and mechanical properties of C35 steel. High austenitization temperatures and prolonged holding times lead to grain coarsening, which reduces hardness and promotes the formation of undesirable microstructural features such as Widmanstätten ferrite.

Microscopy techniques, particularly SEM, proved essential for identifying microstructural features and understanding transformation mechanisms. The results are consistent with the modified Hall–Petch relationship, indicating that finer grain sizes are also associated with higher hardness.

These findings emphasize the importance of optimizing austenitization conditions to achieve desirable microstructural characteristics and mechanical performance of C35 steel. Future work may include more detailed quantitative image analysis and advanced microscopy techniques to further investigate grain boundary phenomena.

Effects of selected pesticides on mitochondrial ultrastructure in skeletal muscle cells of larvae of the antlion *Euroleon nostras* (Geoffroy in Fourcroy, 1785)

Vajs Tanja[a], Žnidaršič Nada[b], Klokočovnik Vesna[c], Lipovšek Saška[a]

[a]*Department of Cell Biology, Faculty of Medicine, University of Maribor (UM), Slovenia*

[b]*Department of Biology, Biotechnical Faculty, University of Ljubljana (UL), Slovenia*

[c]*Department of Biology, Faculty of Natural Sciences and Mathematics (UM), Slovenia*

Contact email: tanja.vajs1@um.si

The aim of this study was to determine the impact of two pesticides on the structure of skeletal striated muscles in *Euroleon nostras* larvae. We compared the effects of the classical (conventional) synthetic insecticide chlorantraniliprole, which specifically targets insects, with those of lime sulfur, a sulfur-based pesticide permitted in organic agriculture and mainly used as a fungicide and bactericide rather than as an insecticide, although it may also exhibit insecticidal activity through contact toxicity by damaging the insect cuticle. To achieve this, we analysed the structure and ultrastructure of skeletal striated muscles in *E. nostras* larvae using light microscopy and transmission electron microscopy (TEM). In this section, we examine mitochondrial morphology to evaluate the effects of the two pesticides on mitochondria in muscle tissue.

Fieldwork included the collection and identification of antlion larvae. Third-instar larvae were used in the experiment and were identified based on body size, particularly head capsule size.

The antlions were transferred to the laboratory, weighed, and assigned to experimental groups. Prior to pesticide exposure, all larvae were fed one uncontaminated ant on five selected days to ensure comparable physiological conditions. Two concentrations were used in the experiment: the higher dose corresponded to that used in practice, and the lower dose was half that concentration.

The larvae were divided into five groups: (1) a control group fed uncontaminated ants, (2) larvae fed ants contaminated with 0,009% insecticide, (3) larvae fed ants contaminated with 0,018% insecticide, (4) larvae fed ants contaminated with 0,6% fungicide/bactericide, and (5) larvae fed ants contaminated with 1,2% fungicide/bactericide.

Antlion larvae ingested pesticides by feeding on contaminated ants. The ants were immersed in the pesticide solution for 10 s following the prey-dipping methodology described by Paramasivam et al. (2017) [1] and Twardowski et al. (2021) [2].

Mitochondria in skeletal muscle cells were analysed in three individuals from each group after four feedings (day 14) and eight feedings (day 28). TEM micrographs were quantitatively analysed using the open-source software ImageJ. The "ROI Manager" tool was used for parameter analysis. The mitochondrial analysis included organelle cross-sectional area, the longest (major) and shortest (minor) axes of the ellipse fitted to each organelle, organelle cross-sectional elongation (aspect ratio), and organelle cross-sectional roundness. Roundness was calculated as $(4 \cdot \text{Area}) / (\pi \cdot \text{Major Axis}^2)$. In this formulation, a value of 1 represents a perfect circle, whereas values < 1 indicate deviation from a circular cross-section.

Both doses of chlorantraniliprole and lime sulfur caused changes in mitochondrial cross-sectional area and cross-sectional roundness compared with the control group, with more pronounced alterations observed at the higher dose. The magnitude of these changes also increased with longer exposure time to both pesticides, regardless of concentration. Student's t-test indicated that the observed differences were statistically significant ($p < 0,05$) in all treatment groups (Figure 1).

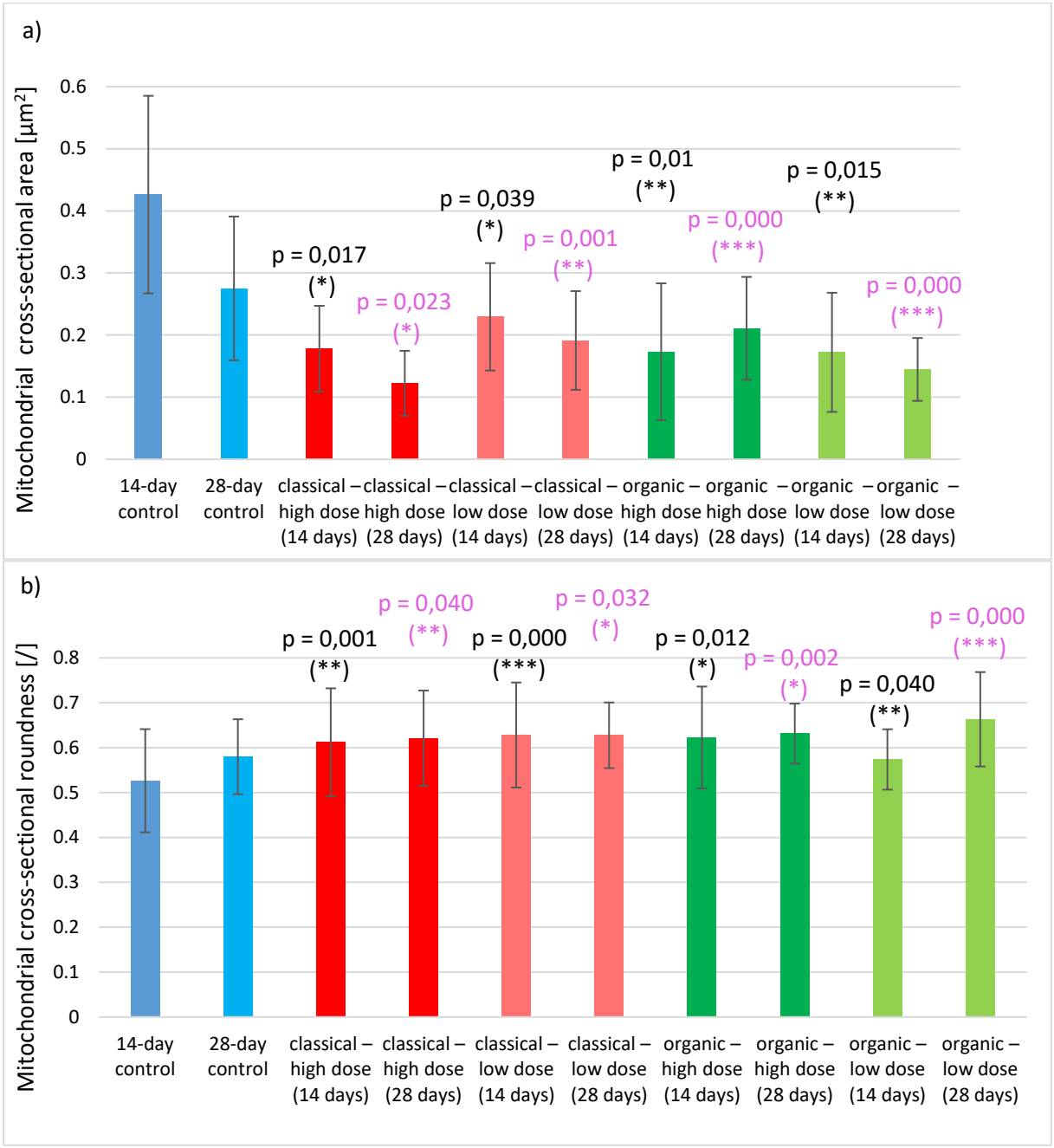

Figure 1: Mitochondrial cross-sectional area (a) and roundness (b) in the skeletal striated muscle of *Euroleon nostras* larvae after 14 and 28 days of feeding on contaminated ants. Bars represent mean ± standard deviation (SD). Statistical differences were determined using Student's t-test, comparing each treated group with the corresponding control group at the same exposure time (14 or 28 days). Measurements were obtained from 370 TEM micrographs, and a total of 7400 mitochondria were analysed. Asterisks indicate statistical significance (p *< 0,05, p** < 0,01, p*** < 0,001).

References:
1. M. Paramasivam & C. Selvi, Journal of Entomology and Zoology Studies, 2017, 5(3), 1441-1445.
2. J. P. Twardowski et al, (2021). *Insects*, 2021, 12(5), 434.

Experimental Challenges in *In Situ* Heating TEM

Saša Kos[a], Lara Einfalt[b], Miran Čeh[a,b,c]

[a]*Center for Electron Microscopy and Microanalysis, Jozef Stefan Institute, (Ljubljana), Slovenia*

[b]*Department for Nanostructured Materials, Jozef Stefan Institute, (Ljubljana), Slovenia*

[c]*International Postgraduate School, Jozef Stefan Institute, (Ljubljana), Slovenia*

Contact email: sasa.kos@ijs.si

In situ heating experiments in transmission electron microscopy (TEM) enable direct observation of thermally induced structural transformations at the nanoscale, providing valuable insight into phase transitions, crystallization processes, and microstructural evolution that cannot be captured using conventional ex situ characterization methods [1,2]. However, the reliability of in situ heating experiments is often influenced by methodological factors such as sample drift, grid stability, temperature gradients, and interactions between the specimen, support film, and heating holder components. These experimental variables can complicate the interpretation of observed structural changes and may introduce artifacts that are difficult to distinguish from intrinsic material behavior.

In this work, a methodological approach for in situ heating TEM experiments is presented using a JEOL JEM-2100 TEM equipped with a Gatan 652 double-tilt heating holder with a tantalum furnace capable of reaching temperatures up to 1000 °C. Special attention was given to the influence of commonly available and cost-effective TEM grid materials (Cu, Ni, and Au) with lacey carbon, which are widely used due to their accessibility and ease of preparation. Their thermal performance was evaluated during heating up to 800 °C, while investigating the thermal behavior of high-entropy oxide nanotubes and amorphous TiO_2 thin films. Experiments were performed using a controlled heating ramping with imaging and selected area electron diffraction (SAED) analysis at selected temperature intervals following thermal stabilization.

The experiments revealed significant differences in thermal performance of Au, Cu and Ni grids including grid deformation, carbon support failure, diffusion processes, and grid–holder interactions. Beyond the performance of the grid materials, another question arose during the experiments. Particles on the TEM grids exhibited heterogeneous structural transformations, which may reflect spatially uneven thermal conditions across the grid during heating, although intrinsic heterogeneity of the material cannot be excluded.

The results highlight the importance of grid selection for reliable in situ heating TEM experiments. While commonly used and cost-effective grids enable accessible experimentation, their thermal behavior can influence data interpretation. Future work will focus on experiments using other cost-effective and holder compatible grids and FIB-prepared lamellae to better isolate intrinsic material behavior from experimental artifacts.

References:
1. H. Saka, T. Kamino, S. Ara, K. Sasaki, *MRS Bull.* **2008**, 33(2), 93-100.
2. Z. Zhang, D. Su, *Ultramicroscopy* **2009**, 109(6), 766-774.

IL-STEM analysis of Pt-based nanostructures studied under relevant electrocatalytic degradation conditions

Francisco Ruiz-Zepeda[1,2], Lazar Bijelic[1], Ana Rebeka Kamšek[2], Ante Matošin[1], Carlos A. Campos-Roldán[3], Zhonghong Xia[4], Nejc Hodnik[1,2]

[1]*Department of Materials Chemistry, National Institute of Chemistry, Ljubljana 1000, Slovenia*

[2]*Institute of Metals and Technology, Ljubljana 1000, Slovenia*

[3]*ICGM, Univ. Montpellier, CNRS, ENSCM, 34095 Montpellier Cedex 5, France*

[4]*Institute for Sustainable Energy, Department of Chemistry, College of Sciences, Shanghai University, Shanghai 200444, P. R. China*

Contact email: Francisco.ruizzepeda@ki.si

This study examines how Pt-based nanostructures evolve at the microstructural level when exposed to various accelerated electrocatalytic degradation protocols that mimic both harsh and more realistic operating conditions [1]. Identical-location STEM was used to monitor structural changes that could directly affect catalytic performance and durability. The first group of materials included intermetallic Pt–M nanoparticles, where M represents Mn, Cr, V, or Zn [2]. The second part of the study investigated PtCoFeNi high-entropy alloy nanowires [3], analyzed under two different electrochemical degradation temperatures. The results are interpreted in terms of grain evolution, defect behavior, and overall chemical and morphological stability. For the nanoparticles, comparisons among the different intermetallic systems reveal how surface morphology and internal structure change following degradation. Additional phenomena of interest include particle mobility, the development of Pt-rich shells, and processes such as dissolution and redeposition. By linking the applied electrochemical stress conditions to the observed structural transformations, the study provides insight into the primary degradation mechanisms governing the stability of Pt-based nanostructures. Overall, the work aims to deepen understanding of how nanoscale structural changes impact electrocatalyst durability for a better design of a more robust Pt-based catalyst for future energy conversion technologies.

Acknowledgments: Authors would like to thank the European Research Council (ERC) Starting Grant 123STABLE (Grant agreement ID: 852208) and ARRS project J7-4637.

References:

1. Ante Matošin et al. J. Phys. Chem. C 2025, 129, 34, 15419–15432.
2. Carlos A. Campos-Roldán et al. ACS Catal. 2025, 15, 21, 17950–17957.
3. Zhonghong Xia et al. ACS Nano 2025, 19, 7, 7379–7390.

Laser-Induced Oxide Formation for Surface Functionalisation of Stainless Steel

Matej Hočevar[1], Barbara Šetina Batič[1], Peter Gregorčič[2]

[1]*Institute of Metals and Technology, 1000 Ljubljana, Slovenia*

[2]*Faculty of Mechanical Engineering, University of Ljubljana, 1000 Ljubljana, Slovenia*

E-mail: matej.hocevar@imt

Laser irradiation induces localised heating, which may lead to oxidation, melting, evaporation and ionization. These ablation effects depend on different processing parameters, such as pulse fluence, pulse duration, repetition rate, and scanning speed. When the fluence is below the threshold fluence for laser ablation, part of the laser energy is reflected and the rest is absorbed in the metallic surface. The absorbed optical energy results in localized heating, which leads to atom diffusion and - in oxygen-containing atmospheres (e.g., air) - to oxidation.

In this study, we use laser fluence that lead to metal surface oxidation and study the influence of different processing parameters on oxide thickness and its chemical composition. The relationship between pulse fluence, scanning conditions, and resulting oxide layer characteristics was analysed using microscopy-based techniques. Distinct colour variations were correlated with specific metal oxides.

The oxide layers exhibited nickel contents of 4–50 wt% and chromium contents of 2.5–21 wt%, with thicknesses ranging from ~100 nm to 500 nm (Figure 1), and morphologies varying from compact to porous.

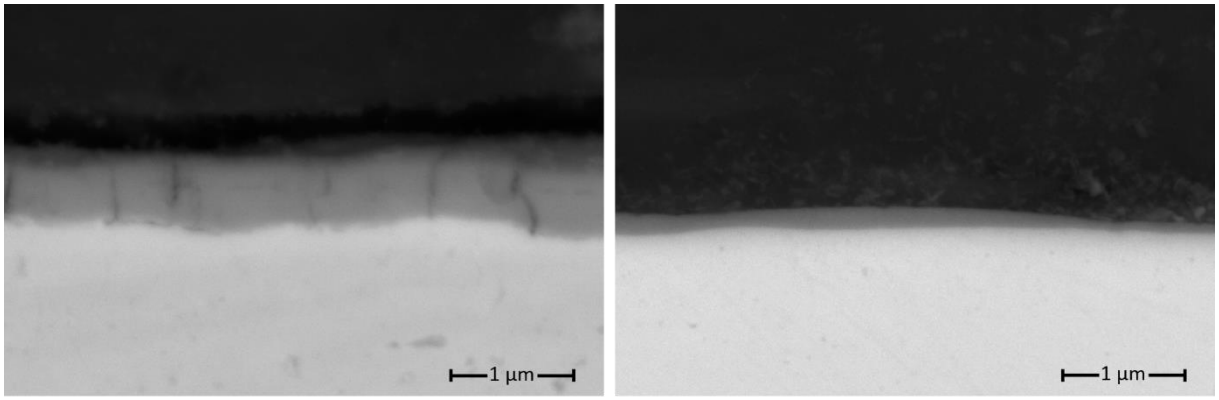

Figure 1: *SEM cross-section of oxide layers formed on 316L stainless steel under different laser processing parameters (left: thick, porous oxide with low chromium content; right: thin, uniform oxide layer with high chromium content).*

Acknowledgement:

The authors acknowledge the financial support from the Slovenian Research and Innovation Agency (research core fundings P2-0132, P2-0392, and project No. J2-60051).

microCT and FESEM analysis of parasitic acanthocephalans in proteus (*Proteus anguinus*), an endangered underground amphibian

Rok Kostanjšek, Grega Benko

Department of Biology, Biotechnical Faculty, University of Ljubljana, Ljubljana, Slovenia

Contact email: rok.kostanjsek@bf.uni-lj.si

Introduction: The olm or proteus (*Proteus anguinus*) is a highly endangered underground amphibian, threatened, among the others by parasites, including acanthocephalans. Acanthocephalans are worm-like endoparasites that require two hosts to successfully complete their life cycle. In their adult stage they attach to the intestinal wall of vertebrates (final hosts) and release their eggs into the intestinal lumen and subsequently into the environment. These eggs are then ingested by arthropods (intermediate hosts), which are later consumed by their final hosts, enabling the parasite to reach its reproductive site and complete its life cycle.

Acanthocephalus anguillae is a widespread freshwater parasite in Europe, typically cycling between fish and the crustacean *Asellus aquaticus*. Recently, however, this species has been detected in the digestive tract of the olm and in a population of exclusively cave-dwelling crustaceans [1]. This finding suggests the first documented case of a multiple-host parasite completing its life cycle in a subterranean environment.

Reproductive capacity in these parasites is generally confirmed by the presence of fully developed eggs in females attached to the gut wall of their final host. While mature eggs can be recognized by their elongated morphology, detailed analysis in our case was limited by the scarcity of biological material, namely rare adult female parasite specimens attached to the gut wall of the highly endangered amphibian host. To address this limitation, we applied a combined methodological approach: microCT scanning for initial screening and identification of egg-bearing females, followed by FESEM for high-resolution morphological analysis of the eggs.

Methods: Parasites were carefully removed from the intestinal wall of the olm and fixed in 4% formaldehyde in 0,1M phosphate buffer. After rinsing, specimens were gradually transferred to 70% ethanol and contrasted overnight with 0,3% phosphotungstic acid (PTA) in 70% ethanol. Specimens were then scanned using a Neoscan N80 (50 kV, 80 mA at 1.8 µm resolution, 0.2° rotation step and averaging of four scans). A total of 989 X-ray projections were used to reconstruct virtual cross-sections of entire parasites. Between 2665 and 3025 sections per specimen were processed for 3D reconstruction and segmentation using Dragonfly software (ORS Inc.). For FESEM analysis, samples were dehydrated through a graded ethanol series and transferred to HMDS, followed by air drying at room temperature [2]. Specimens were mounted on metal sample holders using carbon disks, carefully opened with dissecting needles to expose the body cavity, and sputter coated with 7 nm of platinum. Observations were performed using a JSM 7500F field emission scanning electron microscope.

Results: MicroCT analysis of PTA-contrasted specimens provided a non-destructive overview of internal anatomy. Female individuals were selected for FESEM analysis based on the presence of eggs in their body cavity. Subsequent FESEM examination revealed that most eggs were oval-shaped and immature, while a smaller proportion exhibited the elongated morphology characteristic of fully matured eggs.

Discussion and conclusions: The combined use of microCT and FESEM enabled efficient, non-destructive screening of parasites for the presence of eggs prior to detailed morphological analysis. Although this methodological combination is not commonly employed, it proved highly effective in the presented study and significantly reduced the number of required samples - an important consideration given the rarity of the host organism. Our findings confirm the ability of the olm to serve as the final host of *A. anguillae*, supporting the first documented case of a complete life cycle of a

multi-host parasite in a subterranean environment. These results also improve our knowledge on potential parasitic threats to this highly endangered cave animal in its natural environment.

Acknowledgements: The research was supported by ARIS funding to research program “Integrative zoology and speleobiology” (grant number P1-0184) and the infrastructural center “Microscopy of biological samples”, (MRIC UL, I0-0022-0481-08) at the University of Ljubljana, Biotechnical faculty.

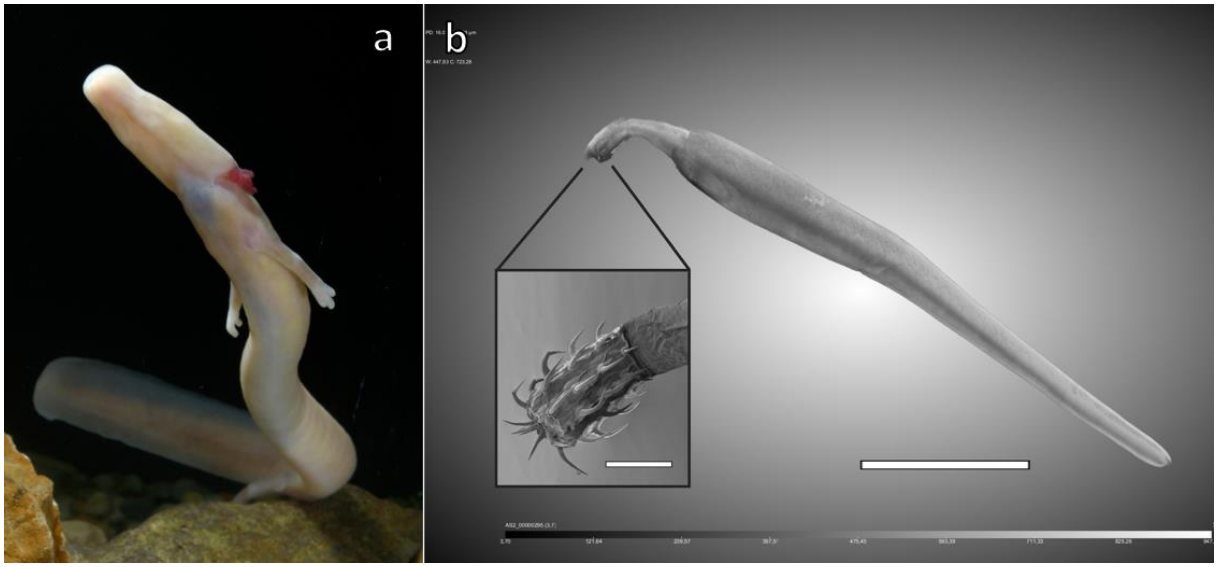

Figure 1: Olm or proteus (*Proteus anguinus*), an endangered cave salamander (bar=2 cm) (a) and microCT reconstruction of their parasite *Acanthocephalus anguillae* (bar=2 mm) with distinctive attachment hooks in its frontal part shown by FESEM (inset, bar = 100 µm).

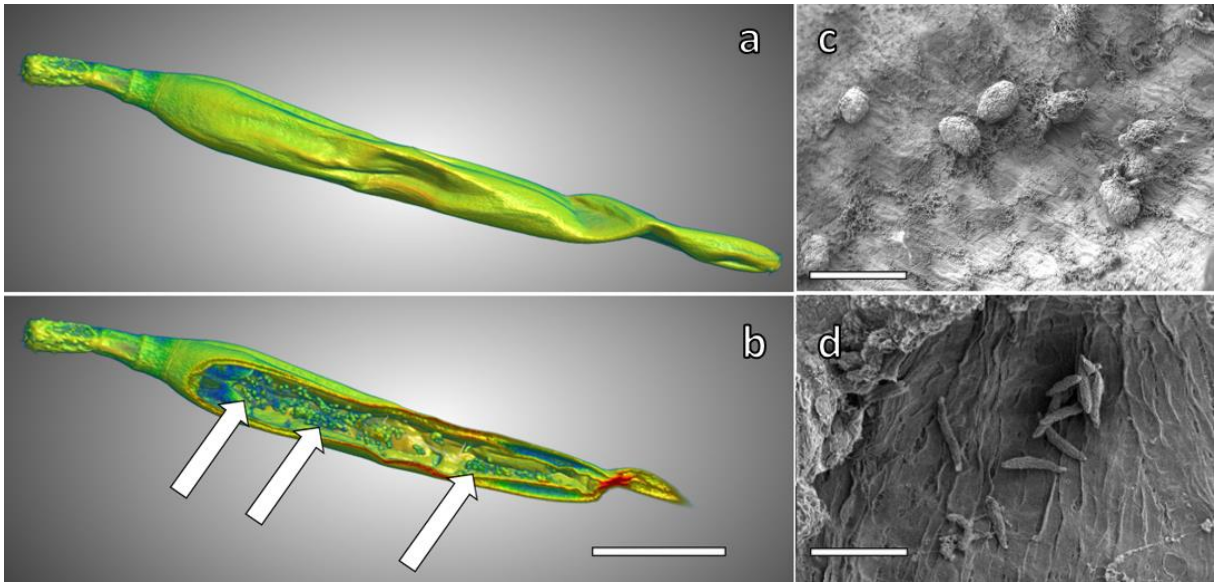

Figure 2. MicroCT visualization of the parasite’s external surface (a) and virtual cross-section (b) showing the eggs (arrows) within its body cavity (scale bar = 1 mm) and FESEM image of exposed eggs in the parasite body cavity, displaying rounded immature eggs (c) and elongated, fully mature eggs (d) (scale bars = 100 µm).

References:

1. Amin OM, Heckmann RA, Fišer Ž, Zakšek V, Herlyn H, Kostanjšek R. *Folia Parasitol*, **2019**, 66: 1-13.
2. Černoša A, Gostinčar C., Kostanjšek R, Lenassi M, Gunde-Cimerman N. *Sci rep,* **2025**, *15*, 1413.

Microscopic characterization of human amniotic membrane-based 3D-printed bioactive scaffolds for soft tissue regeneration

Hristina Obradović[1,2], Ivana Gazikalović[3], Aleksandar Janev[2], Jovana Jevdosić[1], Ivana Okić Đorđević[1], Dragana Aleksandrović[1], Slavko Mojsilović[1], Mateja Erdani Kreft[2], Aleksandra Jauković[1]

[1]*Group for Hematology and Stem Cells, Institute for Medical Research, National Institute of Republic of Serbia, University of Belgrade, Belgrade, Serbia*

[2] *Institute of Cell Biology, Faculty of Medicine, University of Ljubljana, Ljubljana, Slovenia*

[3] *Innovation Center, Faculty of Technology and Metallurgy, University of Belgrade, Belgrade, Serbia*

Contact e-mail: hristina.obradovic@imi.bg.ac.rs

Introduction: Human amniotic membrane (hAM) of the placenta represents a promising source of bioactive biomaterials for tissue engineering due to its rich composition of extracellular matrix (ECM) components and bioactive molecules with regenerative, anti-inflammatory, and immunomodulatory properties. Because the tissue is normally discarded after birth and exhibits low immunogenicity, it has been applied in skin, corneal and urogenital repair and has attracted increasing attention for the development of biomaterials aimed at soft tissue regeneration. Structural characterization of such biomaterials is essential for understanding the distribution of ECM components and the microarchitecture of engineered scaffolds that influence cell–material interactions. Development of scaffolds capable of supporting adipose tissue regeneration is particularly relevant for post-mastectomy breast reconstruction given that despite safety and feasibility for patients, existing breast reconstruction techniques post- mastectomy carry the risk of potential complications. In this study, we performed microscopic characterization of hAM-derived biomaterials and 3D-printed scaffolds.

Methods Placentas were obtained from healthy donors following cesarean sections, and the hAM was separated from the chorion and homogenized using a previously established protocol under patent protection [1,2]. Fluorescence microscopy was employed to visualize ECM proteins within the homogenate and confirm the presence of key structural components. Additional characterization included analysis of cytokine composition by flow cytometry and physicochemical properties relevant for scaffold fabrication. For scaffold fabrication, hydrogels were prepared by combining selected concentrations of hAM homogenate with alginate solutions of different viscosities and subsequently printed using an extrusion-based 3D bioprinter. The printed constructs were crosslinked with $CaCl_2$ to obtain stable scaffolds suitable for structural and cellular evaluation. Microscopic analysis was performed to assess both the material structure and its interaction with cells. Brightfield and phase-contrast microscopy was used to examine the morphology of the printed scaffolds and to evaluate the attachment of human adipose-derived stromal/stem cells (AT-MSC) cultured on the constructs. These cells were selected as a relevant stromal component of adipose tissue, which constitutes the major volume of the breast and is therefore important for evaluating biomaterials intended for post-mastectomy breast reconstruction. Scanning electron microscopy (SEM) was employed to assess the surface morphology and microstructural features of the printed scaffolds relevant for cell attachment and tissue integration.

Results: Fluorescence microscopy confirmed the presence of ECM components within the homogenate, demonstrating heterogeneous but clearly detectable distribution of structural proteins characteristic of AM tissue. Analysis of the hAM homogenate revealed the presence of multiple regenerative cytokines and growth factors, while physicochemical measurements confirmed features suitable for biomaterial preparation. Light microscopy revealed that the extrusion printing process generated scaffolds with defined structures and reproducible architecture. Cultured AT-MSC successfully attached to the scaffold surfaces, indicating compatibility of the printed biomaterial with stromal cells relevant for soft tissue regeneration. SEM further revealed characteristic surface

topography and microstructural features of the printed constructs generated during the printing and crosslinking processes.

Discussion and conclusions: Combined microscopic analyses provided complementary information on hAM-derived biomaterial organization, scaffold morphology, and their interaction with stromal cells. These findings highlight the value of integrating fluorescence microscopy, phase-contrast light microscopy and SEM for multiscale characterization of placenta-derived biomaterials and 3D-printed scaffolds. Overall, microscopic analyses support the potential of hAM-based bioactive scaffolds for applications in soft tissue engineering.

Acknowledgements: This research was supported by the Science Fund of the Republic of Serbia, grant No 11073, Determining the Potential of Placental Tissue Derivatives for Use in Post-Mastectomy Breast Reconstruction: Development of a 3D-Printed Bioscaffold- AmnioPrintCare. The study was also supported by the Slovenian Research and Innovation Agency (Grants No. P3-0108 and the MRIC UL IP-0510 Infrastructure program).
Experiments performed by Jovana Jevdosić were part of bachelor thesis work
The authors gratefully acknowledge all placenta donors whose generous contribution made this research possible. Authors also thank dr Slađana Mihajlović, dr Milan Lacković, dr Iva Bogićević, dr Ivan Hristov and Vesna Masarik for their help.

Reference:
1. 1. Janev A, Ramuta TŽ, Tratnjek L, Sardoč Ž, Obradović H, Mojsilović S, Taskovska M, Smrkolj T, Kreft ME. Detrimental Effect of Various Preparations of the Human Amniotic Membrane Homogenate on the 2D and 3D Bladder Cancer In vitro Models. *Front Bioeng Biotechnol*. **2021** Jun 25;9:690358. doi: 10.3389/fbioe.2021.690358.
2. ERDANI-KREFT, Mateja, ŽELEZNIK RAMUTA, Taja. Procedure for preparation of amniotic membrane homogenate, based antimicrobial agent = Verfahren zur herstellung eines antimikrobiellen mittels auf basis von amnionmembranhomogenat = Procédé de préparation d'un agent antimicrobien à base de broyat de membrane amniotique : Publication number EP 3 917 549 A0, 2021-12-08. Munich: European Patent Office, 2021. 43 str., ilustr.

Minor phases in Slovenian dolomites revealed by scanning electron microscopy

Lea Žibret[a], Vilma Ducman[a], Mitja Kolar[b], Jernej Imperl[b], Gorazd Žibret[c]

[a] *Slovenian National Building and Civil Engineering Institute, Ljubljana, Slovenia*

[b] *Faculty of Chemistry and Chemical Technology, University of Ljubljana, Ljubljana, Slovenia*

c Geological Survey of Slovenia, Ljubljana, Slovenia

Contact email: lea.zibret@zag.si

Introduction

Carbonate rocks cover more than 50% of Slovenian territory. Among these, thick deposits of relatively pure dolomites are widespread. Carbonate rocks in sedimentary basins are reactive and record complex histories of events associated with fluid flow in these basins, including dolomitization processes [1]. During post-diagenetic dolomitization, recrystallisation and chemical alterations affect matrix-replacive dolomites [2]. Consequently, dolomites display distinct chemical signatures, which can indicate the influence of basinal fluids triggered by specific tectonic episodes and associated volcanic activity, thus making an important contribution to understanding the geological evolution of the territory [3]. To gain better insight into the dolomitization of Slovenian dolomites, the elemental and mineralogical characteristics of dolomites from different geological ages (Upper Permian to Lower Cretaceous) and different geotectonic units have been investigated.

Methods

The common methodology for determining the mineralogical composition is X-ray powder diffraction (XRD). However, the detection limit of XRD is up to approximately 1 wt%. Consequently, in dolomite samples, only major phases (dolomite, calcite, and quartz) were detected by XRD. The measured elemental composition showed the presence of various trace elements, including REE, and suggested that some minor phases are also present in dolomites. To reveal these less abundant phases, detailed scanning electron microscopy accompanied by energy-dispersive X-ray spectroscopy (SEM/EDS) was performed. Dolomite fragments were cast in epoxy resin, polished, coated with carbon, and observed in high vacuum mode.

Results

SEM/EDS confirmed the presence of specific minerals incorporated into dolomites as minor phases, including pyrite, zircon, sphalerite, siderite, galena, cerussite, apatite, fluorite, K-feldspar, mica, hematite, rutile, uraninite, and others. Figure 1 shows an example of dolomite in which pores are filled by hematite, fluorite and galena. The minerals exhibited specific textures, which may also be characteristic of individual pore fluids that have affected the rocks.

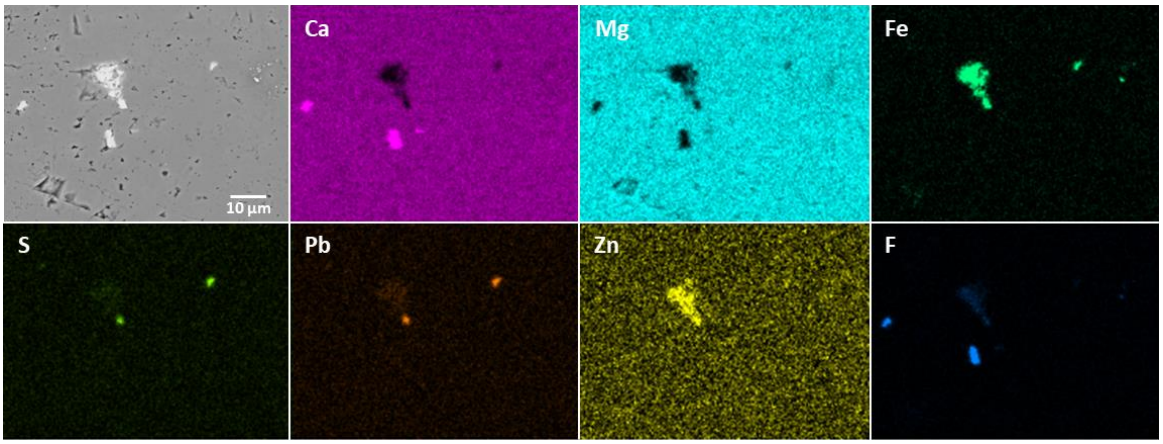

Figure 1: Elemental EDS maps for a dolomite sample with inclusion of fluorite, hematite and galena.

Discussion and conclusions

The comparison of minor phases, presented in dolomites of different geological ages and tectonic units allowed the recognition of some specific pore fluids from Upper Permian to Lower Cretaceous period. The precise microstructural observations by SEM suggested multiphase events and in some cases their relative ages. For example, hematite appeared in various textures, and some grains showed signs of dissolution (Figure 2). Minor phases formed in pores or in veins. The pore fluid phases correspond to regional geodynamic phases.

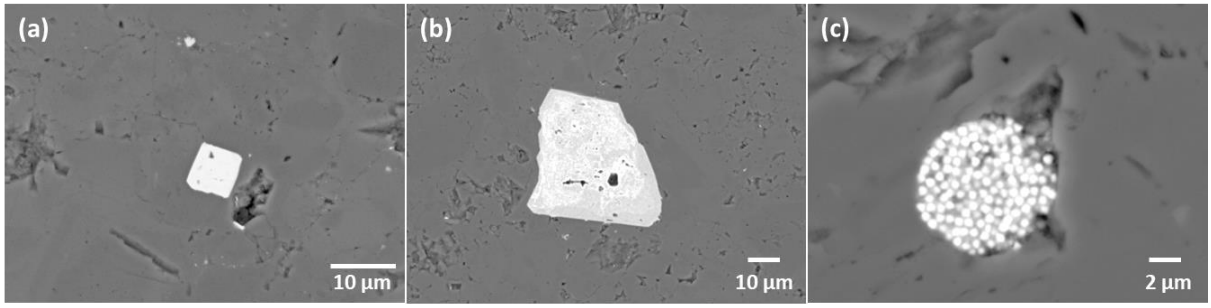

Figure 2: SEM micrographs of hematite in dolomite: (a) euhedral (idiomorphic) crystals; (b) uneven edges with signs of dissolution and (c) specific texture.

Acknowledgments

This study was financially supported by the Slovenian Research and Innovation Agency (ARIS) under project J1-50032 “Geological and lithogeochemical characterization of Slovenian dolomites including Mg extraction tests”, and research core grants P1-0025 (Mineral resources) and P2-0273 (Building structures and materials).

References:

1. E. Gomez-Rivas, M. Corbella, J.D. Martín-Martín, S.L. Stafford, A. Teixell, P.D. Bons, A. Griera, E. Cardellach, Mar. Pet. Geol. **2014**, 26–42.
2. T. Li, D. Zhu, M. Yang, X. Zhang, P. Li, C. Lu, H. Zou, Mar. Pet. Geol. **2021**, 134, 105367.
3. M.A. Gonçalves, M. Vuckovic, A. Fiorelli, P. Barrulas, J. Mirão, E3S Web Conf. **2019**, 98, 01017.

Morfogeneza prebavnih žlez: 3D struktura in kvantitativna analiza z uporabo mikro-CT, svetlobne in presevne elektronske mikroskopije

Polona Mrak[a], Urban Bogataj[a], Katja Kunčič[a], Miloš Vittori[a], Nada Žnidaršič[a]

[a]*Oddelek za biologijo, Biotehniška fakulteta, Univerza v Ljubljani, Slovenija*

Kontakt: polona.mrak@bf.uni-lj.si

Procesi morfogeneze organov, ki potekajo med embrionalnim in postembrionalnim razvojem organizma, so zapleteni in medsebojno odvisni. Zato je nujno, da morfogenezo proučujemo na nivoju organizma, organa, tkiva in celic ter vključimo analize 3D strukture in kvantifikacijo relevantnih morfoloških parametrov.

V tej študiji predstavljamo uporabo komplementarnih slikovnih tehnik za karakterizacijo morfogeneze prebavnih žlez med embrionalnim in postembrionalnim razvojem izopodnih rakov, in sicer mikro-računalniške tomografije (mikro-CT), histologije in presevne elektronske mikroskopije (TEM), v kombinaciji z morfometričnimi analizami. V raziskavo smo vključili naslednje razvojne faze: srednje embrije (faze S13, S14 in S15); pozne embrije (faza S16); zgodnje, srednje in pozne marzupijske manke; postmarzupijske manke 1-3 dni in 14 dni po sprostitvi iz valilnika (marzupija) samice. Vzorci za analize z mikro-CT so bili predhodno fiksirani v aldehidih, dehidrirani in posušeni v HMDS (heksametildisilazan). Polovico vzorcev smo dodatno postfiksirali z osmijevim tetroksidom, z namenom ovrednotenja učinka osmiranja na analize z micro-CT. Vzorce smo posneli z mikrotomografom N80 (Neoscan). Posnete 3D nize podatkov smo uvozili v programsko opremo Dragonfly (Comet) in segmentirali prebavne žleze ter pridobili 3D rekonstrukcije anatomske zgradbe žlez znotraj celotnega organizma. Na podlagi števila označenih prostorskih elementov (vokslov) smo kvantificirali volumne prvega in drugega para cevk prebavnih žlez ter zunanjega rumenjaka. Za histološke in ultrastrukturne analize smo embrije in manke fiksirali v aldehidih, postfiksirali v osmijevem tetroksidu, vklopili v smolo Agar 100 ter slikali z mikroskopom AxioImager Z1 (Zeiss) oziroma s presevnima elektronskima mikroskopoma Talos L120C (Thermo Fisher Scientific) in CM 100 (Phillips). Ker je eden od ključnih procesov morfogeneze epitela prebavnih žlez tudi diferenciacija septiranih stikov, ki v transportnih epitelih vzpostavljajo paracelularno bariero, smo na mikrografijah TEM v programu Fiji/Image J izmerili naslednje parametre septiranih stikov: i) dolžina septiranega stika (dSS); (ii) dolžina ravne linije septiranega stika (rlSS); (iii) širina medceličnega prostora v območju septiranega stika; (iv) razdalja med zaporednimi septami v nizu sept; (v) debelina posameznih sept. Iz razmerja dSS/rlSS smo izračunali indeks nagubanja stika.

Z micro-CT analizo celotnih embrijev in mank smo pridobili informacije o spremembah oblike in volumna cevk prebavnih žlez med morfogenezo znotraj intaktnega organizma. Prvi par žleznih cevk se oblikuje v fazah srednjega embrija iz zasnove žlez, ki se vzdolžno predeli v dva lobula s tvorbo epitela žlez v smeri od posteriornega proti anteriornemu delu embrija. Pri poznih embrijih ter marzupijskih in postmarzupijskih mankah se širina in volumen prvega para cevk postopno manjšata. Zasnovi drugega para cevk se izoblikujeta na anteriornem delu prvega para v fazi S14, dolžina in volumen drugega para se nato postopno povečujeta (sl. 1a, 1b). S histološko analizo smo pokazali, da se epitelne celice prebavnih žlez spremenijo iz kubičnih v kupolasto oblikovane celice B in stožčasto oblikovane celice S v fazi pozne marzupijske manke (sl. 1c). Oranžna avtofluorescenca, značilna za celice S pri odraslih ob UV vzbujanju, je bila predhodno opažena že pri poznih embrijih, zato domnevamo, da se nekateri vidiki funkcionalne in ultrastrukturne diferenciacije zgodijo pred spremembami oblike celic med morfogenezo. Septirani stiki se med razvojem embrijev in mank podaljšujejo, medtem ko se njihova ultrastruktura in arhitektura ne spreminjata bistveno. Najbolj izrazito podaljšanje septiranih stikov je bilo opazno pri prehodu iz marzupijske v postmarzupijsko manko (sl. 1č, 1d).

Z uporabo metode mikro-CT smo lahko natančno opredelili 3D anatomijo prebavnih žlez glede na ostale organe znotraj celotnih organizmov, velikih le 0,8 mm (embriji) ali 1–2 mm (manke). Ena od prednosti te metode je, da lahko prehajamo med virtualnimi prerezi vzorca v različnih orientacijah, kar nam omogoča, da posamezne strukture opazujemo z različnih zornih kotov in tako bolj celovito pojasnimo njihovo morfologijo. V osmiranih vzorcih kažejo tkiva oziroma celice bogate z lipidi zelo

močan signal, kar je koristno za številne študije, npr. za analizo količine in razporeditve lipidnih kapljic. Pridobljeni podatki kažejo, kako spremembe v obliki celic in diferenciaciji septiranih stikov v epitelu prebavnih žlez časovno sovpadajo s ključnimi spremembami oblike in volumna prebavnih žlez ter s ključnimi stopnjami embrionalnega in postembrionalnega razvoja živali. Spremembe v volumnu žlez, obliki epitelnih celic in dolžini septiranih stikov so najizrazitejše v obdobju zgodnjega postembrionalnega razvoja, ko se rumenjak v lumnu žlez porabi, žival se sprosti iz valilnika in se začne prehranjevati samostojno.

Zahvala: To raziskavo je financirala Slovenska agencija za raziskave in inovacije (ARIS) v okviru raziskovalnega programa »Integrativna zoologija in speleobiologija« (P1-0184), uporabili smo opremo infrastrukturnega centra »Mikroskopija bioloških vzorcev« (MRIC UL, I0-0022-0481-08) BF UL.

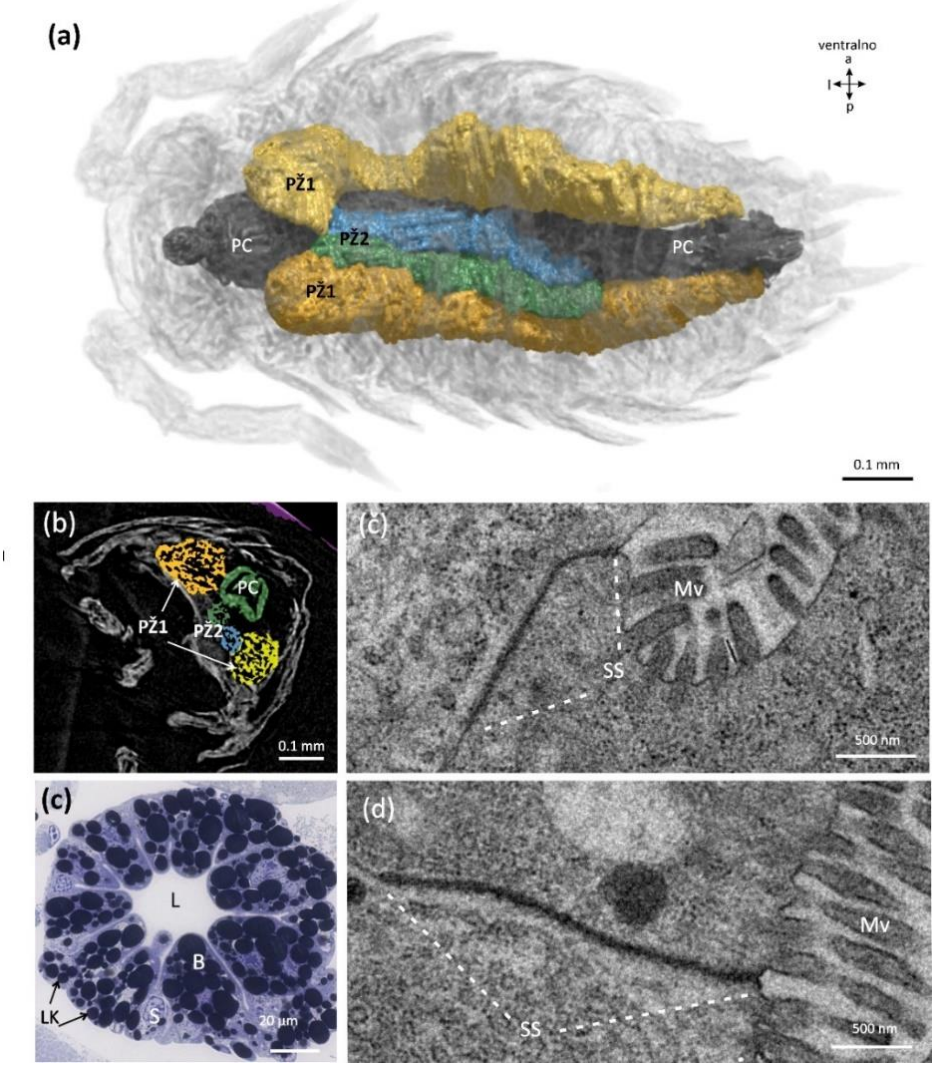

Slika 1: Od 3D anatomije do ultrastrukture prebavnih žlez med morfogenezo pri pozni marzupijski manki **(a-č)** in postmarzupijski manki **(d)**. **(a)** 3D rekonstrukcija manke, slikane z mikro-CT, s segmentiranim prebavnim sistemom. Oba para cevk prebavnih žlez (PŽ1, PŽ2) potekata ventralno in se povezujeta s prebavno cevjo (PC) v predelu stika sprednjega in zadnjega črevesa. **(b)** Virtualni 2D prečni prerez manke, pridobljen z mikro-CT. **(c)** Histološka zgradba epitela prebavnih žlez manke s celicami B in S (B, S). V celicah B je veliko lipidnih kapelj (LK). Lumen žleznih cevk (L) ne vsebuje rumenjaka. (č) Ultrastruktura apikalne strani epitela z mikrovili (Mv) ter obsežnimi septiranimi stiki (SS). (d) V fazi postmarzupijske manke so septirani stiki daljši.

Pressureless Spark Plasma Sintering vs Fast Firing sintering of Strontium hexaferrite

A. Učakar[1,2,3], A. Pajek[1], A. Kocjan[2,3], D. Salamon[4,5], P. Jenuš Belec[2]

[1] *Jožef Stefan Institute, Center for Microscopy and Microanalysis, 1000 Ljubljana, Slovenia*

[2] *Jožef Stefan Institute, Department for Nanostructured Materials, 1000 Ljubljana, Slovenia*

[3] *Jožef Stefan International Postgraduate School, 1000 Ljubljana, Slovenia*

[4] *Central European Institute of Technology Brno, University of Technology, Brno, Czech Republic*

[5] *Department of Materials Science, Montanuniversität Leoben, Leoben, Austria*

Contact email: aleksander.ucakar@ijs.si

Techniques such as pressureless Spark Plasma Sintering (pSPS) and Fast Firing (FF) allow rapid densification of strontium hexaferrite (SFO) while largely retaining a fine-grained microstructure. However, the outcome of these processes is highly sensitive to the local oxygen partial pressure and the presence of carbon, which can trigger reduction and decomposition reactions [1]. In contrast to FF where material only consolidates, during pSPS several phase and morphological changes were observed indicating the reduction of Fe^{3+} to Fe^{2+} or even metallic Fe [2,3]. A clear understanding of these processes is therefore essential for controlling densification, phase stability, and the resulting magnetic performance. Experiments revealed that commercially available SFO presents several challenges when processed by the rapid pSPS technique. In particular, phase evolution during sintering was strongly affected by the presence of carbon in the sintering environment and by the requirement for vacuum or inert atmospheres. This combination promotes metastable phase transformations that deteriorate the magnetic properties of SFO, most notably reducing coercivity. To better understand these effects, additional samples were sintered conventionally (1200 °C for 4 h) under vacuum and in inert argon atmosphere, enabling a comparison of both microstructure and magnetic behaviour. SEM-EDS analysis showed the formation of Sr-rich secondary phases surrounding SFO grains. These phases likely formed localized liquid regions during sintering, which helped initiate partial densification but simultaneously introduced microstructural heterogeneity and microcracking. Grain coalescence occurred in some regions, while other areas retained small isolated grains, resulting in an uneven pore distribution. Magnetic measurements reflected these changes, with noticeable reductions in coercivity and remanence in regions affected by reduction, consistent with the formation of soft magnetic or metallic phases following SFO decomposition. In contrast, Fast Firing experiments carried out for only 5 minutes at 1100–1300 °C in air produced dense samples that retained excellent magnetic characteristic of SFO. SEM observations and X-ray diffraction results both confirmed that the SFO phase remained stable under FF conditions, indicating that this processing route avoids the reduction-driven phase transformations which limit the effectiveness of pSPS for this material.

[1] A. Klein, D. Hotza, Advanced ceramics with dense and fine-grained microstructures through fast firing, Rev. Adv. Mater. Sci. 30 (Jun) (2012)

[2] Učakar, A., Kocjan, A., Belec, B., Košir, J., Kallio, T., Maček, M. K., Arah, B. & Jenuš, P. (2025). The role of carbon presence on the strontium hexaferrite phase decomposition during pressureless spark plasma sintering (pSPS).

[3] S. Ovtar, S. Le Gallet, L. Minier, N. Millot, and D. Lisjak, 'Control of barium ferrite decomposition during spark plasma sintering: Towards nanostructured samples with anisotropic magnetic properties', J. Eur. Ceram. Soc., vol. 34, no. 2, pp. 337–346, 2014, doi: 10.1016/j.jeurceramsoc.2013.07.027.

Acknowledgements: Slovenian Research Agency is acknowledged for funding the research programs (P2-0405, P2-0087-2) and Infrastructure Center for Electronic Microscopy and Microanalysis, Jožef Stefan Institute, Ljubljana, Slovenia (PR-05722).

Primerjava ultrastrukturnih poškodb bakterij po izpostavitvi z elektrolizirano fiziološko raztopino in klorheksidinom s transmisijsko elektronsko mikroskopijo

Marko Kolenc[1], Haris Munjaković[2,3], Tina Mikuletič[1], Irena Šest[1], Tina Triglav[1], Katja Seme[1], Aleš Fidler[4,5], Rok Gašperšič[2,3]

[1] *Inštitut za mikrobiologijo in imunologijo, Medicinska fakulteta, Univerza v Ljubljani, Ljubljana, Slovenija*

[2] *Oddelek za ustne bolezni in parodontologijo, Univerzitetni klinični center Ljubljana, Ljubljana, Slovenija*

[3] *Oddelek za ustne bolezni in parodontologijo, Medicinska fakulteta, Univerza v Ljubljani, Ljubljana, Slovenija*

[4] *Oddelek za endodontijo in restavrativno zobozdravstvo, Medicinska fakulteta, Univerza v Ljubljani, Ljubljana, Slovenija*

[5] *Oddelek za endodontijo in restavrativno zobozdravstvo, Univerzitetni klinični center Ljubljana, Ljubljana, Slovenija*

Kontaktni e-naslov: marko.kolenc@mf.uni-lj.si

Uvod

Aerosoli, ki nastajajo med zobozdravstvenimi posegi, predstavljajo pomemben vir prenosa mikroorganizmov. Poleg kvantifikacije bakterij je za razumevanje učinkovitosti antiseptikov ključen tudi vpogled v njihove učinke na bakterijsko ultrastrukturo. Namen raziskave je bil s transmisijsko elektronsko mikroskopijo (TEM) opredeliti morfološke spremembe bakterij po izpostavitvi elektrolizirani fiziološki raztopini (EOS) in jih primerjati z učinkom klorheksidina (CHX).

Metode

Modelne bakterijske vrste (*Streptococcus mitis, Streptococcus pneumoniae, Streptococcus pyogenes in Haemophilus influenzae*) smo izpostavili EOS (200 ppm, pH 7,0), CHX (0,2 %) in fosfatnemu pufru (PBS), kot negativni kontroli. Po kratkotrajni inkubaciji smo bakterijske suspenzije nanesli neposredno na mrežice, prevlečene s formvarjem, ter jih pripravili za TEM z metodo negativnega kontrastiranja z 0,5 % oz. 1 % fosfovolframovo kislino. Vzorce smo analizirali z elektronskim mikroskopom (JEM-1400 Plus; JEOL) pri pospeševalni napetosti 120 kV. Ocenjevali smo integriteto celične stene in citoplazmatske membrane ter prisotnost ekstracelularnega materiala kot pokazatelja poškodbe celičnih struktur.

Rezultati

Transmisijska elektronska mikroskopija je razkrila izrazite ultrastrukturne spremembe bakterijskih celic po izpostavitvi z EOS in CHX v primerjavi s kontrolo. Celice bakterij so v fizioloških pogojih ohranile značilno morfologijo z intaktnimi, jasno razmejenimi celičnimi stenami ter homogeno elektronsko gostoto citoplazme. Protimikrobni mehanizem delovanja EOS se je kazal z izrazitimi poškodbami celičnega ovoja, ki jih je spremljalo iztekanje znotrajceličnega materiala, kar kaže na porušeno celično integriteto. Številne morfološke spremembe so bile prisotne po izpostavitvi CHX, vključno z izgubo značilne celične oblike, porušeno integriteto celične stene ter pojavom vrzeli med citoplazemsko membrano in celično steno. Poleg tega je bilo opazno tudi zmanjšanje celičnega volumna oz. skrčenje celic.

Zaključek

TEM analiza je pokazala, da EOS povzroča nespecifične oksidativne poškodbe bakterijskih ovojnic, ki vodijo do izgube celične integritete, medtem ko CHX deluje na celične membrane, kjer povzroča izrazite deformacije in porušitve njene strukture. Ultrastrukturni vpogled dopolnjuje mikrobiološke

podatke in potrjuje potencial EOS kot učinkovitega in biološko sprejemljivejšega antiseptika pri nadzoru infektivnosti aerosolov, ki nastajajo pri zobozdravstvenih posegih.

Zahvala

Raziskavo je sofinancirala Javna agencija za raziskovalno dejavnost Republike Slovenije (ARRS P3-0083).

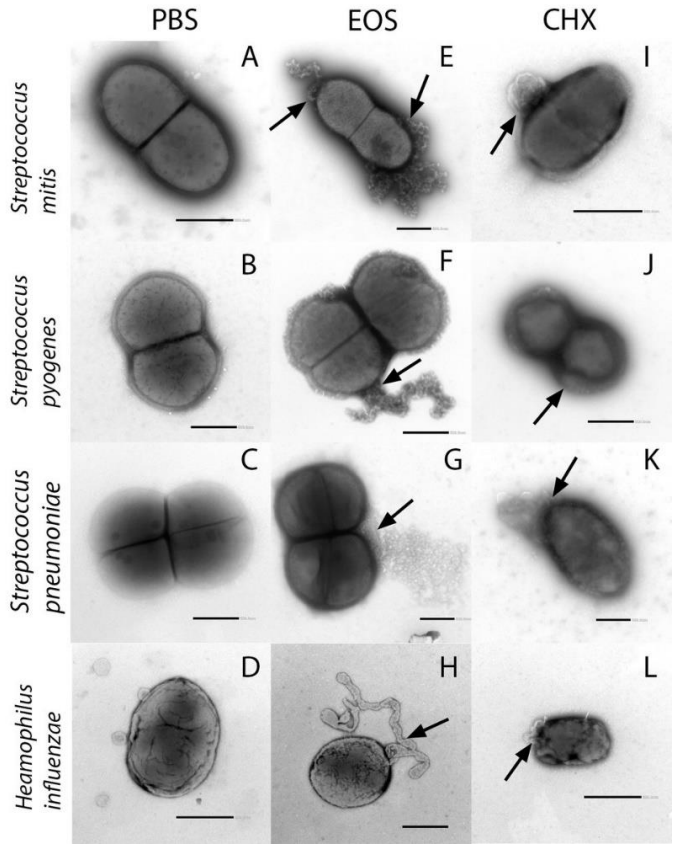

Slika 1: TEM mikrografije bakterij *S. mitis, S. pyogenes, S. pneumoniae* in *H.influenzae* po izpostavitvi fosfatnemu pufru (PBS; kontrola), elektrolizirani fiziološki raztopini (EOS) ali klorheksidinu (CHX). Merilo: 500 nm.

Reference

1. Cheung HY, Wong MM, Cheung SH, Liang LY, Lam YW, Chiu SK. Differential actions of chlorhexidine on the cell wall of Bacillus subtilis and Escherichia coli. PLoS One. **2012**.
2. Feliciano L, Lee J, Pascall MA. Transmission electron microscopic analysis showing structural changes to bacterial cells treated with electrolyzed water and an acidic sanitizer. J Food Sci. **2012**.

Real-Time Dynamics of Nickel Nanoparticles Under Bias by *In-Situ* Electrochemical Liquid-Cell TEM

Sorour Semsari Parapari[a], Layrton Jose Souza da Silva[a,b], Monica Parpal Gimenez[c], Jon Ustarroz[c], Dušan Strmčnik[d], Sašo Šturm[a,b]

[a] *Jožef Stefan Institute, Department for Nanostructured Materials, Ljubljana, Slovenia*

[b] *Jožef Stefan International Postgraduate School, Ljubljana, Slovenia*

[c] *ChemSIN, Université libre de Bruxelles (ULB), Brussels, Belgium*

[d] *National Institute of Chemistry, Ljubljana, Slovenia*

ABSTRACT

Nickel nanoparticles (Ni NPs) are promising non-noble catalysts for the hydrogen evolution reaction (HER), especially in alkaline electrolytes, because they are active, abundant, and low-cost. Their nanoscale dimensions provide a high density of tunable active sites, tunable surface facets, and enhanced metal–electrolyte interactions. However, under HER conditions, the structure and surface chemistry of these NPs can dynamically evolve in response to applied potential, local chemistry, and interaction with adsorbed intermediates, which can drive surface oxidation/reduction, formation of $Ni(OH)_x$ species, facet/defect restructuring, and in some cases dissolution–redeposition. These changes can either improve or degrade performance by altering active-site availability and reaction kinetics, making it essential to track Ni NP structure and chemistry under operating conditions. Direct visualization at high spatial resolution can provide invaluable insights into these processes. Recently developed electrochemical liquid-cell transmission electron microscopy (EC-TEM) holders enable in-situ nanoscale study of material reactions under bias[1].

In this work, we first studied the electrochemical deposition of Ni NPs in-situ at high resolutions, and then we investigated the morphological/structural/chemical modifications of these NPs in HER conditions in an alkaline solution. The in-situ EC-TEM experiments were performed using a Protochips Poseidon 500 liquid holder at a JEOL JEM ARM-200 CF using a 200 kV accelerating voltage in the bright-field mode. Experimental images and videos were recorded under standard illumination conditions for real-time imaging, with controlled electron-beam damage. The electrodeposition process of Ni NPs was conducted from 0.2 M $(NH_4)_2SO_4$ and 0.02 M $NiSO_4$ solution in ultrapure deionized water with both chronoamperometric and chronopotentiometric processes. Circular-shaped NPs ranging between 10 and 100 nm were grown on the electron-transparent glassy-carbon electrode. These NPs were then subjected to the HER process in a Na_2CO_3-based alkaline solution. The morphological and structural/chemical modifications were studied by collecting the images and diffraction patterns, respectively, during the applied bias. The results provided invaluable insights into the restructuring of electrocatalytic particles during reactions.

REFERENCES

1. M. Bernal, S. Semsari Parapari, et al., *Electrochimica Acta* 492 (2024): 144302.
2. The authors acknowledge the support from the Slovenian Research Agency through the national program P2-0084, the J2-70084, and J7-4636 ARIS projects, the ARRS-FWO bilateral project N1-0196, and FWO through contract No. G0C3121N.

STEM applications in medical mineralogy

Ruggero Vigliaturo[a], Ginevra Mango[a]

[a] *Department of Earth Sciences, Università degli Studi di Torino, 10125, Torino, Italy*

Contact email: ruggero.vigliaturo@unito.it

Introduction

Medical mineralogy explores the interactions between geomaterials and the human body, as well as the formation of inorganic precipitates in physiological and pathological conditions. Although the roots of electron microscopy date back to of the first studies of mineral particles in biological tissues (e.g. asbestos fibers and ferruginous bodies imaged in the 1940s), its advanced systematic application is somewhat limited. Scanning Transmission Electron Microscopy (STEM) offers a unique opportunity to bridge material and life sciences by providing atomic-scale information on mineral-biological interfaces.

Methods

This short review integrates studies employing STEM and ancillary techniques relevant to medical mineralogy. The focus includes aberration-corrected imaging, BF/MAADF/HAADF imaging, X-ray Energy-Dispersive Spectrometry (XEDS), Dual-range Electron Energy-Loss Spectroscopy (Dual-EELS), 4D and 5D STEM, and in situ approaches.

Results

Analysis of recent literature demonstrates that STEM enables detailed characterization of endogenous and exogenous mineral phases in tissues, revealing structural order, composition, and local bonding environments at the nanoscale. Novel 4D- and 5D-STEM methods allow correlation of crystallography, magnetic, and electrical properties with sample chemistry, providing insights into dissolution, redox processes, and phase transformation under biologically relevant conditions.

Discussion and conclusions

STEM and its recent methodological developments represent an underexploited but transformative set of tools for medical mineralogy. Through integration with complementary chemical and spectroscopic techniques, STEM can elucidate the structural and chemical mechanisms that govern mineral reactivity, biocompatibility, and pathogenicity. Continued progress in low-dose imaging, advanced detectors, and data analytics will further enhance the capability of STEM to deepen understanding of mineral-biological interactions at the atomic level.

Acknowledgments

This work was supported by the Grant for Internationalization – GFI_22_01 “Mammalian Brain Mineralogy” and GFI2_25_01_F “Nanomineral on the board – Magnetic and electric properties of nanonminerals in organic matrices” assigned to Ruggero Vigliaturo.

STEM characterization and structural evolution of a hierarchically structured CoNi-based catalyst on a ceria–alumina support for magnetically heated ammonia synthesis

Nina Križaj Kosi[a,b], Anja Sedminek[a], Janvit Teržan[c], Sašo Gyergyek[a], Darko Makovec[a,b]

[a] *Department for Materials Synthesis, Jožef Stefan Institute, Slovenia*

[b] *Jožef Stefan International Postgraduate School, Slovenia*

[c] *Department of Catalysis and Chemical Reaction Engineering, National Institute of Chemistry, Slovenia*

Contact email: nina.krizaj@ijs.si

Introduction: Heterogeneous catalysts used in industrial processes typically consist of transition-metal nanoparticles dispersed on high-surface-area supports to prevent degradation due to agglomeration and sintering [1]. The incorporation of magnetic nanoparticles into catalyst supports has recently emerged as a promising strategy to enable localized heating under a high-frequency alternating magnetic field [2, 3]. These so-called magnetic catalysts are complex nanocomposite materials composed of magnetic cores (e.g., CoNi, Fe_3O_4), supports (e.g., alumina, carbon, ceria), and catalytically active nanoparticles (e.g., Fe, Co, Ni, Ru).

The properties of such catalysts—including stability, catalytic activity, and heating efficiency—strongly depend on their nanostructure, particularly particle size, shape, composition, and structural defects [1]. Therefore, advanced electron microscopy is required for detailed characterization.

In this work, scanning transmission electron microscopy (STEM) was used to resolve the hierarchical architecture of a magnetic catalyst—composed of CoNi alloy nanoparticles ($Co_{0.67}Ni_{0.33}$) deposited on a ceria–alumina support, containing embedded CoNi magnetic nanoparticles—and to monitor its nanoscale structural evolution induced by magnetically heated ammonia (NH_3) synthesis.

Methods: The catalyst was synthesized by sequential deposition of different nanomaterials onto CoNi magnetic nanoparticles. First, the particles were stabilized by coating with an inner shell of nanostructured alumina (γ-Al_2O_3). Subsequently, a nanocrystalline ceria (CeO_2) shell was deposited, followed by deposition of smaller CoNi catalytic nanoparticles on the outer surfaces. The catalyst was then tested in NH_3 synthesis (600 °C, 5.5 MPa N_2/H_2, 8 h).

Characterization was performed at each synthesis step using a transmission electron microscope (TEM, JEOL JEM-2100, 200 kV) and a C_S-probe-corrected STEM microscope (Thermo Fisher Spectra 300, 200 kV), equipped with energy-dispersive X-ray spectroscopy (EDXS) and electron energy-loss spectroscopy (EELS) detectors. Structural stability before and after catalytic testing was examined using identical-location STEM (IL-STEM).

Results: Before catalytic testing, the catalyst consisted of larger globular CoNi magnetic nanoparticles (≈26 nm) (Fig. 1f–h, red circles) embedded within γ-Al_2O_3 nanosheets (≈30 nm lateral size, up to 3 nm thick). The magnetic support was covered with a nanocrystalline ceria shell (≈5 nm thick), composed of 3–5 nm ceria crystallites (Fig. 1f–h, yellow circles) with truncated-octahedral shape. Smaller globular CoNi catalytic nanoparticles (5–15 nm) were homogeneously distributed on the composite surfaces (Fig. 1f–h, green circles). EDXS analyses confirmed a $Co_{0.67}Ni_{0.33}$ composition for both larger and smaller CoNi nanoparticles.

After catalytic testing, IL-STEM analyses revealed that the CoNi nanoparticles and γ-Al_2O_3 support remained structurally stable, with no significant changes in particle size or morphology. In contrast, the ceria shell underwent structural evolution, manifested by sintering and partial amorphization of the initially nanocrystalline layer. STEM-EELS analysis (from the region marked in Fig. 2b) further indicated partial reduction of Ce^{4+} to Ce^{3+}, suggesting the formation of oxygen vacancies within the ceria under the reaction environment, which may influence catalytic behaviour.

Discussion and conclusions: Characterization of this hierarchically structured nanocomposite was challenging. In particular, it was difficult to distinguish between small CoNi nanoparticles deposited onto the heavy ceria support. Additionally, the material was sensitive to the electron beam. Nevertheless, the results showed that IL-STEM combined with HR-STEM imaging, EDXS, and EELS enabled direct nanoscale correlation between catalyst structure and its evolution under reaction conditions.

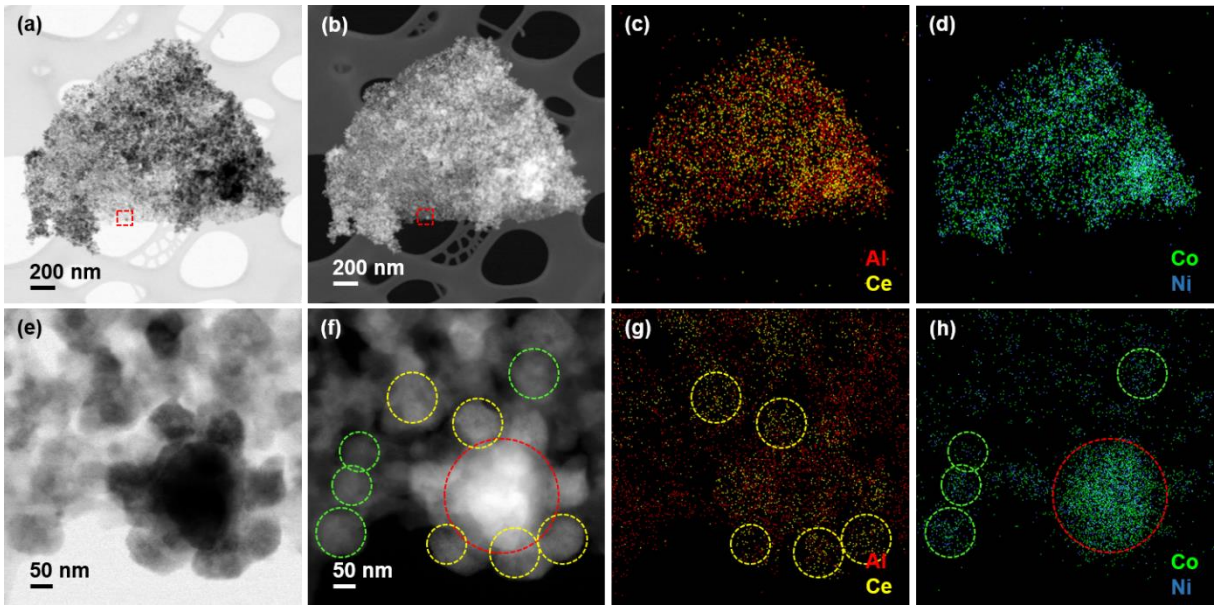

Figure 3: BF-STEM (a) and HAADF-STEM (b) images of the catalyst. HR-BF-STEM (e) and HR-HAADF-STEM (f) images of an enlarged region marked with a red rectangle in (a) and (b). Figures (c, d, g, h) are corresponding EDXS elemental maps, showing the distribution of Al (red), Ce (yellow), Co (green), and Ni (blue). In (f–h), larger CoNi nanoparticles are marked with red circles, smaller CoNi nanoparticles with green circles, and CeO_2 nanoparticles with yellow circles.

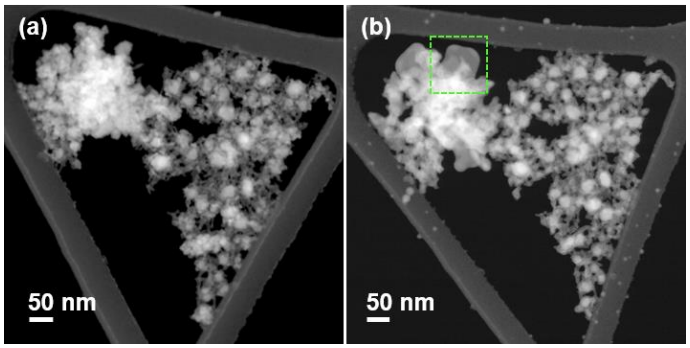

Figure 4: HAADF-STEM images of the catalyst before (a) and after (b) catalytic testing.

Acknowledgements: The authors acknowledge the financial support from the Slovenian Research Agency (ARIS) for research core funding No. P2-0089.

References:

1. M. Bowker, *Oxford University Press Inc.* **1998**.
2. N. K. Kosi, J.-S. Pavelić, M. Grilc, S. Gyergyek, D. Makovec, *J. Phys. Chem. Solids*. **2026**, 212, 113517.
3. A. Sedminek, D. Makovec, M. Huš, A. Prašnikar, S. Zakushkin, B. Likozar, J. Teržan, S. Gyergyek, *Chem. Eng. J*. **2026**, 175068.

Study of solvent impact on organometal halide perovskite crystallization via spin coating and slot die coating

Vedran Kojić[1], Lucija Klobučar[1], Stjepan Dolić[1], Krunoslav Juraić[1], Tihana Čižmar[1], Andreja Gajović[1]

[1] *Ruđer Bošković Institute (Zagreb), Croatia*

Contact email: vkojic@irb.hr

The solution-processing of organometal halide perovskite absorber layers for photovoltaic applications is governed by a hierarchy of solvent-precursor interactions, which operate across multiple length and time scales: from molecular coordination chemistry in the precursor solution to mesoscale crystallization dynamics during film formation via antisolvent treatment. Gutmann's donor number (DN), a measure of Lewis basicity, is the primary culprit that governs solvent interactions with the Pb^{2+} ions of lead halide precursors [1]. High-DN solvents (such as dimethylsulfoxide, DMSO) competitively inhibit iodoplumbate complex formation by coordinating strongly to Pb^{2+}, thereby stabilizing precursor solutions and enabling controlled thin-film deposition. Conversely, low-DN solvents (such as dimethylformamide, DMF) permit iodide complexation and perovskite crystallization, enabling large single-crystal growth.

Thin film crystallization obtained just from the solvents does not yield homogenous and reproducible thin films, as high-DN solvents often have high boiling points, leading to slow elimination of solvents as well as difficult-to-control nucleation and crystallization. To combat this issue, employment of various antisolvents is made to assist solvent elimination and inducing precipitation of perovskite crystals [2]. We identify three antisolvent categories, defined by the solubility of organic precursors in the antisolvent and its miscibility with the host solvents (primarily DMF:DMSO in the literature). Type I antisolvents (eg. alcohols, with high organic-precursor solubility) require fast application to prevent co-extraction of organic halides and consequent PbI_2 excess. Type II antisolvents (chlorinated and ester-based solvents) are largely insensitive to application rate owing to their ideal combination of low organic solubility and high host-solvent miscibility. Type III antisolvents (non-polar aromatics, immiscible with host solvents) require slow application to allow sufficient time for host solvent diffusion across the liquid-liquid interface.

In slot-die coating however, the absence of centrifugal driving force necessitates external quenching techniques, which include air-knife gas flow and/or antisolvent bathing, to substitute for the crystallization driving force provided by spin-coating [3]. Solvent selection criteria closely parallel those identified in the spin-coating literature: high-DN, high-boiling-point co-solvents such as DMSO are used to widen the processing window and stabilize intermediate phases, while low-boiling-point primary solvents such as acetonitrile and 2-methoxyethanol enable fast coating speeds appropriate future scale-up production. In our work we aim to compare both spin coating and slot-die coating thin film preparations using the same primary solvents and antisolvents to investigate the difference in the morphology of the prepared films, as well as their optical properties.

Acknowledgements

We acknowledge the cooperation between the Government of the Republic of Croatia and the Government of the State of Israel with co-financing from the Ministry of Science, Education and Youth Croatia, project „Novel perovskite solar cells with enhanced performance based on hybrid halide perovskite/transition-metal disulfides nanocomposites (Sol-HP-TMD-NanoComp)."

References:
1. J. Clay Hamill et al., *ACS Energy Lett.* **2018**, *3*, 92-97.
2. A.D. Taylor et al., *Nat. Commun.* **2021**, *12*, 1878.
3. K. K. Shin Thant et al., **2025**, 15, 2403088

The Glomerulus in Bloom: Ultrastructural Tapestry of Collagenofibrotic Glomerulopathy

BMC Nephrology - Images in nephrology contest - first place winner

Jerica Pleško[a], Željka Večerić-Haler[b], Nika Kojc[a]

[a]*Institute of Pathology, Faculty of Medicine, University of Ljubljana, Ljubljana, Slovenia*

[b]*Department of Nephrology, University Medical Centre Ljubljana, Ljubljana, Slovenia*

Contact email: jerica.plesko@mf.uni-lj.si

Introduction: Collagenofibrotic glomerulopathy (CFG) is a very rare, non-immune kidney disease characterized by abnormal deposition of type III collagen in the glomeruli. Its cause is unknown, and type III collagen is not normally present in healthy glomeruli, so its accumulation indicates a disorder of extracellular matrix production [1]. Most cases are sporadic, though rare familial forms with autosomal recessive inheritance exist [2,3]. The disease is often under-recognized because its histopathological features resemble more common conditions such as diabetic nephropathy, amyloidosis, and membranoproliferative glomerulonephritis. Therefore, accurate diagnosis requires ultrastructural analysis [1,4].

Methods: This study presents a case report of a 71-year-old male with nephrotic-range proteinuria and chronic kidney disease. A kidney biopsy was performed and evaluated using light microscopy (LM), immunofluorescence (IF), and electron microscopy (EM). LM assessed glomerular morphology, while IF evaluated immune complex deposition. For ultrastructural analysis, ultrathin sections were examined using a transmission electron microscope (JEM-1400 Flash, Jeol, Japan) following contrast enhancement with lead citrate and phosphotungstic acid, as described by Gubler et al [2].

Results: LM revealed marked mesangial expansion with a nodular sclerosis-like appearance and lobular accentuation, findings that were non-specific and suggestive of deposition disease. IF was negative for immunoglobulins and complement, supporting a non-immune process. EM proved decisive, demonstrating abundant fibrils with a characteristic periodicity of 40–65 nm located in the mesangial matrix and subendothelial space. These fibrils formed irregular, curved, and loosely bundled structures with frayed ends, consistent with type III collagen deposition. Clinically, the patient exhibited progressive renal decline and reached kidney failure within five years despite supportive therapy.

Discussion and conclusion: This case highlights the critical role of EM in diagnosing CFG, particularly when LM and IF findings are inconclusive. The distinctive ultrastructural pattern of type III collagen fibrils is essential for differentiating CFG from other glomerular diseases with similar morphological features. In conclusion, awareness of this rare entity and appropriate use of EM are crucial for accurate diagnosis and optimal clinical management.

References:

1. Wilson AV, Costigliolo F, Farris AB, Rengen R, Arend LJ. Collagen Type III Glomerulopathy. Kidney Int Rep. 2021;6(6):1738–42.

2. Gubler MC, Dommergues JP, Foulard M, Bensman A, Leroy JP, Broyer M, et al. Collagen type III glomerulopathy: a new type of hereditary nephropathy. Pediatr Nephrol. 1993;7(4):354–60.

3. Tamura H, Matsuda A, Kidoguchi N, Matsumura O, Mitarai T, Isoda K. A family with two sisters with collagenofibrotic glomerulonephropathy. Am J Kidney Dis. 1996;27(4):588–95.

4. Alchi B, Nishi S, Narita I, Gejyo F. Collagenofibrotic glomerulopathy: clinicopathologic overview of a rare glomerular disease. Am J Kidney Dis. 2007;49(4):499–506.

Toward Safe Antimicrobial Coatings: Safety Assessment of Upconverter Particles

Veno Kononenko[1], Matej Hočevar[2], Tina Petrišič[1], Špela Saje[1], Valentina Perc[1], Pascal Kock[3], Simone Schulte[3], Stefan Fischer[3], Damjana Drobne[1]

[1]*University of Ljubljana, Biotechnical faculty, Ljubljana, Slovenia*

[2]*Institute of Metals and Technology (IMT), Ljubljana, Slovenia*

[3]*Evonik Operations GmbH, Essen, Germany*

Contact email: veno.kononenko@bf.uni-lj.si

Introduction: Upconverter particles (UCPs) are promising materials for antimicrobial coatings due to their ability to convert low-energy radiation into UV light, inducing microbial DNA damage without conventional biocides. However, their safety profile remains insufficiently understood. This study evaluates the toxicological impact of UCPs within a Safe-by-Design (SbD) framework.

Methods: Human toxicity was assessed *in vitro* using multiple cell lines, standard cytotoxicity assays, fluorescence microscopy, and SEM. Ecotoxicity was evaluated across aquatic and terrestrial model organisms. *Tetrahymena thermophila* was used for cytotoxicity and uptake studies, *Daphnia magna* for acute aquatic toxicity (48 h immobility), and *Porcellio scaber* for terrestrial effects in a 14-day feeding experiment, including organism-level and biochemical endpoints. Experiments were conducted under dark and blue light conditions.

Results: UCPs showed low toxicity across all systems. No cytotoxicity was observed in HaCaT, L929, or *T. thermophila*, and no particle uptake was detected in *T. thermophila*. In *D. magna*, effects occurred only at ≥50 µg/mL, with no light-dependent differences. No adverse effects were observed in P. scaber at the organism level. Mild biochemical changes were detected only at high concentrations, indicating limited sublethal responses.

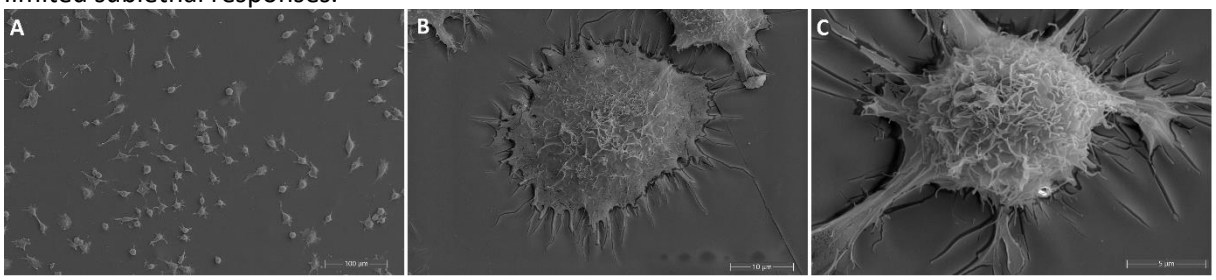

Figure 1: Morphology of L929 cells cultured on blue-light-irradiated surfaces coated with upconverter particles shows no signs of toxicity.

Discussion and conclusions: UCPs exhibit minimal toxicity across multiple systems, with effects limited to high, environmentally unrealistic concentrations. The absence of cytotoxicity, cellular uptake, and organism-level impacts supports their favorable safety profile. Compared to conventional antimicrobials, UCPs show reduced ecological risk and no photo-induced toxicity. These findings support their potential as a safe platform for antimicrobial coatings in line with SbD principles.

Acknowledgements: This research has received funding from the Horizon Europe Framework Programme (grant agreement number 101058554), from the Swiss State Secretariat for Education, Research and Innovation (SERI), from the UK Research and Innovation (UKRI) (grant number 10042534 & grant number 10055606) as part of the Horizon Europe [HORIZON-CL4-2021-RESILIENCE-01]. This work was supported by the Slovenian Research and Innovation Agency (ARIS) grants P1-0207, P2-0424, P1-0184, P2-0132, and J2-60051. This work has been supported by the infrastructural center "Microscopy of biological samples", (MRIC UL, I0–0022–0481–08) located at the University of Ljubljana, Biotechnical faculty.

Tuning Magnetic Order in Barlowite through Selective Zn^{2+} Incorporation

Polona Umek[a], Zvonko Jagličić[b,c], Matej Pregelj[a,d], Matjaž Gomilšek[a,d] and Andrej Zorko[a,d]

[a]*Jožef Stefan Institute, Ljubljana, Slovenia*

[b]*Faculty of Civil and Geodetic Engineering, University of Ljubljana, Ljubljana, Slovenia*

[c]*Institute of Mathematics, Physics and Mechanics, Ljubljana, Slovenia*

[d]*Faculty of Mathematics and Physics, Ljubljana, Slovenia*

Contact email: Polona.Umek@ijs.si

Quantum spin liquid (QSL) materials exhibit an exotic magnetic ground state in which spins evade conventional long-range magnetic order down to $T = 0$ K and remain highly quantum entangled [1,2]. One of the most prominent experimental realisations of QSL materials is Herbertsmithite ($Cu_3Zn(OH)_6Cl_2$) [3,4]. Another structurally related compound is Barlowite ($Cu_4(OH)_6FBr$), which features an undistorted S = 1/2 kagome lattice. However, Barlowite contains additional Cu^{2+} ions at the interlayer sites (Figures 1 a and 1 **b**), which induce magnetic ordering at 15 K and thus prevent the realisation of a QSL state [5]. Density functional theory calculations predict that substitution of the interlayer Cu(II) with nonmagnetic Zn(II) ions should suppress long-range magnetic order and potentially stabilise a QSL ground state [6]. Therefore, substitution of interlayer Cu(II) ions with Zn(II) ions represents a promising route toward new QSL candidates.

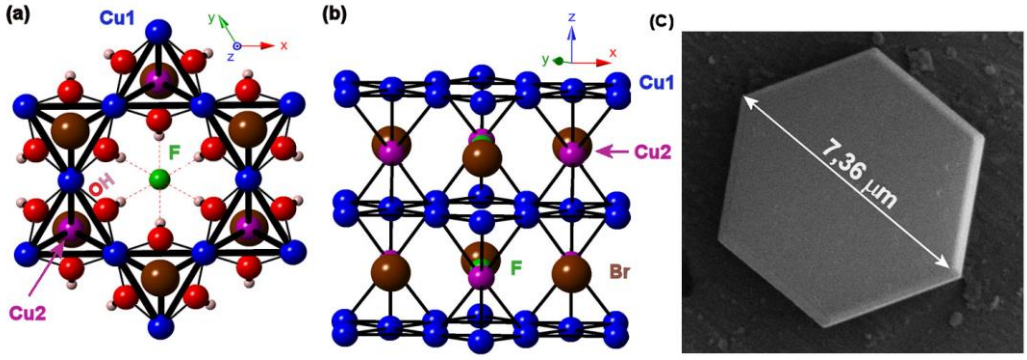

Figure 1: Crystal structure of Barlowite when looking perpendicular (**a**) and almost parallel (**b**) to the kagome lattice. The symbols are kagome Cu1, blue; interkagome Cu2, purple; O, red; H, salmon; F, green; Br, brown. A plate-like crystallite of Barlowite with a characteristic hexagonal shape (**c**).

In this work, we systematically investigated hydrothermal synthesis strategies for Barlowite for the substitution of Cu^{2+} with Zn^{2+}, targeting the composition $Cu_3Zn(OH)_6FBr$ through selective replacement of interlayer Cu(II) ions. Basic copper carbonate ($Cu(OH)_2 \cdot CuCO_3$) was used as the copper precursor, while $ZnBr_2 \bullet 2H_2O$ served as the zinc source. Bromide anions were supplied by $ZnBr_2 \bullet 2H_2O$, HBr(aq), and/or NH_4Br, and fluoride ions by NH_4F or HF(aq). The reactions were carried out under hydrothermal conditions at 180 °C for 72 hours, and the Cu : Zn molar ratios ranged from 4 : 0 to 3 : 1 (+ an additional one with the ratio 3 : 1.25).

Phase purity and crystal structure were examined by powder X-ray diffraction, confirming the preservation of the Barlowite structure upon Zn^{2+} substitution.

The morphology and chemical composition of the synthesised samples were analysed using field-emission scanning electron microscopy (SEM) combined with energy-dispersive X-ray spectroscopy (EDX). SEM images reveal the formation of hexagonal microcrystals characteristic of Barlowite (Figure 1**c**). EDX analysis confirms successful incorporation of Zn^{2+} into the crystalline framework. However, at

higher nominal substitution ratios (i.e., above 3.5 : 0.5), the zinc content gradually reaches a maximum value slightly above 5 at.%. The amounts of fluorine and bromine in Cu_4FBrO_4 should be 8.3 at. % but are higher by about 1 and 2 at. % for both ions, respectively.

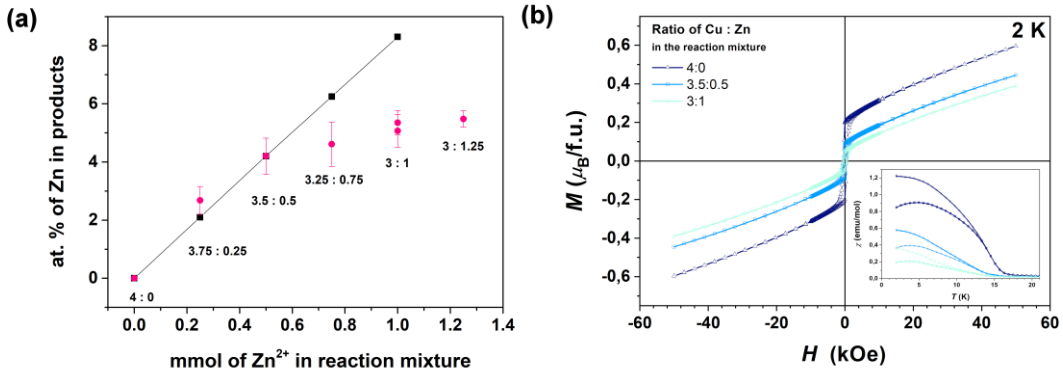

Figure 2: At. % of Zn for the products synthesised in the batch where the source of F^- was HF(aq) (**a**). Black squares correspond to the at. % of zinc for $Cu_{4-x}Zn_xFBrO_4$. Magnetisation curves measured for Barlowite products with a substitution ratio 4 : O, 3.5. : 0.5, and 3 : 1 (**b**).

Magnetic properties were investigated between 2 K and 300 K on polycrystalline samples. The room-temperature effective magnetic moments calculated per Cu(II) ion range from 1.56 to 1.64 μ_B, values slightly smaller than those expected for isolated spin-1/2 ions, as previously reported for single crystals of $Cu_4(OH)_6FBr$ [5]. Below 20 K, all investigated compounds exhibit a steep increase in magnetic susceptibility (Inset to Figure 2 **b**), clearly indicating a magnetic phase transition into a canted antiferromagnetic state. The main influence of Zn incorporation is reflected in the remanent magnetization measured at 2 K. It decreases from 0.20 μ_B per formula unit in the 4 : 0 compound to 0.05 μ_B per formula unit in the 3:1 compound (Figure 2 **b**).

References:

[1] P. W. Anderson, *Science* **1987**, 235, 1196.

[2] A. Kitaev and J. Preskill, *Phys. Rev. Lett.* **2006**, 96, 110404.

[3] M. P. Shores, E. A. Nytko, B. M. Bartlett and D. G. Nocera, *J. Am. Chem. Soc.* **2005**, 127, 13462.

[4] T.-H. Han, J. S. Helton, S. Chu, D. G. Nocera, J. A. Rodrigues-Rivera, C. Broholm, and Y. S. Lee, *Nature* **2012**, 492, 406.

[5] H. O. Jeschke, F. Salvat-Pujol, E. Gati, N. H. Hoang, B. Wolf, M. Lang, J. A. Schlueter, and R. Valenti, Phys. Rev. B **2015**, 92, 094417.

[6] Z. Feng, Z. Li, X. Meng, W. Yi, Y. Wei, J. Zhang, Y.-C. Wang, W. Jiang, Z. Liu, S. Li, F. Liu, J. Luo, S. Li, G.-Q. Zheng, Z. Y. Meng, J.-W. Mei, and Y. Shi, *Chin. Phys. Let.* **2017**, 34.

[7] R. W. Smaha, W. He, J. M. Jiang, J. Wen, Y.-F. Jiang, J. P. Sheckelton, C. J. Titus, S. G. Wang, Y.-S. Chen, S. J. Teat, A. A. Aczel, Y. Zhao, G. Xu, J. W. Lynn, H.- C. Jiang, and Y. S. Lee, *npj Quantum Mater.* 2020, **5**, 1.

Transition Metal Dichalcogenide Nanotube Modification of Titanium Dioxide Bilayer Films for Enhanced Electrical and Photoelectrochemical Performance

Vedran Kojić[a], Stjepan Dolić[a], Krunoslav Juraić[a], Alla Zak[b], Alexander Laikhtman[b], Andreja Gajović[a]

[a] *Ruđer Bošković Institute (Zagreb), Croatia*

[b] *Holon Institute of Technology (Holon), Israel*

Contact email: sdolic@irb.hr

TMD nanotube materials have been shown to have optimal electrical properties in terms of charge-carrier collection and transport.[1] This research aims to enhance the performance of titanium dioxide (TiO_2) thin films, which are often used as electron transport layers (ETLs) in perovskite solar cells. Titanium dioxide is often used in perovskite photovoltaics for this purpose due to its optimal valence band energy and high transmission in the visible spectrum.[2] Transition metal dichalcogenide (TMD) nanotubes, specifically tungsten disulfide (WS_2), have been incorporated into the thin film's structure of a TiO_2 bilayer, consisting of a compact and mesoporous layer, with the aim of enhancing the electrical properties of TiO_2 thin films

WS_2 nanotubes, synthesized via a high-temperature vapor-gas-solid reaction, were incorporated into a TiO_2 bilayer comprising a compact and a mesoporous layer. The TMD nanotubes were incorporated into either the compact or the mesoporous TiO_2 layer. The structural and morphological characteristics of the resulting composite films were analyzed using Scanning Electron Microscopy (SEM), and the results were compared with the electrical and photoelectrochemical performance evaluated via current-voltage (*J-V*) measurements and cyclic voltammetry.

When incorporated into TiO_2 bilayers, SEM analysis revealed significant differences in nanotube integration across layers. In the compact TiO_2 layer, nanotubes were observed sporadically, poorly embedded, and often overcoated by TiO_2, indicating weak incorporation. In contrast, when incorporated into the mesoporous TiO_2 overlayer, nanotubes were more effectively integrated and uniformly dispersed due to the porous structure of the mesoporous layer. This structural difference, clearly visualized by SEM images, correlated directly with electrical measurements. Integration of WS_2 nanotubes into the mesoporous layer resulted in a significant increase in photocurrent from 53 mA cm^{-2} to 154 mA cm^{-2} at +1.5 V and a transition from ohmic to diode-like behavior.

The findings indicate that strategic placement of TMD nanotubes within the TiO_2 bilayer is essential for enhancing ETL performance. SEM results provide clear visual evidence that the porous structure of the mesoporous TiO_2 layer is crucial for effective incorporation of TMD nanotubes. This improved structural integration enables TMD nanotubes to function as efficient photosensitizers and charge-carrier collectors, resulting in enhanced photocurrent and improved *J-V* curve rectification. In contrast, poor embedding of nanotubes within the compact layer, as observed by SEM, led to less pronounced performance improvements. In conclusion, modification of the mesoporous layer with WS_2 nanotubes represents a promising strategy for fabricating high-performance ETLs for next-generation perovskite solar cells.

Acknowledgements

We acknowledge the cooperation between the Government of the Republic of Croatia and the Government of the State of Israel with co-financing from the Ministry of Science, Education and Youth Croatia, project „Novel perovskite solar cells with enhanced performance based on hybrid halide perovskite/transition-metal disulfides nanocomposites (Sol-HP-TMD-NanoComp)."

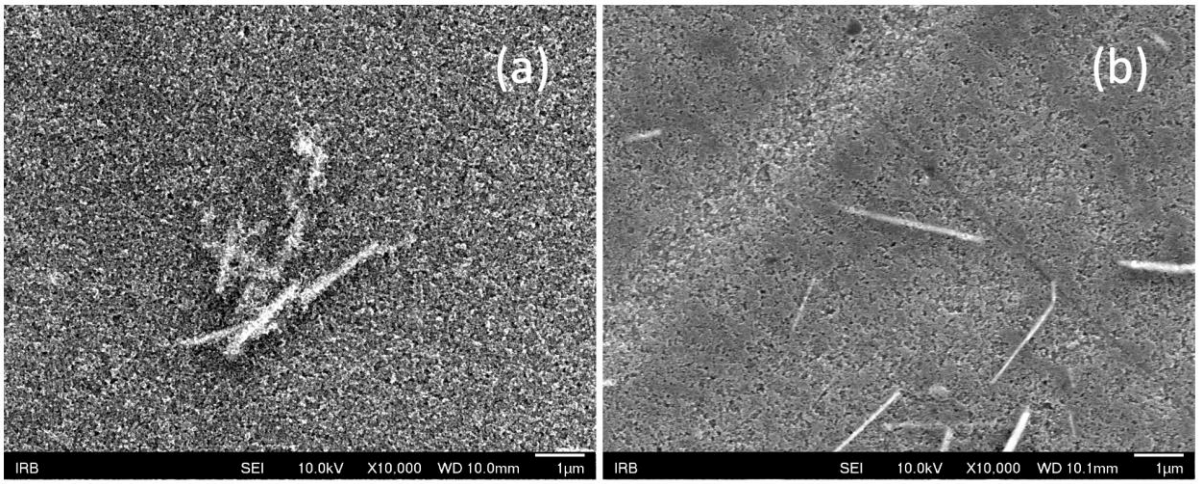

Figure 1. SEM images of a TiO_2 bilayer, where WS_2 nanotubes are incorporated into the (a) compact, and (b) mesoporous layer.

References:
1. S. S. Sinha et al., *J. Phys. Chem. C* **2021**, *125*, 6324−6340.
2. X. Chen et al., *J. Mater. Chem. A* **2016**, *4*, 6521−6526.

Transformations of metallic boride nanoparticles from synthesis to post-oxygen evolution reaction

Nina Daneu, Joyal Johny, Matjaž Spreitzer, Suraj Gupta

Advanced Materials Department, Jožef Stefan Institute, Jamova 39, 1000 Ljubljana, Slovenia

Contact email: nina.daneu@ijs.si

Introduction. Transition-metal (TM) borides are among the most promising catalysts for oxygen evolution reaction (OER), however, the borides are not the final product but act only as pre-catalyst that undergoes surface reconstruction to TM double layered hydroxides during OER to form the active metal species in high oxidation states. The role of boron in the activity and stability of the final catalysis is still debated. In this work, we prepared a multimetal precursor Co-Fe-Mo-B (CFMB) excellent performance (1 A cm^{-2} at ~2.05 V) in an anion-exchange membrane (AEM) electrolyzer along with remarkable stability (>840 h)[1][2]. In this work, we followed the transformation of the CFMB catalyst from the synthesis to oxygen evolution reaction by a combination of transmission electron microscopy techniques.

Methods. CFMB catalyst nanoparticles (NPS) were prepared by dissolving $Na_2MoO_4.2H_2O$, $CoCl_2.6H_2O$ and $FeCl_3.6H_2O$ sequentially in DI water at temperature below 10 °C. Then, $NaBH_4$ aqueous solution was added dropwise forming black powder precipitate. The precipitate was collected, washed and dried. Part of the powder was annealed in N_2 atmosphere, at 300 °C and 500 °C for for 2h to obtain CFMB-300 and CFMB-500 catalysts respectively. Electrochemical characterizations of the prepared catalysts were done in three electrode cell and 5cm^2 single cell AEM electrolyzer with 1M KOH electrolyte. The CFMB nanopowders at all stages of preparation and testing (as-received, annealed, after OER) were characterized by scanning transmission electron microscopy (STEM), energy dispersive spectroscopy (EDS) and electron energy loss spectroscopy (EELS) using Cs-corrected microscope Spectra 300 (Thermo Fisher, Netherlands) operated at 200 kV.

Results and Discussion. The as-synthesized CFMB nanoparticles have spherical morphology typical for TM-borides prepared by wet chemistry route as shown in the HAADF-STEM (**Fig**. **1a**). The NPs have amorphous metallic core composed of Co, Fe and B and a small amount of Mo surrounded by oxidized shell due to surface oxidation. The distribution of B, O, Fe and Co was determined by EELS. The oxidation states of B, Co and Fe were additionally confirmed with detailed analysis of the B-K, Fe-L and Co-L edges in the EELS spectra. After annealing at 300 °C, the core remains amorphous with Co, Fe and B, while the surface becomes covered with a thin layer of B-oxide that protects the nanoparticles from further oxidation (**Fig**. **1b**). This indicates gradual boron migration from the interior of the samples towards the surface at increased temperature. Out-diffusion of boron from the metallic core becomes even more evident after annealing at 500 °C, where the core of the nanoparticles becomes crystalline Co-Fe, while boron is significantly depleted from the bulk and forms an even thicker boron-oxide layer on the surface of the nanoparticles (**Fig**. **1c**). The temperature-instigated migration of boron to the surface and the formation of boron oxide surface layer results in thickening of the oxide shell to about 6 - 7 nm, completely engulfing the multi-metallic core of the catalyst. EELS analysis showed that the catalyst surface became enriched with boron oxide during heat treatment with minimal contributions from the metals, which were mainly present in the interior bulk of the catalyst. Electrochemical screening has shown that CFMB-300 is the most active OER catalyst composition and was thus used to study the reaction mechanism through post-mortem investigations. STEM shows that the nanoparticulate morphology of the CFMB-300 catalyst is partially maintained but new sheet-like features were also observed after OER (**Fig**. **1d**). EELS map and spectra indicate that the sheets comprise of Co, Fe, O along with a low amount of B and, according to EDS, also a low amount of Mo. The results suggest that during OER, the starting catalyst nanoparticles comprised of Co-Fe-Mo-B core and B-O shell undergo gradual structural transformation (recrystallization) into crystalline nanosheets. The nanosheets are OER-active CoFe oxyhydroxide ((Co/Fe)OOH) as confirmed through measured interplanar spacing of the sheets and analysis of O, Fe and Co EELS edges.

Conclusions. Based on the results of STEM analyses, we uncovered a fundamental pathway in amorphous CFMB metal NPs, where boron migrates to the surface upon annealing to form a protective B-oxide shell that preserves the metallic cores. Under alkaline OER, this shell dissolves, increases the accessible surface area, and exposes the preserved metal sites that convert into the active metal (oxy)hydroxide state.

Acknowledgments. We acknowledge funding by European Innovation Council within ANEMEL project (grant agreement no. 101071111). Support by Slovenian Research and Innovation Agency for financing of the research projects within research program P2–0091 is also gratefully acknowledged.

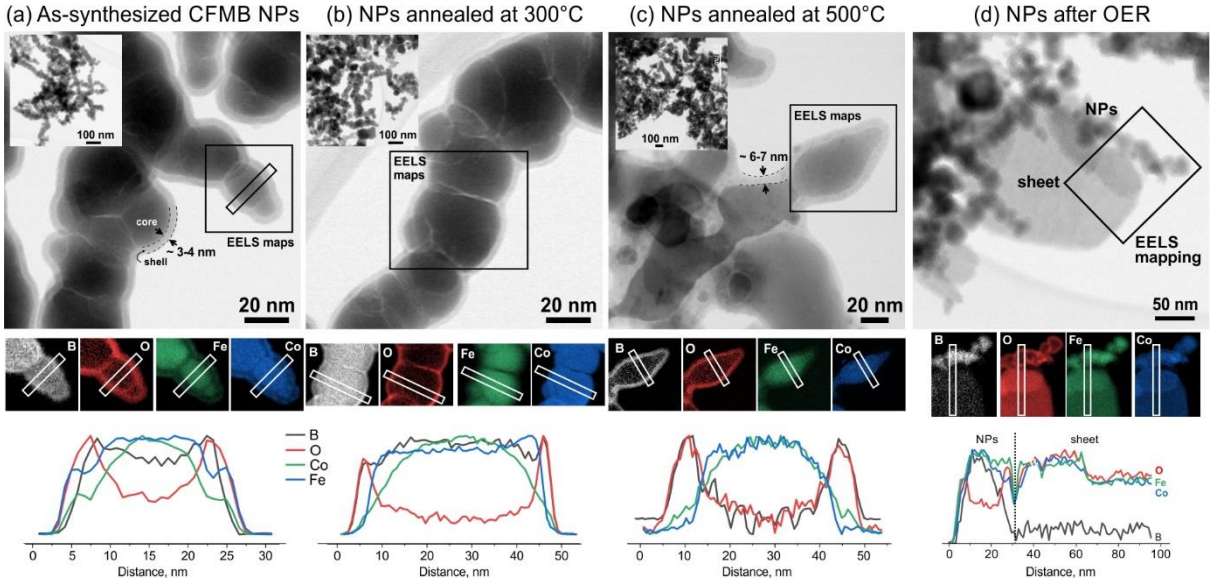

Figure 1: STEM and EELS analysis of CFMB NPs at different stages of synthesis and transformation: (a) as-prepared NPs, (b) after annealing at 300 °C in N, (c) after annealing at 500 °C in N and (d) after OER.

References:

[1] G. Liu *et al.*, "Amorphous CoFeBO nanoparticles as highly active electrocatalysts for efficient water oxidation reaction," *Int. J. Hydrogen Energy*, vol. 43, no. 12, pp. 6138–6149, 2018.

[2] S. Gupta, N. Patel, R. Fernandes, S. Hanchate, A. Miotello, and D. C. Kothari, "Co-Mo-B Nanoparticles as a non-precious and efficient Bifunctional Electrocatalyst for Hydrogen and Oxygen Evolution," *Electrochim. Acta*, vol. 232, pp. 64–71, 2017.

Tracking PS-Eu nanoplastics in *Daphnia magna*: linking uptake to sublethal effects

Valentina Perc [1], Victor Wepener [2], Gregor Marolt [3], Matej Hočevar [4], Damjana Drobne [1], Sara Novak [1]

[1]*University of Ljubljana, Biotechnical faculty, Ljubljana, Slovenia*

[2]*Water Research Group, Unit for Environmental Sciences and Management, North-West University, Potchefstroom, South Africa*

[3] *University of Ljubljana, Faculty of chemistry and chemical technology, Ljubljana, Slovenia*

[4]*Institute of Metals and Technology (IMT), Ljubljana, Slovenia*

Contact email: valentina.perc@bf.uni-lj.si

Introduction: The increasing presence of nanoplastics in aquatic environments raises concerns about their bioavailability and sublethal effects on freshwater organisms. This study investigated the biodistribution and behavioral impacts of europium-labeled polystyrene nanoplastics (PS-Eu NPs; spherical, 100 µm) in the freshwater crustacean *Daphnia magna* at environmentally relevant concentrations.

Methods: Neonates of *D. magna* (n = 20) were exposed in three independent experiments to PS-Eu nanoparticles at concentrations of 0.0005, 0.001, 0.1, 1, and 5 mg/L. Acute toxicity was assessed using the standardized OECD TG 202 assay by evaluating immobility after 48 hours. For biodistribution analysis, organisms exposed to 0.1, 1, and 5 mg/L were fixed in Carnoy B, dehydrated through a graded alcohol series, embedded in paraplast, and analyzed using laser ablation inductively coupled plasma mass spectrometry (LA-ICP-MS). In three additional experiments, organisms were exposed to 0.0005, 0.001, and 1 mg/L, followed by behavioral assessment of swimming activity, quantified as total distance moved.

Results: Immobility of *D. magna* occurred only at the highest tested concentration (5 mg/L). LA-ICP-MS analysis of longitudinal body sections revealed a concentration-dependent presence of europium, predominantly localized within the digestive tract and on the external surface of the organisms. No distribution to other tissues was detected, indicating that particles were either ingested or adhered externally. Behavioral analysis showed a significant reduction in swimming activity at environmentally relevant concentrations (0.0005, 0.001, and 1 mg/L), demonstrating impaired locomotion even at low exposure levels.

Discussion: The results indicate that although acute toxicity was observed only at the highest tested concentration of PS-Eu nanoparticles (5 mg/L), the ingested and surface-adsorbed material induced behavioral alterations even at the lowest tested concentrations. The observed reduction in swimming activity highlights the sensitivity of behavioral endpoints and suggests that sublethal effects can occur at environmentally relevant exposure levels. Such impairments have the potential to negatively influence key ecological functions, including feeding efficiency, predator avoidance, and reproductive success. The combined use of LA-ICP-MS imaging and behavioral assays provides a robust framework for linking internal nanoparticle exposure to functional biological outcomes, thereby offering a more comprehensive understanding of nanoplastic toxicity.

Conclusions: Environmentally relevant concentrations of PS-Eu nanoplastics accumulate in *D. magna* and induce significant sublethal behavioral effects. These findings emphasize the importance of incorporating sensitive behavioral endpoints into ecotoxicological risk assessments and contribute to growing evidence that nanoplastics pose a subtle but significant risk to freshwater invertebrates and ecosystem stability.

From Microstructure to Magnetism: Lorentz TEM Study of Domain Structures in NdFeB Micromagnets

Sergej Ražnjević[a], Vinko Sršan[a], Sašo Šturm[a]

[a] *Department for Nanostructured Materials, Jožef Stefan Institute, Jamova cesta 39, 1000 Ljubljana, Slovenia*

Understanding the relationship between microstructure and magnetic behaviour is essential for optimizing the performance of NdFeB permanent magnets, particularly at the microscale. In this work, we investigate the magnetic domain structures and magnetization processes in a focused ion beam (FIB)-prepared NdFeB micromagnet using transmission electron microscopy (TEM), with a special emphasis on Lorentz (Fresnel) TEM imaging.

A thin lamella (10 µm × 10 µm × 100 nm) was extracted from bulk NdFeB material with an average grain size of approximately 300 nm. Lorentz TEM, operated under low-field conditions to preserve the intrinsic magnetic configuration, enabled direct visualization of magnetic domains and domain walls through defocus-dependent contrast (Fig. 1). Three domain configurations were identified: lamellar, finger-like, and spaghetti/vortex domains. Lamellar domains, typically associated with high coercivity due to alignment along the crystallographic easy axis (c-axis), were found to be scarce in the investigated micromagnet. In contrast, finger-like and complex vortex-like domains were predominant, indicating locally disturbed magnetic anisotropy, grain misorientation, and reduced coercivity.

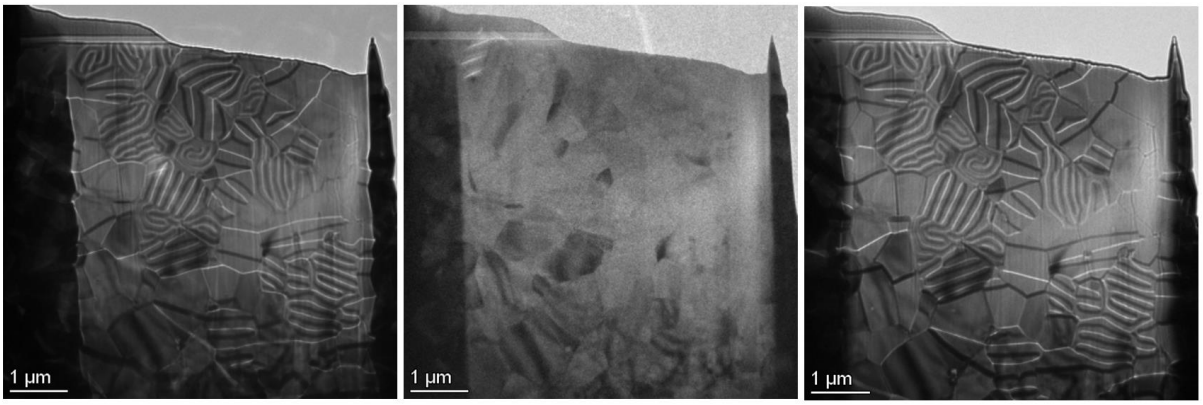

df = -943 µm **df = 0** **df = 943 µm**

Figure 5: Principle of Fresnel (Lorentz) TEM imaging for magnetic domain observation. Under in-focus conditions (df = 0), no magnetic contrast is visible. Defocused imaging reveals domain walls through Lorentz deflection of the electron beam: over-focus (df > 0) produces dark contrast, while under-focus (df < 0) produces bright contrast, with contrast reversal between the two conditions.

In-situ magnetization experiments were performed by applying controlled magnetic fields via the objective lens, calibrated using a Hall probe. The magnetization process was followed from the virgin state through progressive field application up to ±0.8 T. The evolution of domain structures revealed a transition toward single-domain states under increasing field, followed by magnetization reversal upon field inversion. These observations provide insight into the mechanisms of domain wall motion and pinning at the microscale.

Structural characterization using high-angle annular dark-field (HAADF) imaging confirmed that the grains are highly crystalline, while orientation mapping based on diffraction pattern analysis revealed local variations in grain alignment. Chemical analysis showed the presence of Nd-rich, Fe-poor triple junctions and minor carbon inclusions; however, these features exhibited no significant influence on the observed magnetic domain configurations.

The combination of Lorentz TEM imaging and in-situ magnetic field application provides a powerful platform for directly correlating magnetic configurations with structural features at the nanoscale. This approach enables real-time observation of domain evolution, offering valuable insight into the fundamental mechanisms governing micromagnetic behavior.

Overall, our findings demonstrate that in NdFeB micromagnets, magnetic behaviour is governed more strongly by geometrical factors and domain structure complexity than by chemistry or crystallinity alone. These insights contribute to a deeper understanding of micromagnetic phenomena and may inform the design of advanced permanent magnetic materials with tailored properties.

Acknowledgements

The authors acknowledge the Slovenian Research Agency (ARRS) for financial support under Program P2-0084.

Formation of metamorphic moissanite from Pohorje Mountains

Tim Sotelšek [a], Jesse B. Walters[b], Marian Janák[c], Sergej Ražnjević[d], Nik Gračanin[d], Sašo Šturm[a,d], Mirijam Vrabec[a]

[a]*University of Ljubljana, Faculty for Natural Sciences and Engineering, (Ljubljana), Slovenia*

[b]*University of Graz, Department of Earth Sciences, (Graz), Austria*

[c]*Slovak Academy of Sciences, Geological Institute, (Bratislava), Slovak Republic*

[d]*Institute Jožef Stefan, (Ljubljana), Slovenia*

Email: tim.sotelsek@ntf.uni-lj.si

Introduction Moissanite (SiC) is a rare mineral formed by bonding of Si^{4+} and C^{4-}, but most Earth environments are too oxygen-rich, causing silicon to exist as SiO_2. Thus, silicate minerals dominate Earth's crust and mantle (>90%). Despite this, moissanite has been reported in kimberlites, volcanic rocks, mantle-derived ultramafic rocks, and metamorphic rocks. It is often associated with diamond, amorphous material, and metal silicides, suggesting formation under ultra-reducing, high-pressure–temperature conditions. Experiments indicate SiC is stable only at oxygen fugacities 4–9 log units below the iron–wüstite buffer, far lower than typical crustal and mantle conditions (ΔIW ≥ +4), leaving its origin debated [1–5].

A key problem is that SiC cannot coexist in equilibrium with Fe-bearing silicates and oxides, yet they are commonly found together. Proposed explanations include formation under ultrahigh-pressure conditions deep in the mantle or in localized ultra-reduced domains caused by fluid processes. However, such environments are difficult to sustain, and preservation during magma transport is unlikely. Alternative hypotheses suggest contamination or formation by lightning strikes at extreme temperatures. Because most findings are not in situ, their origin remains uncertain.

This study examines moissanite inclusions in well studied diamond bearing garnets from Slovenian metamorphic rocks [4,6]. Using advanced analytical techniques, results confirm its presence and suggest formation through post-entrapment modification via hydrogen diffusion, without requiring extremely low oxygen conditions.

Methods Samples of metapelitic gneiss from the Pohorje Mountains were prepared as polished thin sections using Al_2O_3 abrasives to avoid SiC contamination and cleaned ultrasonically. Mineral phases were identified by micro-Raman spectroscopy (LabRAM HR, green Nd:YAG laser, 532 nm). A moissanite-bearing inclusion was extracted as an electron-transparent lamella using FIB–SEM technique (Helios NanoLab 600i Dual Beam System). Detailed structural and chemical characterization was then carried out by TEM (Spectra 300, operated at 200 kV), including EDXS, SAED, STEM–HAADF imaging, and EELS. Graphite, synthetic SiC and diamond were used as reference materials. Phase equilibria of the metapelitic gneiss was modelled using the Perple_X software in a Na-K-Ca-Fe-Mg-Ti-Mn-Al-Si-C-H_2-O_2 system, allowing Fe, C, and H speciation to vary freely via Gibbs free energy minimization.

Results Moissanite occurs with multiple phase assemblages, including diamond, disordered graphite, carbonates, pyrophyllite, CO_2, and CH_4. Inclusions containing fluid phases are fully enclosed within the host garnet. TEM analysis of a moissanite-bearing inclusion in garnet provides detailed insight into its microstructure and phase relationships. The studied inclusion is a well-faceted, negative crystal-shaped cavity approximately 6 × 4 µm in size. Raman spectroscopy performed prior to lamella cutting confirmed the presence of moissanite, carbonate, diamond, and graphite within the inclusion. TEM analysis of this inclusion of the extracted lamella shows moissanite, amorphous material, and carbonaceous phases, while carbonate was likely lost during preparation. Selected area electron diffraction (SAED) confirms that the central grain is monocrystalline cubic moissanite (β-SiC, space group F-43m), with measured interplanar distances matching reference data within 1% (Fig. 1a). High-

resolution HAADF–STEM imaging further verifies its atomic structure, consistent with crystallographic models (Fig. 1b). The moissanite grain contains abundant nanoscale pores and inclusions (5–25 nm), mostly spherical and unevenly distributed. Inclusions are enriched in Fe and Al.

Two carbon-bearing grains are identified as diamond (Dia#1 and Dia#2), attached to cavity walls; one is in contact with moissanite. Electron energy-loss spectroscopy confirms graphite associated with one diamond grain. Amorphous material is also present, as shown by diffuse SAED patterns. Its composition resembles the host garnet but is enriched in O and C and depleted in major cations (Si, Al, Ca, Mg, Fe), with significant chemical variability.

The modeled C–O–H fluid composition is CH_4-dominated. The results indicate that peak UHP fluids formed along the CH_4–H_2O join, with negligible CO_2 present. Corresponding fO_2 conditions range from $\log_{10} fO_2 \approx -18$ to -20 (Fig. 1c) significantly higher than those required for moissanite stability, making such reduced conditions incompatible with the observed mineral assemblage.

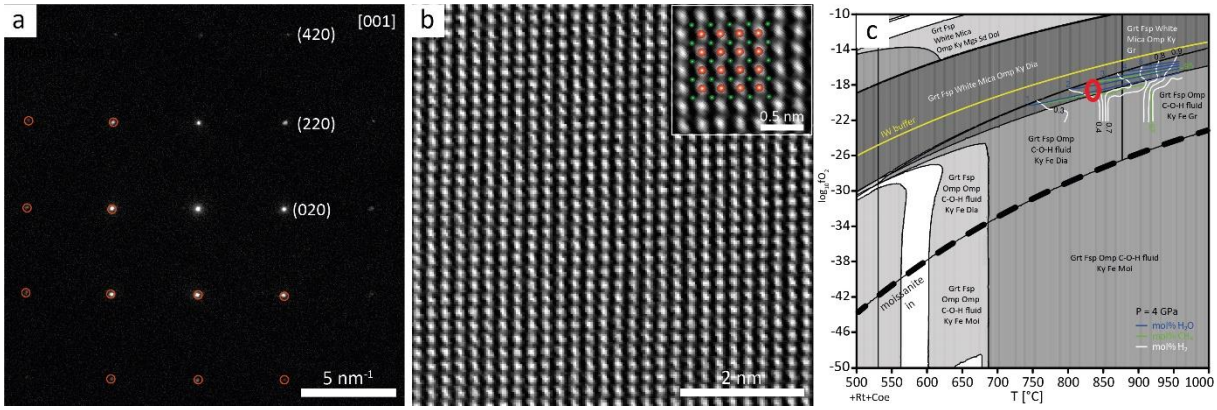

Figure 6: Crystallographic and HAADF–STEM characterization of moissanite and calculated thermodynamic stability. (a) Indexed SAED spot pattern of a moissanite grain with superimposed simulated ED patterns (red circles) for reference in zone axis [001]. (b) Image showing detailed atomic structure. The inset shows the simulated atomic model of moissanite superimposed on the magnified, noise-filtered experimental image (Si shown as red spheres, C as green spheres). (c) T–fO_2 diagram calculated at 4 GPa for the system with 2.0 wt% bulk H_2O content. Mol% isopleths of H_2O, CH_4, and H_2 in the system at peak metamorphic conditions shown in blue, green, and white, respectively.

Discussion and conclusions Moissanite identified within garnet-hosted inclusions from the Pohorje metapelites is confirmed as natural by Raman spectroscopy and TEM, which show it is fully encapsulated and associated with diamond, carbonate, and graphite. Its β-SiC structure, Fe–Al–rich nanoscale inclusions, and distinct defect patterns further distinguish it from synthetic counterparts and support a natural origin. The presence of Al-bearing phases is particularly significant, as such compositions are inconsistent with industrial SiC formation conditions [2,3,7]. These microstructural and compositional features collectively indicate formation in a high-pressure metamorphic environment. However, thermodynamic modeling indicates that UHP conditions were too oxidized for its stability, implying it did not form in equilibrium with the host assemblage. Instead, we propose post-entrapment modification during which fluid interacted with host garnet. Hydrogen diffusion during decompression drove the reactions that converted CH_4 to CO_2 and SiC (and other observed phases), enabling moissanite formation without requiring low fO_2 conditions.

References

1. L. Dobrzhinetskaya et al., *Lithos* **2018**, 310–311, 355–368.
2. J. X. Huang et al., *Sci. Bull.* **2020**, 65, 1479–1488.
3. E. A. Mathez et al., *Geochim. Cosmochim. Acta* ***1995***, 59, 781–791.
4. M. Janák et al., *J. Metamorph. Geol.* **2015**, 33, 495–512.
5. V. S. Shatsky et al., *Russ. Geol. Geophys.* **2025**, 66, 1–17.
6. T. Sotelšek et al., *J. Metamorph. Geol.* **2026**, 44, 226–245.
7. S. Di Pierro et al., *Am. mineral.* **2016**, 101, 71–81.

Ab-initio and STM investigation of the $Nd_2Fe_{14}B$ surface

Sana Saeed[a], Willfried Bajoun Mbajoun[b], Abhirami Suresh[b], Vincent Fournée[b],

Julin Ledieu[b], Matej Komelj[a], Kristina Žužek[a], Sašo Štrum[a],

a: Jožef Stefan Institute, Department for Nanostructured Materials, Jamova cesta 39, SI-1000 Ljubljana, Slovenia

b: Institute Jean Lamour, Campus Artem, 2 allée André Guinier, 54011 Nancy, France
Contact email: sana.saeed@ijs.si

Introduction:

During the last decades, significant efforts have been made to improve the performance of $Nd_2Fe_{14}B$-based permanent magnets, essential in various technologies[1]. Although the $Nd_2Fe_{14}B$ phase intrinsically exhibits exceptionally high magnetocrystalline anisotropy, real magnets often fail to reach this potential. The discrepancy is commonly attributed to microstructural effects, such as the presence of secondary phases, grain boundaries and interfaces, and secondary phases. The coercivity observed in Nd-Fe-B permanent magnets represent only 20% of what is theoretically possible, which calls for significant improvements[2]. While surfaces and thin films are generally expected to enhance magnetic anisotropy due to the breaking of the respective-bulk symmetry, $Nd_2Fe_{14}B$ surfaces are often regarded as the source of a degraded magnetic performance. In this work, we examine the surface structure of $Nd_2Fe_{14}B$ single crystals and present a combined experimental and computational characterization of the $Nd_2Fe_{14}B(001)$ surface[3].

Methods:

A $Nd_2Fe_{14}B$ single crystal was grown applying the Nd-rich self-flux method and oriented along the [001] direction using Laue back-reflection diffraction. The $Nd_2Fe_{14}B(001)$ surface was prepared by means of Ar^+ sputtering followed by annealing, and its long-range order, symmetry, morphology, and atomic arrangement were characterized by LEED and room-temperature STM.

DFT calculations were performed using OpenMX within the LSDA framework. The investigated surface was described by introducing a 1.364 nm thick vacuum layer along the z direction, resulting in supercell dimensions of 12.411 ×12.411 ×24.239. Simulated scanning tunneling microscopy (STM) images were calculated from the converged electronic structure using the local density of states (LDOS) within the framework of the Tersoff–Haman approximation. The tunneling current was obtained by integrating the LDOS over an energy window ranging from −1.8 eV to the Fermi level, corresponding to a bias voltage of −1.8 V.

Results:

The LEED pattern was recorded after each preparation cycle. From the 10th cycle onward, annealing at 858–872 K produced sharp LEED spots with low background intensity, as shown in Fig. 1(a), indicating a well-ordered surface. Calibration using Al(111) gave a square surface unit mesh with $a_s = b_s = 12.4 \pm 0.2$ Å, corresponding to √2 times the bulk lattice parameter. This confirms a (√2 × √2)R45°, or c(2 × 2), surface reconstruction. Following the LEED analysis, STM measurements were carried out on the area of surface. The atomically resolved STM image in Fig. 1(b) exhibits more details on the local atomic arrangement. The FFT analysis yields the surface lattice parameter a=b=12.3 Å, indicating C(√2×√2, 45°) surface reconstruction. The atomic arrangement of the $Nd_2Fe_{14}B(001)$ surface in Fig. 1(c) presents the relationship between the unreconstructed and reconstructed surface unit cells. The black square denotes the primitive 1 × 1 surface unit cell of the bulk-terminated $Nd_2Fe_{14}B(001)$ surface, whereas the red square indicates the reconstructed c(2 × 2) unit mesh. The lateral dimensions of 12.41 Å × 12.41 Å match a rotation by 45° with respect to the original surface lattice, corresponding to a (√2 × √2)R45° surface reconstruction. To reproduce the experimentally observed c(2 × 2) surface structure, several atoms were selectively removed from the Nd-rich surface plane, resulting in the surface model sketched in Fig, 1 (d) consistent with the STM-resolved periodicity.

The simulated STM image, generated for this model, are shown in Fig 1 (e) in good agreement with the experimental data.. The tunneling current was obtained by integrating the LDOS over an energy window ranging from −1.8 eV to the Fermi level, corresponding to a bias voltage of −1.8 V.

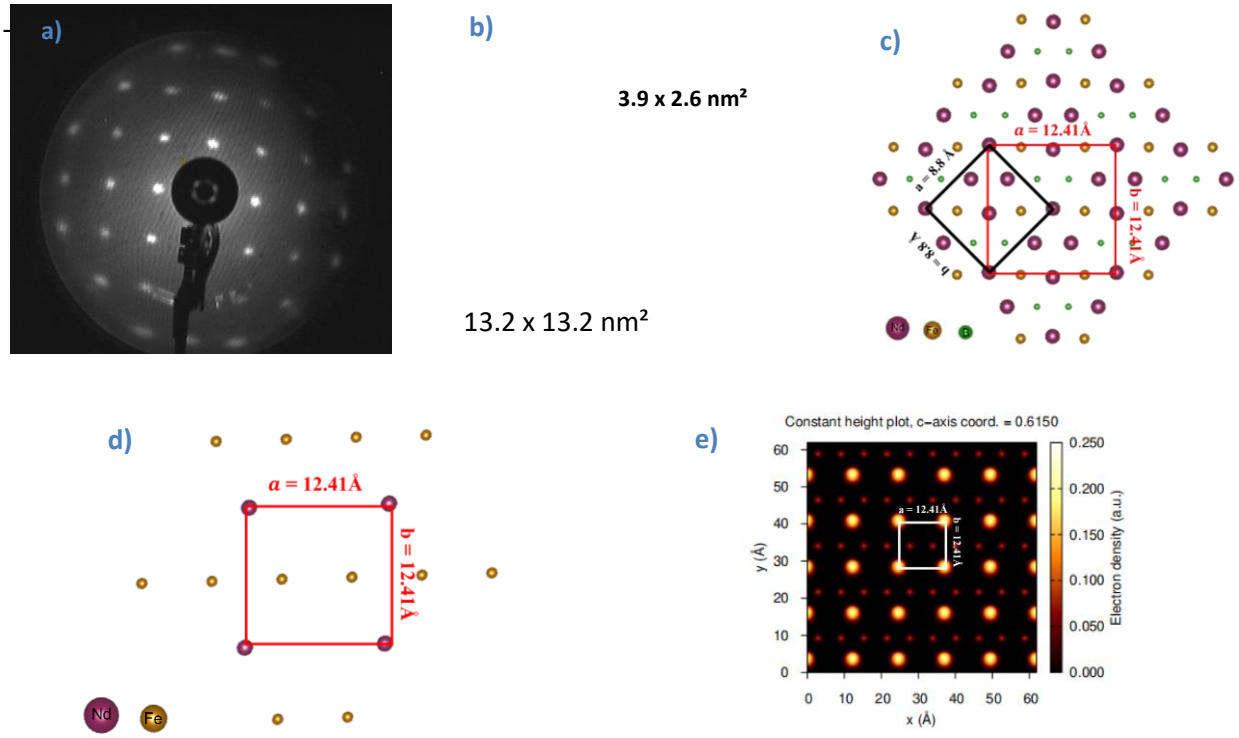

Figure 1: (a)LEED pattern recorded at 20 eV after annealing the sample at 872 K. (b) Atomic resolution STM image (13.2 x 13.2 nm^2,V_b = -1.80 V, I_t = 0.1 nA) [inset: Zoom on (b)] obtained after a change in the tip state. (c) Atomic arrangement of the $Nd_2Fe_{14}B(001)$ surface. (d) Proposed reconstructed surface model. (e) Simulated STM image.

Conclusion

The combined LEED, STM, and DFT results confirm that the $Nd_2Fe_{14}B(001)$ surface forms a well-ordered c(2 × 2) reconstruction after sputtering and annealing. The agreement between the experimental and simulated STM images indicates that the reconstructed surface model obtained by selective removal of atoms from the Nd-rich plane reliably represents the atomic structure of the $Nd_2Fe_{14}B(001)$ surface. This validated surface-model will serve as the basis for further DFT investigations of the surface magnetic properties, including layer-resolved magnetic moments, spin polarization, and the general interpretation for the relation between thesurface reconstruction and magnetic behavior.

References:

1. Becker, J.J., 1970. Rare-Earth-Compound Permanent Magnets. Journal of Applied Physics, 41(3), pp.1055-1064.
2. Tang, X., Li, J., Sepehri-Amin, H., Bolyachkin, A., Martin-Cid, A., Kobayashi, S., Kotani, Y., Suzuki, M., Terasawa, A., Gohda, Y. and Ohkubo, T., 2023. Unveiling the origin of the large coercivity in (Nd, Dy)-Fe-B sintered magnets. NPG Asia Materials, 15(1), p.50.
3. Nishino, M., Uysal, I.E. and Miyashita, S., 2021. Effect of the surface magnetic anisotropy of neodymium atoms on the coercivity in neodymium permanent magnets. Physical Review B, 103(1), p.014418.

Synthesis-dependent defect formation in Li-rich oxides: role of temperature and chelating chemistry

Rabail Badar Abbasi[1], Giuliana Aquilanti[2], Jasper Plasier[2], Marjan Bele[1], Anton Meden[3], Robert Dominko[1,3,4], Elena Tchernychova[1,5]

[1]*Department of Materials Chemistry, National Institute of Chemistry, Ljubljana, Slovenia*

[2]*Elettra-Sincrotrone Trieste S.C.p.A., s.s. 14 km 163.5, 34149 Basovizza, Trieste, Italy*

[3]*Faculty of chemistry and chemical technology, University of Ljubljana, Slovenia*

[4]*ALISTORE-European Research Institute, Amiens, France*

[5]*Institute of Metals research and Technology, Ljubljana, Slovenia*

Contact email: elena.tchernychova@imt.si

Li-rich layered oxides (LROs) are among the most promising high-voltage cathode materials for next-generation lithium-ion batteries (LIBs) due to their high practical energy density, low cost, and ability to access anionic redox, enabling capacities exceeding 250 mAh g^{-1}. However, their practical application is limited by low initial coulombic efficiency, voltage decay, capacity fading, and poor rate capability. These challenges are closely associated with oxygen redox activity, transition-metal (TM) migration, and progressive transformation of the layered structure into spinel- or rocksalt-like phases during cycling. The complexity of these degradation mechanisms is strongly influenced by synthesis-induced crystallographic defects, making defect chemistry a key parameter for improving performance.

In this work, $Li_{1.2}Mn_{0.54}Co_{0.13}Ni_{0.13}O_2$ was synthesized via sol–gel methods, systematically varying chelating agents and calcination temperatures to tune defect formation. The resulting materials were characterized using synchrotron X-ray diffraction (λ = 0.8265 Å, 15 keV) at the MCX beamline (ELETTRA, Trieste), alongside high-resolution transmission electron microscopy (HRTEM) and STEM-HAADF imaging to probe local structure and stacking disorder. Diffraction data in the low-angle region (11–15°) exhibit asymmetric peak features indicative of stacking faults, whose concentration depends on synthesis conditions. Higher calcination temperatures reduce fault density, while citric acid as a chelating agent yields lower peak asymmetry compared to stronger chelators.

These structural variations are correlated with defect chemistry, including stacking disorder and oxygen vacancy formation, which influence oxygen redox reversibility and TM migration. The results demonstrate that synthesis parameters directly govern defect populations and, consequently, electrochemical behavior and phase stability. This study highlights the importance of detailed structural characterization and controlled defect engineering to better understand and optimize LRO cathodes, providing a foundation for improving their performance in high-energy LIB applications.

Acknowledgements: This work has received funding from the European Union Horizon 2020 research and innovation PhD program DESTINY under grant agreement No. 945357. Co-financing from the Slovenian Research Agency ARIS (core program funding P2-0423, projects J2-3050 and JV-4637) are acknowledged.

Conventional Cross-Sectional TEM Sample Preparation for Structural Analysis of PEALD-Grown ZnO Thin Films

Tina Radošević[1], Daria Jardas Babić[2], Damjan vengust[1], Aleš Omerzu[2], Matejka Podlogar[1]

[1]*Jožef Stefan Institute, Jamova Cesta 39, 1000 Ljubljana, Slovenia*

[2]*University of Rijeka, Faculty of Physics, Radmile Matejčić 2, 51000 Rijeka, Croatia*

Contact email: tina.radosevic@ijs.si

Thin ZnO films prepared by plasma-enhanced atomic layer deposition (PEALD) are promising materials for photocatalytic applications, particularly when low-temperature deposition is required for thermally sensitive substrates. Detailed nanoscale characterization is essential for understanding their structure, including crystallinity, grain size, orientation and the film/substrate interface.

In this contribution, we present the conventional cross-sectional preparation of TEM samples for the structural analysis of PEALD-grown ZnO thin films. The preparation involved cutting ZnO-coated substrates, mounting them face-to-face into a 3 mm brass ring using epoxy resin, mechanical thinning to approximately 100 µm, dimpling to about 20 µm in the central region, and final ion milling with Ar^+ ions to achieve electron transparency. Prior to TEM analysis, a thin carbon coating was applied to reduce charging under the electron beam.

This preparation approach enabled high-resolution TEM imaging and electron diffraction analysis of ZnO films deposited under different PEALD conditions. The obtained cross-sections provided direct insight into the evolution from amorphous or nanocrystalline structures to more ordered ZnO films with increasing deposition temperature or plasma RF power. These results demonstrate that conventional cross-sectional TEM preparation remains a reliable and powerful approach for correlating synthesis parameters with the nanoscale structure and functional properties of thin oxide films.

References:
1. D. Jardas Babić, *et al.* Relation between structural and photocatalytic properties of thin ZnO films synthesised by plasma-enhanced atomic layer deposition, Ceramics International, 51, 43289, 2025, DOI: 10.1016/j.ceramint.2025.07.068
2. D. Jardas Babić, *et al.* Photocatalytic properties of thin ZnO films synthesised with plasma-enhanced atomic layer deposition at room temperature, Vacuum, 240, 114504, 2025, DOI: 10.1016/j.vacuum.2025.114504

FIB-Prepared TEM Lamellas for Cross-Sectional Analysis of TiO_2-Cu Thin Films

Nik Gračanin[1], Ivana Jelovica Badovinac[2], Ivna Kavre Piltaver[2], Peter Robert[2], Matejka Podlogar[1]

[1]*Jožef Stefan Institute, Jamova Cesta 39, 1000 Ljubljana, Slovenia*

[2]*University of Rijeka, Faculty of Physics and Center for Micro- and Nanosciences and Technologies, Radmile Matejčić 2, 51000 Rijeka, Croatia*

Contact email: nik.gracanin@ijs.si

Atomic layer deposition (ALD) enables the preparation of thin composite films with precise control over thickness, composition and nanostructure. However, understanding the distribution of embedded nanoparticles within such thin films requires site-specific sample preparation and high-resolution cross-sectional analysis. In this contribution, we present the focused ion beam scanning electron microscopy (FIB-SEM) preparation of electron-transparent lamellas for transmission electron microscopy (TEM) investigation of ALD-grown TiO_2-Cu composite films.

The studied TiO_2-Cu films contain copper nanoparticles incorporated into an anatase TiO_2 matrix during ALD growth. While surface and cross-sectional SEM analysis revealed changes in film morphology and the presence of Cu-rich features, TEM analysis of FIB-prepared lamellas provided direct insight into the internal structure of the films and the position of Cu nanoparticles within the TiO_2 matrix. In the study, the lamella was prepared from the middle of the film and thinned to reveal the cross-sectional composition within the layer, enabling HAADF-STEM image along with EDS elemental maps. Cross-sectional TEM confirmed that Cu nanoparticles are embedded within the TiO_2 layer, while high-resolution imaging revealed the coexistence of anatase TiO_2 grains and metallic Cu crystallites. The analysis showed that TiO_2 grains can terminate at Cu inclusions or grow around them, demonstrating the importance of cross-sectional TEM for understanding local interfaces in nanocomposite thin films.

This work highlights FIB-SEM as an essential preparation technique for site-specific TEM analysis of thin-film photocatalysts. By enabling direct visualization of incorporated nanoparticles, interfaces and grain structure, FIB-prepared TEM lamellas provide critical information for correlating synthesis conditions, nanoscale structure and functional photocatalytic performance.

Reference:
1. I. Jelovica Badovinac, *et al.* Synergistic enhancement of solar photocatalysis in ALD-grown TiO_2-Cu composite films, Surfaces and Interfaces, 73, 107570, 2025, DOI: 10.1016/j.surfin.2025.107570

Microscopy-Based Characterization of Micro- and Nanoplastics

Tina Radošević[1], Damjan Vengust[1], Nik Gračanin[1], Klara Laura Cokan[1], Marko Kozjek[2], Pia Leban[1], Janja Vidmar[1], Manca Kovač Viršek[3], Vasyl Shvalya[1], Matejka Podlogar[1]

[1]*Jožef Stefan Institute, Jamova Cesta 39, 1000 Ljubljana, Slovenia*

[2]*Institute for water of the Republic of Slovenia, Einspielerjeva 6, 1000 Ljubljana, Slovenia*

[3]*National Institute of Biology, Večna pot 121, 1000 Ljubljana, Slovenia*

Contact email: matejka.podlogar@ijs.si

Micro- and nanoplastics represent a complex and analytically challenging class of environmental pollutants, especially at the nanoscale, where conventional techniques often fail. In this contribution, we present a multimodal analytical approach with a strong emphasis on electron microscopy, complemented by vibrational spectroscopy, for the comprehensive characterization of micro- and nanoplastic particles.

Electron microscopy techniques, including SEM, ESEM and TEM, provide detailed insight into particle morphology, surface features and internal structure at different length scales, depending on particle size and sample complexity. Elemental characterization is performed using energy-dispersive X-ray spectroscopy (EDS), which is integrated into all microscopy platforms. These approaches are complemented by Raman spectroscopy and surface-enhanced Raman scattering (SERS), which enable reliable chemical identification and improved sensitivity for the detection of plastic nanoparticles. In particular, tailored vertical plasmonic substrates enabled the detection of 100 nm polystyrene (PS) particles, demonstrating the potential of SERS for the analysis of ultra-small nanoplastics. The vertical nanostructures, which allow particles to be trapped between the walls, therefore show great promise for identifying nanoplastics of 100 nm and below using SERS.

Correlative microscopy approaches enable direct correlation of morphology, composition, and nanoscale structure, which is essential for the reliable identification and interpretation of complex environmental particles. In biological matrices, such as tomato tissues exposed to europium-doped polystyrene nanoplastics, microscopy provides important information on particle morphology, aggregation and potential changes induced by sample preparation. The power of this approach is further demonstrated by environmental case studies, including the analysis of giant hailstones, where fibrous microplastics were first identified in their cores. A distinct spatial distribution of particles was observed, with fibrous materials concentrated in the inner regions and mineral particles dominating the outer layers, suggesting a potential role of lightweight fibers in ice nucleation and giant hail formation.

References:

1. SAHAI H., *et al.* Critical evaluation of enzymatic extraction for quantification of europium-doped polystyrene nanoplastics in tomato tissues by single particle ICP-MS, Ecotoxicology and environmental safety, 311, 119873, 2026, DOI: 10.1016/j.ecoenv.2026.119873
2. SHVALYA V., *et al.* Addressing SERS challenges of nanoplastics with vertical plasmonic substrates, Surfaces and interfaces, 69, 106780, 2025, DOI: 10.1016/j.surfin.2025.106780
3. SELEŠ P., *et al.* Altering defect population during the solvothermal growth of ZnO nanorods for photocatalytic applications, Ceramics international, 50, 2024, DOI: 10.1016/j.ceramint.2024.04.410
4. KOZJEK M., *et al.* Dissecting giant hailstones: a glimpse into the troposphere with its diverse bacterial communities and fibrous microplastics, Science of the total environment, 856, 2023, DOI: 10.1016/j.scitotenv.2022.158786

Zahvala

Organizacijski odbor 6. Slovenskega posvetovanja mikroskopistov, bi se rad zahvalil vsem sodelujočim za udeležbo, saj ste Vi in Vaši prispevki tisti, ki naredijo posvetovanje vredno obiska. Radi bi se zahvalili tudi vsem sponzorjem, ki ste finančno podprli posvetovanje ter s svojim obiskom ponudili obiskovalcem širok nabor mikroskopskih tehnik in naprav za mikroskopiranje.

Hvala za vaš prispevek.

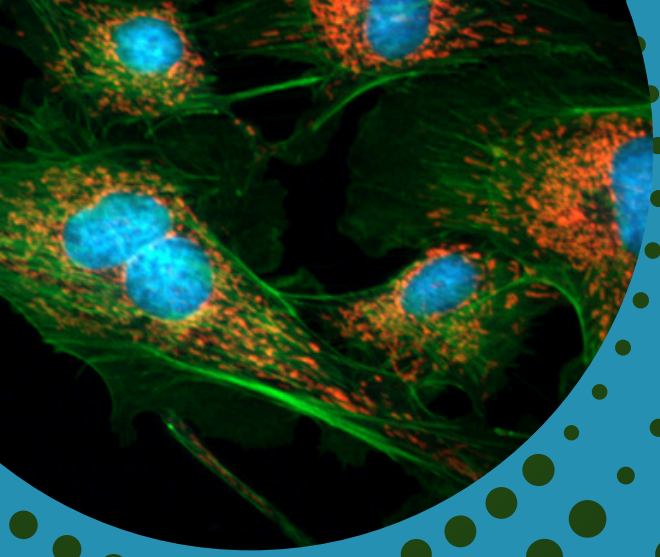

Slovensko
Društvo za
Mikroskopijo

SDM

Slovene
Society for
Microscopy